論文 / 著書情報
Article / Book Information

題目(和文)	
Title(English)	Methods for determination of nuclear fission probability and fission barrier heights
著者(和文)	KEANKUN RATHA
Author(English)	Kun Ratha Kean
出典(和文)	学位:博士(学術), 学位授与機関:東京工業大学, 報告番号:甲第11333号, 授与年月日:2019年9月20日, 学位の種別:課程博士, 審査員:千葉 敏,林崎 規託,片渕 竜也,相樂 洋,赤塚 洋
Citation(English)	Degree:Doctor (Academic), Conferring organization: Tokyo Institute of Technology, Report number:甲第11333号, Conferred date:2019/9/20, Degree Type:Course doctor, Examiner:,,,,
学位種別(和文)	博士論文
Type(English)	Doctoral Thesis

TOKYO INSTITUTE OF TECHNOLOGY

DOCTORAL THESIS

Methods for determination of nuclear fission probability and fission barrier heights

Author:
KEAN Kun Ratha
Student ID: 16D58362

Supervisor:
Prof. Satoshi CHIBA

A thesis submitted in fulfillment of the requirements for the degree of Doctor of Philosophy

in the

Graduate Major in Nuclear Engineering, Department of Trans-disciplinary Science and Engineering, School of Environment and Society

2019/8

TOKYO INSTITUTE OF TECHNOLOGY

Abstract

Graduate Major in Nuclear Engineering, Department of Trans-disciplinary Science and Engineering, School of Environment and Society

Doctor of Philosophy

Methods for determination of nuclear fission probability and fission barrier heights

by KEAN Kun Ratha
Student ID: 16D58362

Fission cross section is very important in many domains, such as nuclear physics, nuclear astrophysics and applications in nuclear technology. Fission probability (P_f) and barrier height (B_f) are the key input information to evaluate fission cross sections. These physical quantities can be determined by both experiment and theory. The objective of this work is thus to propose new method to experimentally and theoretically determine B_f. Experimental determination of fission cross sections or B_f for short-lived nuclei by neutron-induced fission approach is more often or even impossible due to the difficulties of target preparations, e.g., radioactive nature. Multi-nucleon transfer reactions (MNT) have been applied as an alternative approach to deduce B_f from the P_f distribution spectrum as a function of the excitation energy of the compound nucleus. Traditionally, light ion beams, e.g., $^{1-3}$H, ^{3,4}He and ^{7}Li etc., have been used. However, in the JAEA tandem accelerator facility, the use of heavier ions ^{18}O allow to study wider range of isotopes in a single experiment compared to the use of lighter ones. For this purpose, experiments employing ^{18}O beam on ^{237}Np was carried out. In the experiments, ^{18}O beam ($\sim$ 162.0 MeV, $\sim$ 0.5 pnA) was accelerated to bombar the ^{237}Np target (76.3 μg/cm^2 thick) on a natural nickel backing (300 μg/cm^2 in thickness). The detection system was composed of four multi-wire proportional counters (MWPCs) and of a segmented silicon ΔE-E telescope which serve for the detection of fission fragments and ejectiles, respectively. $P_f(max)$ and B_f were obtained by fitting the P_f spectra with the Hill-Wheeler's fission barrier penetration formula. Our B_fs agree well with the literature data, thus demonstrating the potential of the MNT reactions to obtain fission-barrier data which is not accessible for fission studies via neutron- or light charged-particle induced reactions. However, the magnitude of P_fs disagree with the literature data, probably due to the different transferred angular momentum during the collisions. We also performed theoretical analysis of the B_f. The B_fs, estimated by the quadrupole-deformation constrained Hartree-Fock + BCS theory using the Skyrme forces, namely SkM* and SLy4, are too large with respect to our data and the literature data. Although, it was well known from Strutinsky calculations that the restriction of the nuclear shapes to axial symmetry assumed in our calculations leads to too high barriers, we studied the nuclear medium effect represented by the density dependent force term of the energy density functional including three- and more-body forces. As a result, we found that the many-body force is shown to have a significantly large impact on the barrier height magnitude of heavy nuclei. Newly modified Skyrme parameter sets for SkM* and SLy4 are proposed. As a grand summary, we studied on B_f by both a novel experimental technique and theory.

Acknowledgements

I am sincerely and heartily grateful to my academic supervisor, Prof. Satoshi CHIBA, for accepting me as his doctoral student, for the support and guidance for both my researches and daily life. He showed me throughout my dissertation writing. I am sure it would have not been possible without his help. Besides I am truly indebted and thankful Dr. Katsuhisa NISHIO who is a manager of research group for heavy-element nuclear science (HENS) at Japan Atomic Energy Agency (JAEA) and allowed me to perform my research activities with his group. He did not only supervise my research activities but also help about my life issues. Moreover, I owe sincere and earnest thankfulness to Prof. Igor TSEKHANOVICH at Bordeaux University, France and Prof. Andrei ANDREYEV at York University, UK and also a leader of HENS for giving good advice for writing my dissertation and my accepted manuscript which is part of my dissertation. Furthermore, I would like to show my gratitude to Dr. Hirose KENTARO at JAEA and Dr. Mark VERMEULEN, a former postdoctoral student from UK at JAEA, who guided me for data analysis. Thanks are also given to Dr. Yoritaka Iwata, a former researcher at prof. Chiba's laboratory and now associate professor at Kansai University, who locally supervises my theoretical work in chapter 6. I thank my family, in particular, my wife who always motivates and strongly supports my study. This dissertation would not have been possible unless all kind of supports from everyone in Prof. Chiba's lab and HENS at the JAEA. The work is partially supported by the "Comprehensive study of delayed-neutron yields for accurate evaluation of kinetics of high burn-up reactors", by the Ministry of Education, Culture, Sports, Science and Technology of Japan (MEXT), and K.R. Kean is supported by the MEXT scholarship program for Cambodian citizens. We thank the tandem accelerator operators who provided the beam with very good conditions. This work was supported by JSPS KAKENHI Grant No. 17K05440. Calculations were carried out at the work station in LANE, Tokyo Institute of Technology.

Contents

List of Figures

List of Tables

List of Abbreviations

MNT	**Multi-Nucleon Transfer**
HF	**Hartree-Fock**
BCS	**Bardeen–Cooper–Schrieffer**
FFMDs	**Fission Fragment Mass Distributions**
LDM	**Liquid Drop Model**
SCM	**Shell-Correction Method**
CENBG	**Centre Etudes Nucléaires de Bordeaux Gradignan**
WE	**Weisskopf-Ewing**
CN	**Compound Nucleus**
exp	**experiment**
JAEA	**Japan Atomic Energy Agency**
PID	**Particle Identification Plot**
MWPC	**Multi-Wire Proportional Counter**
R.C.E	**Random Coincidence Events**
FWHM	**full width at half maximum**
mSLy4	**modified SLy4**
mSkM*	**modified SkM***
BE ratio	**Binding Energy ratio**
FB ratio	**Fissin Barrier ratio**

Physical Constants

Speed of Light	$c = 2.997\,924\,58 \times 10^{8}\,\mathrm{m\,s^{-1}}$ (exact)
Planck's constant	$\hbar = 6.626\,070\,150(81) \times 10^{-34}\,\mathrm{J\,s}$

List of Symbols

B_f	fission barrier height	(MeV)
P_f	fission probability	
ω	angular frequency	$\mathrm{rad\,s^{-1}}$

Chapter 1

Introduction

Since its discovery by Hahn and Strassmann in 1939, the fission characteristics have been extensively studied by both experiment- [4] and theory-wise [62, 61]. For both fundamental and applied aspects, the interpretation of how nuclei undergo fission and fission cross section are of special interest. Fission cross section is a challenging research topic not only in the physics phenomena, but also in the applications, such as nuclear-astrophysics and nuclear technology.

In astrophysics, to answer the most common questions about the nature, such as the origin of the elements necessary for life, the age of the universe and the formation and evolution of the Suns, the stars and the Galaxies, the detailed stellar model with high precision must be developed [59]. The compound nuclear cross sections play a crucial role in the understanding of the nucleosynthesis of the heavy elements beyond ^{56}Fe, which takes place by the neutron capture on the lighter seed of nuclei, so-called "s" (slow neutron capture) and "r" (rapid neutron capture) processes.

The present electric powers generated by nuclear reactors represents around 11% of the total production worldwide. Management of nuclear waste, and in particular, of long-lived minor actinides produced in these reactors, is one of the most important issues in the use of nuclear power. Among the radioactive species in nuclear wastes, minor actinide nuclei (neptunium, americium and curium isotopes) are the most hazardous as they concentrate $\approx$ 95% of the radioactivity, even though they are observed only $\approx$ 0.2 % of the total volume of the generated waste [38]. In order to deal with nuclear waste management problems, it thus requires very accurate measurements of the fission cross section to transmute them into short-lived fission products in such a system as accelerator-driven systems (ADS) or by fast reactors.

The fission barrier height introduced by Bohr and Wheeler [13] is one of the most fundamental quantities to describe fission. The fission barrier height and its curvature are one of the essential parameters to estimate the fission cross section. The partial half-life for spontaneous fission of heavy nuclei is closely connected with the hight of the barrier. In the classical liquid-drop picture, the fission barrier is created by a balance between the attractive surface energy and the repulsive Coulomb force which shows an inverted parabolic shape as a function of deformation in a rather simple (parabolic) way. The single-humped fission barrier, see, e.g., Fig. 2.1, which arises in the macroscopic liquid drop approach, is dramatically modified by introducing shell correction energies [66]. These microscopic corrections modify the smooth parabolic barrier, producing a double- or triple-humped fission-barrier shape, see, e.g., Fig. 2.3 or Fig.2 of [39]. The double-humped fission barrier can be also reproduced by the Hartree-Fock (HF) theory. The pure microscopic HF approach (+ Skyrme force [72]) allows to calculate fission barrier heights for the first time in 1973 [26], despite the fact that the results do not agree with experimental ones and with those calculated with the shell-correction method. However, it was a first step to confirm that the two-humped barrier is able to be reproduced in this model. Although the reason has been

well understood from Strutinsky calculations that the restriction of the nuclear shapes to axial symmetry in calculations leads to too high barriers by about 0.5–2 MeV, we cast out on another factor "the nuclear medium effect".

Up to now, information on the fission barrier profile in actinide nuclei has been derived using neutron-induced fission and nucleon-transfer reactions with light projectiles, such as (d,p) [23, 28, 21], (t,p) [6, 21] and (^{3}He,d) [7] reactions. In these methods, the fission probability is usually measured as a function of excitation energy of the fissioning nucleus. The height of the fission barrier is then equal to the excitation energy of the nucleus, corresponding to the half-maximum of the fission probability curve for the first chance fission [70]. However, such methods require the use of stable or long-lived target nuclei, which limits the range of accessible nuclei along the beta-stability line, and thus the number of the isotopes which can serve as targets for such kind of studies. This explains the relative scarcity of the available experimental data on the fission barrier profile: to our knowledge, there are fission barrier data available on just 33 nuclei in the best-studied actinide region [18, 12], out of a few hundred known between uranium and californium.

Recently, it is demonstrated that reliable fission data, e.g., fission fragment mass and kinetic-energy distributions, can be assessed via multi-nucleon transfer (MNT) reactions of ^{18}O beam interacting with actinide targets, such as ^{232}Th, ^{238}U, etc. [44, 34]. Due to a large number of MNT channels accessible in reactions with ^{18}O beam, low-energy fission data for about twelve nuclides can be simultaneously taken in a single experiment. For instance, the study [34] reports on the fission fragment mass distributions (FFMDs) for twelve isotopes of uranium, neptunium and plutonium measured in the ^{18}O + ^{238}U reaction.

The aims of this work is to determine the fission barrier heights experimentally and theoretically. In experiment, the present work deals with the extension of the MNT method for determining the fission-barrier height. For a given excitation energy, due to the use of a relatively heavy projectile (^{18}O), the excited states populated in the fissioning nucleus can be different in terms of spin and parity compared to those created in traditional neutron-induced or one- or two-nucleon transfer reactions with light projectiles, such as ^{3}He. This may result in a different fission probability, and thus may affect the fission-barrier height. Therefore, it becomes important to benchmark the MNT technique by comparing the data on fission probabilities and barriers with available literature data. We also performed a theoretical analysis of the fission barrier in order to find out new Skyrme parameter sets. In the calculation, we employed the quadrupole-deformation constrained Hartree-Fock + BCS theory with the Skyrme forces, namely SkM* and SLy4.

Chapter 2

Theoretical and methodological background

In this chapter, the essential backgrounds for both theory and experimental approach have been provided which are useful to understand the experiments. For theoretical backgrounds, we mention the concepts of fission barrier height and fission processes by starting from the classical liquid-picture to the shell-correction model (the Strutinsky approach). In methodological background, we introduce the principle of nuclear reactions by using the classical picture of heavy ion collisions, in particular the multi-nucleon transfer technique.

2.1 Nuclear fission

2.1.1 Discovery of fission

In an attempt to explain the resulting radioactivity as coming from a new element (Z = 93) or even several "transuranium elements", the experiment was performed by Enrico Fermi and his collaborators in Rome in May 1934. In the experiment, the neutrons moderated by paraffin were used to bombar the uranium (Z = 92). However, a wide variety of radioactivities were observed, and radiochemical properties were too unexpected to explain in this way. The phenomenon could not be understood until 1938, Hahn-Strassman and Maitner-Frisch identified the new process (called fission) in which a nucleus is split into fragments (normally two, but three in few cases). Soon after revealing the existence of fission, Maitner and Frisch also proposed a qualitative explanation of the process based on the analogy of a charged liquid drop.

2.1.2 The liquid drop model (LDM)

This model relies on the basic idea of considering a nucleus as a uniformly charged liquid drop. The stability or disintegration (fissioning) of a nucleus is controlled by balance between the attractive nuclear force described by a (classical) surface tension and the repulsive Coulomb force.

This same model is the basis of the semi-empirical formula extended by Weizsäker [74] and Bethe [11, 10], in which the total mass (binding energy) of a nucleus is expressed as:

$$\begin{aligned} E(N,Z) = \; & a_V(1+k_V I^2)A + a_S(1+k_S I^2)A^{2/3} + \\ & c_d Z(Z-1)A^{-1/3} + c_{exc} Z^{4/3} A^{-1} + \\ & P(N,Z) + \delta E(N,Z) \end{aligned} \tag{2.1}$$

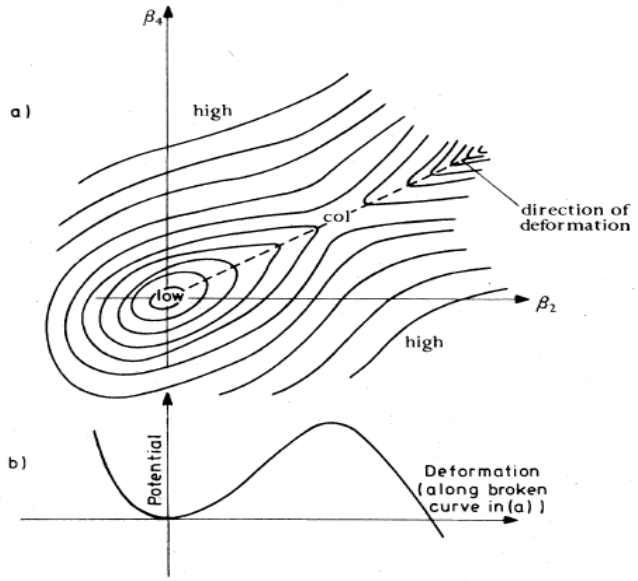

FIGURE 2.1: (a) Schematic representation of the potential energy contours of a fissionable nucleus is plotted as a function of the quadrupole β_2 and hexadecapole β_4 deformation parameters. (b) The variation of potential energy along with the increasing the deformation β_2, and the minimum potential corresponds to $\beta_2 = 0$ (spherical shape). [This figure taken from [12]]

with the mass number A is the sum of the number of proton Z and the number of neutrons N, $A = N + Z$, and $I = \dfrac{N - Z}{A}$.

Here a_V and a_S represent so-called volume and surface energies, k_V and k_S the asymmetry coefficients, the terms with c_d and c_{exc} indicate the direct and exchange Coulomb energies, $P(N, Z)$ is the paring energy ($\sim\pm$ 2 MeV) and $\delta E(N, Z)$ is the shell correction energy term originated from the quantum mechanical effect. All other terms, except δE and $P(N, Z)$, are the smooth function of N and Z and mainly contribute to the binding energy ($\gtrsim$ 99% in a heavy nucleus). Equation (2.1) can be summarized as

$$E(N, Z) = E_{LDM}(N, Z) + P(N, Z) + \delta E(N, Z), \tag{2.2}$$

where $E_{LDM}(N, Z)$ illustrates the liquid drop energy, which accounts for all terms.

We note that in most early LDM calculations, the deformed nuclear surface can be determined by the multipole expansion in a spherical harmonic $Y_{\lambda,\mu}(\theta, \phi)$:

$$R(\theta, \phi) = R_0[1 + \sum_{\lambda,\mu} \beta_{\lambda,\mu} Y_{\lambda,\mu}(\theta, \phi)]. \tag{2.3}$$

Here R_0 is the nuclear radius at the spherical shape, $\beta_{\lambda,\mu}$ is the deformed shape parameter. Figure 2.2 shows examples of nuclear shape due to the different deformation types associated with λ, μ. From left to right, first row, $\beta_{\lambda,\mu} = 0$, $\beta_{20} > 0$, $\beta_{20} < 0$ and $\beta_{40} > 0$ indicate sphere, prolate spheroid, oblate spheroid and hexadecapole shape, while the second row illustrates triaxial ellipsoid ($\beta_{22} \neq 0$), reflection asymmetric octupole ($\beta_{30} \neq 0$), tetrahedron ($\beta_{32} \neq 0$), reflection asymmetric octupole with very large quadrupole and hexadecapole deformation ($\beta_{20} \gg 0$). If one assumes that a nucleus undergoing fission remains symmetric with respect to its rotation around its

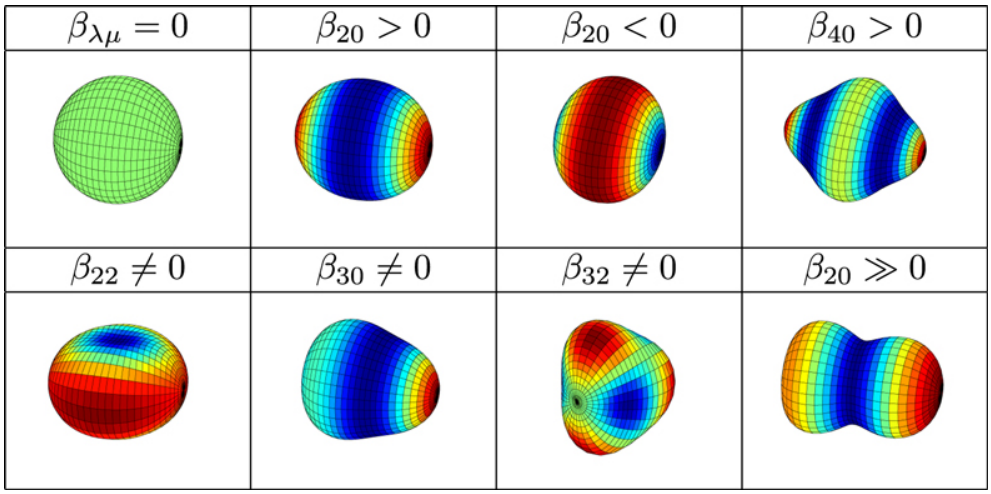

FIGURE 2.2: The representation of nuclear shapes with respect to the typical values of the deformation parameters β_λ are shown. First row, $\beta_{\lambda,\mu} = 0$, $\beta_{20} > 0$, $\beta_{20} < 0$ and $\beta_{40} > 0$ indicate sphere, prolate spheroid, oblate spheroid and hexadecapole shape, while the second row, triaxial ellipsoid $\beta_{22} \neq 0$, reflection asymmetric octupole $\beta_{30} \neq 0$, tetrahedron $\beta_{32} \neq 0$, reflection asymmetric octupole with very large quadrupole and hexadecapole deformation $\beta_{20} \gg 0$. It was taken from [47].

deformation axis ($\mu = 0$), $\beta_2 = \beta_{20}$ and $\beta_4 = \beta_{40}$ are called quadrupole and hexadecapole deformation parameters, respectively.

To explain the fission process, according to the deformed shape of the nucleus, the deformation energy represented by the parameter β, has been introduced into the model . The deformed energy $E^{def}_{LDM}(\beta)$ is defined as the difference between the energy at a given deformation β and at a spherical shape ($\beta = 0$). To this difference, only surface and Coulomb terms take part. Due to the conservation of nuclear volume (incompressible nuclear matter), the volumic term falls out. The deformed energy can be therefore expressed as the sum of the surface and the Coulomb energy:

$$E^{def}_{LDM}(\beta) = E_{Surf}(\beta) + E_{Coul}(\beta). \tag{2.4}$$

Note that both terms are normalized to zero at a spherical shape ($\beta = 0$).

In the LDM, the critical parameter known as the "fissionability" or (fissility) parameter χ is defined as the ratio of the Coulomb energy to the twice of the surface energy for a charged sphere of radius R_0:

$$\chi = \frac{E_{Coul}(0)}{2E_{Surf}(0)} \tag{2.5}$$

with

$$E_{Coul}(0) = \frac{3}{5}\frac{Z^2e^2}{R_0}; E_{Surf}(0) = 4\pi R_0\tau. \tag{2.6}$$

Here τ represents the surface tension, which can be related to the surface term in Eq. (2.1) as

$$\tau = a_S(1 + k_S I^2)/4\pi r_0^2 \tag{2.7}$$

with the empirical relation

$$R_0 = r_0 A^{1/3}; r_0 \simeq 1.2 fm. \tag{2.8}$$

Combining Eqs. (2.5 – 2.8), besides the relatively weak I^2–dependence of τ, the fissility parameter *chi* is observed to go like Z^2/A. We frequently write

$$\chi = \frac{\left(\frac{Z^2}{A}\right)}{\left(\frac{Z^2}{A}\right)_{crit}}. \tag{2.9}$$

With the above constants and given empirical values $a_S \simeq 18 MeV$; $k_S \simeq -2.5$, we obtain

$$\left(\frac{Z^2}{A}\right)_{crit} \approx 45 - 50 \tag{2.10}$$

In the LDM (Bohr-Wheeler), this barrier maximum is written as

$$\frac{B_f}{E_{Surf}(0)} = \frac{98}{15}\left(1 - \chi^3 - \frac{11368}{34425(1-\chi)^4}\right). \tag{2.11}$$

The main results of the LDM can be summarized as following:

1. For $\chi < 1$, all nuclei with the spherical configuration (all $\beta_\lambda = 0$) have minimum potential energies, see Fig. 2.1. Thus, the LDM estimates that these nuclei are stable in their spherical ground states. For $\chi > 1$, the negative $E^{def}_{LDM}(\beta)$ and there is no barrier toward fission. The unstability against quadrupole deformation ($\beta_2 = 0$) of a nucleus with a spherical shape occurs, then the nucleus undergoes self-deforming until fission (known as spontaneous fission). Therefore, all nuclei with $\chi > 1$ have been predicted by the LDM to go into spontaneous fission. Note that a heavy actinide nucleus has $\chi \simeq 0.8$ for $(Z^2/A) = 40$.

2. For $0.7 \lesssim \chi < 1$, the deformation energy has a maximum so-called saddle point with the positive energy B_f positive with respect to the ground state (fission barrier height). This result is obtained only if β_2 and β_4 are used, see Fig. 2.1. The LDM overestimates the fission barrier height compared to the measured data, as shown in Tab. 2.1. The LDM barrier heights vary in the range 15–9 MeV, whereas the measured data give around between 5.5 and 6.5 MeV. Consequently, the LDM provides the wrong quantitative behavior of fission barrier heights.

3. For $\chi > 0.39$, the nucleus is always stable against rotationally asymmetric (represented by $\mu \neq 0$) and reflection (left/right) asymmetry (also called mass asymmetry) for λ odd deformation. In fact, only parameter β_λ with λ even doesn't vanish. As a result, the LDM is not able to interpret the mass asymmetry in fission.

   In short, main failures of the LDM, such as no static deformations of nuclear shape (or potential energy), wrong estimations of fission barrier heights and no asymmetric fission, come from the missing of the quantum mechanical (shell) effects. Remember that the order of magnitude of the empirical shell-corrections compared to the ground masses [52] is:

TABLE 2.1: Comparing the calculated LDM fission barrier height (B_f^{the}) with the experimental barrier data (B_f^{exp}), both in MeV. The value of fissility parameter χ has been calculated using $(Z^2/A)_{crit}$ = 50. [the data from Wilets, 1964 [46]].

Isotope	χ	B_f^{the}	B_f^{exp}
^{233}Th	0.694	15.58	6.44
^{232}Th	0.697	15.08	5.95
^{239}U	0.707	13.51	6.15
^{238}U	0.710	13.06	5.80
^{232}Ra	0.713	12.68	6.18
^{237}U	0.713	12.63	6.40
^{235}U	0.719	11.79	5.75
^{233}U	0.725	10.96	5.49
^{238}Np	0.725	10.92	6.04
^{237}Np	0.729	10.53	5.49
^{239}Pu	0.739	9.39	5.48

$$|\delta E| = |\delta M| \simeq 5 - 15 MeV. \tag{2.12}$$

Even though this value is too small with respect to the total binding energies of heavy nuclei ($\sim$ 1000 - 2000 MeV), it turns out to be absolutely significant when compared to the fission barrier heights.

Therefore, the LDM can qualitatively describe the fission process, but the shell effects need to be take into account in order to be a quantitative theory.

2.1.3 The (deformed) shell model

In the shell model [31, 50], the quantum mechanical structure of a nucleus can be described as a system of Z protons and N neutrons. Nucleons (proton or neutron) are assumed to move independently inside the mean potential created by the mutual interaction between them. For each kind of this nucleon with mass "m" and a wave function "$\psi_i(r)$", the Schrödinger equation can be written as

$$H\psi_i(r) = \left[-\frac{\hbar^2 \Delta}{2m} + V(r) \right] \psi_i(r) = \varepsilon_i \psi_i(r), \tag{2.13}$$

where the Hamiltonian H is the sum of the kinetic energy of a nucleon (-$\frac{\hbar^2 \Delta}{2m}$) and the mean potential $V(r)$. Potentials $V_n(r)$ and $V_p(r)$ constitute a local (central) and a spin-orbit part. $V_p(r)$ additionally includes the Coulomb interaction among the protons. The eigenvalue ε_i of H, representing a single particle energy of each particle, is obtained by solving this equation.

In order to connect with the fission, we most prefer the Nilsson model (deformed shell model) [53] which extends the shell model to deformed nuclei. In the Nilsson model, the deformed nuclear shape leads to the deformation of potentials $V_n(r)$ and

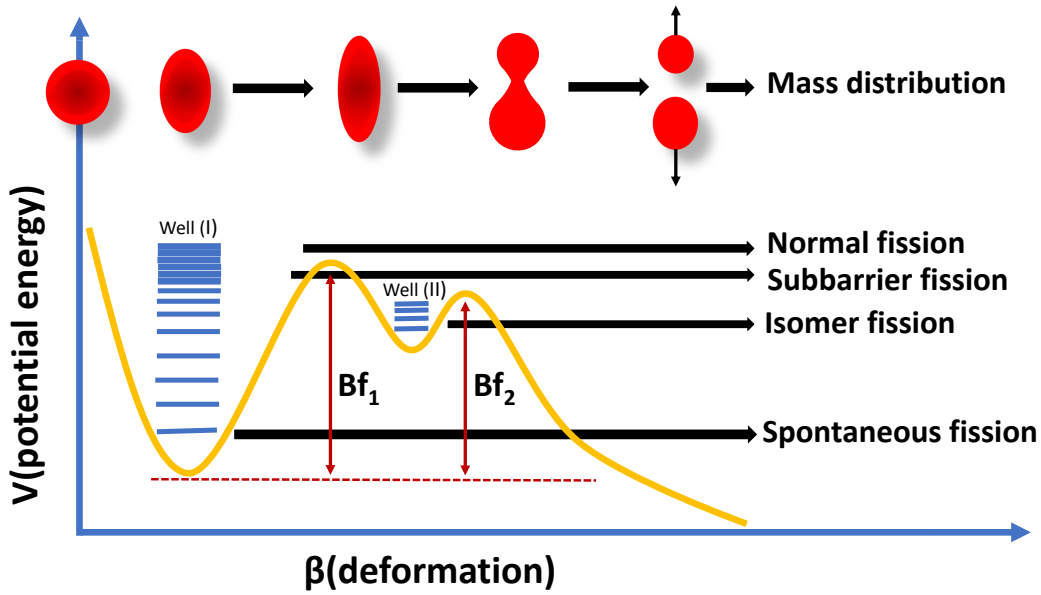

FIGURE 2.3: Schematic representation of the deformed nuclear potential (well (I) and well (II)) as well as corresponding nuclear shapes (asymmetric deformation in the second barrier region) along with the deformation β in the A $\approx$ 240 region is illustrated. It includes deferent fission types, namely spontaneous, isomer, subbarrier and normal fission. $B_f(1)$ and $B_f(2)$ stands for the inner and outer barrier, respectively.

$V_p(r)$ as well. As a consequence, the solution of the Schrödinger equation is also as a function of the deformation parameter β. In the independent particle model, the total energy of a nucleon system in a nucleus can be expressed as

$$E(\beta) = \sum_{i=1}^{N} \epsilon_i^n(\beta) + \sum_{i=1}^{Z} \epsilon_i^p(\beta). \tag{2.14}$$

Strictly speaking, the justification of the shell model is provided by the Hartree-Fock theory (which will be discussed exclusively in Chapter 6), where Eq. (2.14) does not illustrate the total binding energy.

Minimizing the energy $E(\beta)$ with respect to β results in the deformation of the ground state at β_0. From the Nilsson spectra ($\epsilon_i(\beta_0)$) at the ground state, it is possible to deduce other properties of the nuclei, such as spin, magnetic moment and single particle spectra of odd-A nuclei.

The model meets its failure when extended to large deformations. The deformation energy in Eq. (2.14) was observed to increase very sharply and not to produce any reasonable fission barrier height [54]. Similar results were also seen in the two-center shell model (e.g. [60]).

The reason for this breakdown is due to the exclusion of self-consistency of employed mean deformed potentials and of the formula (2.14) for the total energy. At small (ground state) deformations, experimental data from spectroscopy enables to parametrize the shell model with satisfaction. However, when extended to the large deformations, it turns out that results depend strongly on parameters and how potentials deformed.

This brings Myers and Swiatecki [52] to discuss the relation between the non-uniformities of the shell model spectra ϵ_i and the magnitude of empirical values in

shell corrections δE in Eq. 2.1. For the magic nucleon numbers, it is observed large gaps, which cause the increase of binding energy (negative δE).

It was Strutinsky [65, 66], who introduced the quantitative method for the calculating δE well known as the shell correction method (or Strutinsky method).

2.1.4 The shell-correction method (SCM) ("Strutinsky method")

Strutinsky used his own strategy to formulate the shell correction δE for each type of nucleon as

$$\delta E_{p(n)} = \sum_{i=1}^{Z(N)} \epsilon_i^{p(n)} - \tilde{E}_{p(n)}. \tag{2.15}$$

Here for each kind of particle, the first term is the sum of the ocupied level energies while the second term represents its mean energy.

$$\tilde{E}_{p(n)} = \left\langle \sum_{i=1}^{Z(N)} \epsilon_i^{p(n)} \right\rangle. \tag{2.16}$$

The total energy of the nucleus can thus be written as:

$$E(N, Z, \beta) = E_{LDM}(N, Z, \beta) + P(N, Z) + \delta E_p(Z, \beta) + \delta E_n(N, \beta), \tag{2.17}$$

This demonstrates that the average parts of the single-particle energies is renormalized by the LDM energy. Therefore, one did obtain the modified total energy by combining the correct mean energy of the LDM with the correct fluctuating part δE of the shell model energy of Eq. 2.14.

The essential results of the SCM can be summarized as:

1. The produced double-humped fission barrier behavior (B_{f1} inner and B_{f2} outer barrier), see Fig. (2.3), allows to interpret the fission isomers, although it had been discovered long time ago [57]. At present, most actinide nuclei are well recognized to have two barriers.

2. Calculated and experimental fission barrier heights quantitatively agree each other, normally within roughly 1-2 MeV, except for neutron-poor lighter actinides (Th-anomaly).

3. There are excellent agreement between the ground-state deformation and the experimental ones. For example, discrepancies between calculated and experimental ground-state masses δE (δM) are within around 1-2 MeV, but very large for ^{208}Pb region (Pb-anomaly).

4. It explains qualitatively the mass asymmetry of the fission products, see Fig. (2.3), governed by the shell effects for both at the outer saddle point and at the scission point.

5. It predicts a possible island (or several) of stable nuclei with Z $\approx$ 114–126 or larger. In brief, the existence of "the superheavy nuclei".

   To summarize, the Srutinsky technique provided a breakthrough in the theory of fission barrier height, enabling for the first time to calculate the fission barrier heights with satisfaction and also to explain the fission isomers as shape isomers. It plays a balance role between the LDM and the shell model.

2.1.5 Fission process and barrier penetration

For heavy nuclei in the A $\approx$ 240 region, a nucleus can undergo fission in different ways, namely, spontaneous, isomer, subbarrier and normal fission, see Fig. 2.3. To make nuclear fission happening, it requires the necessary minimum energy to distort a nucleus to the point (saddle point), see Fig.2.1, where this nucleus is split into two (or three parts) which is well recognized as fission process. This energy can either come from external agent, e.g., neutron bombardment or self deformation in theirs ground states (spontaneous fission via quantum tunneling effect). If a nucleus undergo fission spontaneously from its ground state, and then it might be trapped in the second well before continuing to fission. This phenomenon is called isomer fission. If one imping a nucleus with a particle, e.g., a neutron, the nucleus might get excited with the excitation energy higher than the highest fission barrier or in between the two barrier tops. The former is called normal fission and the later is subbarrier fission. Remind that most actinide nuclei are known to have double barriers (inner and outer barrier), see Fig. 2.3, or third barriers are suggested for some other actinide nuclei, e.g., thorium isotopes.

The magnitude of fission barrier heights contribute to the various observations of the fission phenomena. For instance, if one is much higher than other, then only the information on the height and curvature of the highest peak can be observed experimentally. In this case, no sub-barrier resonance will occur. In contrast, if two peaks have comparable heights, in some cases there are observations of sub-barrier resonances in the fission probability spectra near the top of the lowest peak. For many doubly-even-isotopes of uranium and plutonium, the existence of resonance structures have been previously provided in the fission probability spectra [6].

Fission barrier, in particular its height, is a basis to interpret the fission in nuclear reaction studies. Such data are experimentally derived from the fission rate (or fission probability) distributions which will be discuss in details in Chapters 4 and 5. In the Hill-Wheeler's barrier penetration calculation based on the assumption of the inverted parabola barrier (harmonic oscillator form) gives the barrier penetration (or barrier transmission coefficient) [33] as

$$P_{\mathrm{f}}(E^*) = \frac{P_{max}}{1 + \exp\left(\dfrac{2\pi(B_f - E^*)}{\hbar\omega}\right)}, \tag{2.18}$$

where E^* is excitation energy, and three fitting parameters P_{max}, B_f and $\hbar\omega$ represent maximum fission probability reached by the 1^{st} chance fission, fission barrier height and its curvature, respectively.

The term $\hbar\omega$ represents the barrier thickness. The larger value of $\hbar\omega$, the thinner barrier. The slope of the measured P_{f} distribution is strongly related to $\hbar\omega$ values. If the barrier is thick, there is a small probability to have the tunneling effect below the barrier peak resulting in the sharp rising of the probability spectrum. The opposite is true in the case of the large value of $\hbar\omega$. The half-lives of the spontaneous fission are highly connected with not only the effective height of the barrier but also to the width and the inertial parameter related with the nuclear collective motion along the fission path. Usually, $\hbar\omega$ deduced by Hill-Wheeler's expression is very large with respect to that obtained by the statistical model which is based on the double humped-assumption [22]. However, B_{f} of the Hill-Wheeler is also applied in the statistical model.

2.2 Heavy ion collisions

When two nuclei collide each other, different types of reactions may occur. Three qualitatively distinct reactions, such as distant, grazing and close collisions, are shown in Fig. 2.4. The reaction type is strongly associated with interplay between the Coulomb and nuclear interactions. As the nuclear interation is a short range type, this kind of the interaction is involved only in a quite limited range of the impact parameter b and with the bombarding energy E_{cm} to overcome the Coulomb barrier $V(R)$ associated with the reduced-wavelength, the wavelength of the relative motion of the colliding nuclei, which can be determined as

$$\lambda\!\!\!^{-} = k^{-1}(R) \approx \left(\frac{A_1 + A_2}{A_1 A_2} \times \frac{20MeV}{E_{cm} - V(R)} \right)^{1/2} \text{ fm}, \tag{2.19}$$

where A_1 and A_2 denote mass numbers of colliding nuclei. If the nuclear interaction of the colliding system is ignored, the potential energy barrier is only the Coulomb interaction $V(R)$ given as

$$V(R) = \frac{Z_1 Z_2 e^2}{R}. \tag{2.20}$$

If colliding system are lighter nuclei, the interaction radius R can be determined by

$$R = [1.36(A_1^{1/3} + A_2^{1/3}) + 0.5] \text{ fm}, \tag{2.21}$$

and if colliding system are heavier nuclei, the interaction radius can be determined by

$$R = [1.16(A_1^{1/3} + A_2^{1/3}) + 2.4] \text{ fm}. \tag{2.22}$$

The distinction is again based on the impact parameter b or the corresponding angular momentum $l = bp_\infty/\hbar$, where p_∞ represents the asymptotic initial relative momentum. Here, b_{gr} is defined as the *grazing impact parameter* which is the impact parameter of the grazing trajectory (the nuclear interaction threshold) at which the nuclear interaction just begins. At b_{gr}, the nuclear interactions are very weak by definition. We also define an *interaction radius* R as the closest distance of approach between the centers of the nuclei on the grazing trajectory. The ejectile scattered in a particular angle due to the grazing collision is called grazing angle which is determined in the center-of-mass system (CM) as

$$\theta_{gr(CM)} = 2arcsin \left[2 \left(\frac{E_{CM}}{V(R)} - 1 \right) \right]^{-1} \tag{2.23}$$

This angle can also be calculated by using LYSE++ software [45]. The results are almost the same. If b is lager than b_{gr}, only Coulomb interaction is involved. It is called a distant collision or elastic (Rutherford) scattering. This is the most dominant part of nuclear collision which will be observed in the particle identification plot (Fig. 4.5) in chapter 4. It is indicated as "Elastic Scattering". There are two kinds of close collision when b is smaller than b_{gr}. If a projectile fuses with a target nucleus in a intermediate stage, it is known as a compound-nucleus formation collision. If only some nucleons are exchanged between them, it is a dissipative collision or direct reaction. Sine the nucleus is not transparent enough, the dissipative collision mainly occurs around the nuclear surface. It takes longer time for projectile to interact with the nucleons of the target nucleus in the compound-nucleus formation collision (10^{-18}s - 10^{-16}s) than in the dissipative collision (10^{-22}s). In our study, we concentrate on the multi-nucleon

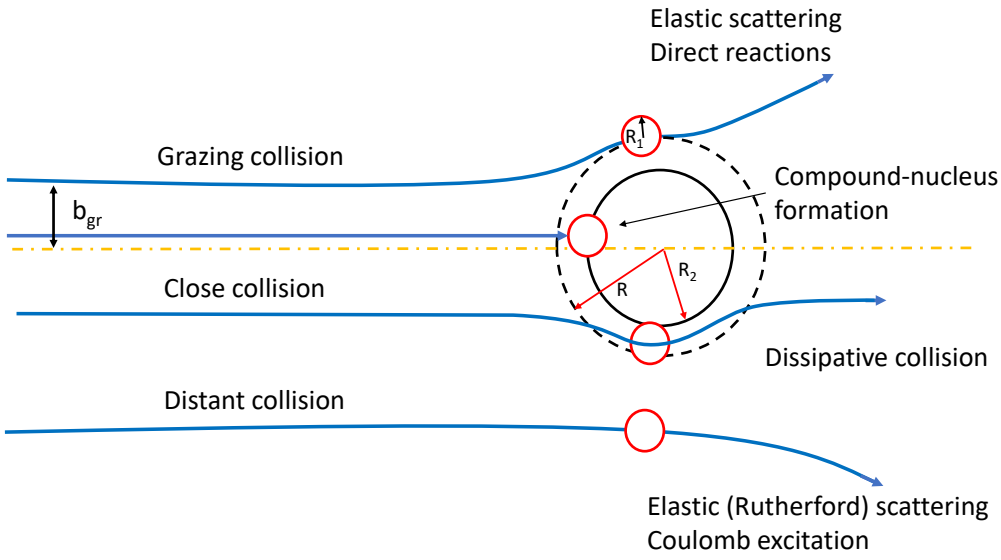

FIGURE 2.4: Distant, grazing and close collisions are shown in the classical picture of heavy ion collisions.

transfer reaction which is a type of the dissipative collision. Taken our measurement as a compelling example, the ^{18}O was bombarded on ^{237}Np target at E_{cm} = 150.48 MeV (E_{lab} = 162 MeV) above the interaction barrier V(R) calculated to be $\approx$ 85 MeV at R $\approx$ 12.62 fm, we obtain $\lambda \approx 0.12$ fm, which is small with respect to characteristic lengths (e.g. surface thickness $\approx$ 2 fm) of the colliding system. The grazing angle in the center of mass frame ($\theta_{gr(CM)}$) is 45.91^0 for this colliding system. For ^{18}O + ^{nat}Ni reaction with same beam energy as the above reaction, the grazing angle ($\theta_{gr(CM)}$) is 16.95^0. These grazing angle are very useful information for placing the telescope detector in the forward direction (Chapter 3, Sec. 3.3.1) which is very sensitive to the high intensity of elastic scattering particles. In our case, we placed our telescope detector between these two angles.

2.3 Multi-Nucleon Transfer Reaction

The multi-nucleon transfer (MNT) approach (also called surrogate method) is an alternative technique to the neutron-induced fission allowing for the fission cross-section studies on a much wider range of nuclei. It is noted that "surrogate method" is mentioned in the sens that when it is employed to derived the neutron-induced cross section of the desired nucleus. In 1970s, the surrogate approach was introduced by [21, 14] at the Los Alamos National Laboratory. This technique regained its popularity, when two groups at the Centre Etudes Nucléaires de Bordeaux Gradignan (CENBG) and the Lawrence Livermore National Laboratory used it to extract cross section of interest for reactor physics [75, 76, 56, 16, 25, 24, 37, 41]. The recent studies have been also attempted to derive the (n,γ) cross section with this technique [23]. Usually, the information on a fission barrier profile has been derived for actinide nuclei stemming from nucleon-transfer reactions with light projectiles, such as (d,p) [23, 28, 21], (t,p) [6, 21] and (^{3}He,d) [7] reactions up to now. In the MNT, see Fig. 2.5, the nucleus of interest is created in collisions of a beam with target nuclei, via the

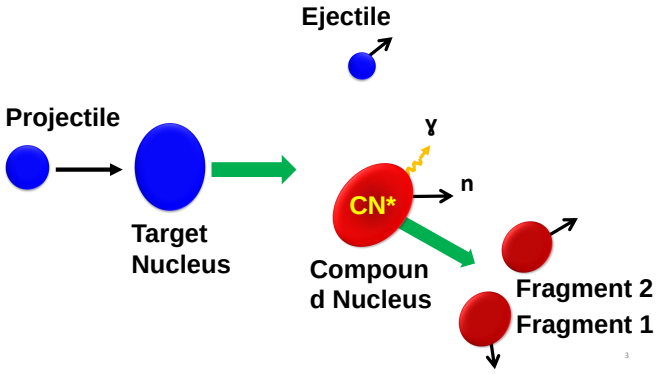

FIGURE 2.5: Schematic representation of multi-nucleon-transferred method. Three possible decay modes (fission, gamma and neutron emission) are indicated.

exchange of nucleons between them. As a result of the reaction, an ejectile and a corresponding compound nucleus are obtained. Since the formed compound nucleus is excited, it may therefore de-excite via different modes (or exit channels): either fission, or emission of gamma-rays or neutrons, etc. Actual beam-target combination used in the MNT determines the number of created compound nuclei, thus allowing a simultaneous study of their decay channels.

In the MNT, compound-nuclear cross sections can be appropriately described by the statistical Hausser-Feshbach theory (H-F) [30]. For the reactions leading to an energy region in the final nucleus, the average cross section per unit energy in the outgoing channel can be described by a level density given as:

$$\frac{d\sigma_{\alpha\chi}^{H-F}(E_{pro})}{dE\chi} = \pi\lambda\!\!\!^{-2}\sum_{J\pi}\omega_{\alpha}^{J}\sum_{lsl's'I'}\frac{T_{\alpha ls}^{J}T_{\chi l's'}^{J}\rho_{I'}(E^{*'})W_{\alpha\chi}(J)}{\sum_{\chi''s''l''}^{'}T_{\chi''s''l''}^{J}+\sum_{\chi''s''l''I''}\int T_{\chi''s''l''}^{J}\rho_{I''}(E^{*''})dE_{\chi''}}. \quad (2.24)$$

Here α represents the entrance channel (projetile + target) and χ denotes the corresponding exit channel (ejectile + compound nucleus), E_{pro} is the kinetic energy of the projectile, and $\lambda\!\!\!^{-}_{\chi}$ represents the reduced wavelength in the incident channel. The channel spin is denoted by $\overrightarrow{s} = \overrightarrow{i} + \overrightarrow{I}$, where i and I are spin of the incident particle and the target, respectively. The compound-nucleus angular momentum and parity are represented by $J\pi$. The statistical-weight factor ω_{α}^{J} is calculated as $(2J+1)/[(2i+1)(2I+1)]$. In similar way, The spin of the exit-channel χ is $\overrightarrow{s'} = \overrightarrow{i'} + \overrightarrow{I'}$, where i' and I' are spin of the ejectile particle and the compound-nucleus, respectively. The relative orbital angular momentum in the entrance and exit channels are l and l', respectively. The transmission coefficients is $T_{\alpha ls}$ and the level density of spin I' of the residual nucleus at the excitation energy E^* is denoted by $\rho_{I''}(E^{*''})$. One has to account the energetically possible final channels (decay channels), and therefore in the denominator it should include the contributions from decays to discrete level region in the residual nucleus (the first sum in the denominator, $\sum'$) and the contributions from decays to regions described by a level density in the residual nucleus (the second sum in the denominator involving an energy integral of a product between transmission coefficients and level densities in the compound nucleus). By taking into account the correlations between the incident and the outgoing reaction channels, width fluctuation corrections $W_{\alpha\chi}(J)$ has been introduced into

the expression (Eq. (2.24)) [51, 32]. In writing Eq. 2.24, the parity quantum number has been suppressed except that of the compound nucleus. As a matter of fact, the level density principally depends on parity even though this dependency is usually neglected in the applications. The parity conservation must be respected for all sums over quantum numbers. More often, the width fluctuations $W_{\alpha\chi}(J)$ are unimportant, and assumed to be one. In such a case, for a given total spin and parity $J\pi$, in the expression there exist two separated terms, one of which contains the transmission coefficients $T_{\alpha ls}$ for the entrance channel, while the other $T^{J}_{\chi l's'}$ shows the decay probability into exit channel (e.g. gamma emission, neutron emission and fission, etc.); we sum over transmission coefficients of the exit channels divided by the denominator being all energetically possible decay channels. This leads to the remarkable assumption of the Hauser-Feshbach model, that the compound nucleus lose the memory of its formation, and that the conservation of the total spin and the parity of the compound nucleus system must be followed. In order to calculate the cross section employing Hauser-Feshbach formula, there require information, such as nuclear binding energy, spins and parities of both ground and excited states, γ-branching ratios for these states, nuclear level densities, and transmission coefficients for particles, photons, and fission. The developments of the requisite models and codes as well as the formulation of the recommended parameters [18] have been done with much effort. The method has been satisfactorily utilized to reproduce the available experimental cross section data. It is considered as complementary approach to estimate in the absence of experimental data.The uncertainties of the calculations are associated with the amount and quality of the available experimental constraints. For a compelling example, the measurements of the neutron resonance yields average level spacings and thus restrictions for the level densities near the neutron separation energy. Average radiative widths give information on the product of the level density and the γ-ray strength function related to the calculations of capture cross section. In the case of unavailable constraining data, one must depend on systematics or extrapolations, which remarkably brings additionally increased uncertainties in the calculated cross sections. It is valuable to microscopically calculate the relevant quantities, particularly, reactions on isotopes far from the valley of stability have been extensively calculated, but the uncertainties are difficult to quantify up to present.

In the surrogate method, the cross section expressed in Eq. (2.24) is actually the quantity of interest due to the fact that, for (n,f) cross section, one need to integrate over all final-state energies corresponding to the energies of the transition states built on the top of the fission barriers for fission. After the integration, the desired cross section thus becomes

$$\sigma_{\alpha\chi}(E_{pro}) = \sum_{J,\pi} \sigma^{CN}_{\alpha}(E^*, J, \pi) G^{CN}_{\chi}(E^*, J, \pi), \tag{2.25}$$

where $\sigma^{CN}(E^*)$ is the cross section of compound nucleus populated at the excitation energy E^* with spin and parity $J\pi$, and $G^{CN}_{\chi}(E^*, J, \pi)$ represents the branching ratio of the decay modes (channels) or decay probability χ. In typical applications, $\sigma^{CN}(E^*$ for individual spin is usually calculated by the optical model with reasonable accuracy, while the theoretical prediction of $G^{CN}_{\chi}(E^*, J, \pi)$ is often quite uncertain. The objective of the surrogate reaction is therefore to indirectly determine this quantity.

Equation (2.25) is just a simplified from of Eq. (2.24) in the absence of width-fluctuations corrections, in which the factorization indicates the explicit independence between the formation and the decay of the compound system. According to this independent hypothesis, the formation factor $\sigma^{CN}_{\alpha}(E^*, J, \pi)$ in Eq. (2.25) can

be replaced by a factor, which represents any other mechanism leading to the equilibrium of the compound nucleus as expected. For developing the surrogate-reaction method, this feature has been exploited.

In a surrogate experiment, the decay of a created compound nucleus is detected in coincidence with the detection of outgoing particle (ejectile). The probability for populating the compound nucleus, with particular value E^* and $J\pi$, is denoted by $F_\delta^{CN}(E^*, J, \pi)$. The quantity

$$P_{\delta\chi}(E^*) = \sum_{J,\pi} F_\delta^{CN}(E^*, J, \pi) G_\chi^{CN}(E^*, J, \pi), \tag{2.26}$$

which yields the decay probability into the channel χ can be experimentally, by measuring N_δ, the total surrogate events (number of ejectile scattering events), and $N_{\delta\chi}$, the number of the coincident events between the direct- reaction particle (ejectile) and the observable leading to identification of the corresponding exit channel:

$$P_{\delta\chi}^{exp}(E^*) = \frac{N_{\delta\chi}}{N_\delta \epsilon_\chi}. \tag{2.27}$$

Here ϵ_χ represents the detection efficiency of the exit channel χ for the reaction in which the ejectile is detected. The efficiency for the detection of the ejectile is not necessary to be determined due to fact that it has been canceled in the ratio. We note that $P_{\delta\chi}^{exp}(E^*)$ is in fact angular dependent, which arises from the fact that the population $F_\delta^{CN}(E^*, J, \pi)$ of the compound nucleus strongly relevant to the angular-momentum transferred in the surrogate reaction, and therefore the scattering angle of the ejectile.

In most of the applications in cross section determination of the surrogate method up to now, one has usually employed the approximations, such as the Weisskopf-Ewing (WE) limit approximation [73] of the Hausser-Feshbach theory and the surrogate ratio approach [25, 24]. Since the surrogate ratio approach is not the scope of our work, we will discuss only the Weisskopf-Ewing limit approximation.

In this Weisskopf-Ewing limit approximation, the branching ratios are assumed to be independent of the spin and parity $J\pi$, $G_\chi^{CN}(E^*, J, \pi)$ –> $G_\chi^{CN}(E^*)$, and the cross section expressed in Eq. (2.25) for the reaction of interest becomes

$$\sigma_{\alpha\chi}^{WE}(E_{pro}) = \sigma_\alpha^{CN}(E^*) G_\chi^{CN}(E^*), \tag{2.28}$$

where $\sigma_\alpha^{CN}(E^*)$ is the cross section for populating the compound nucleus at excitation energy E^*,

$$\sigma_\alpha^{CN}(E^*) = \sum_{J\pi} \sigma_\alpha^{CN}(E^*, J, \pi), \tag{2.29}$$

which can be calculated by employing the reasonable optical model. The great simplification [$F_\delta^{CN}(E^*, J, \pi) \approx 1$] has been taken in the Weisskopf-Ewing limit such that the branching ratios $G_\chi^{CN}(E^*)$ can be directly determined from the measured coincidence probabilities $P_{\delta\chi}^{exp}(E^*)$,

$$P_{\delta\chi}^{exp}(E^*) = G_\chi^{CN}(E^*), \tag{2.30}$$

and the cross section of interest given as

$$\sigma_{\alpha\chi}^{WE}(E_{pro}) = \sigma_\alpha^{CN}(E^*) P_{\delta\chi}^{exp}(E^*). \tag{2.31}$$

The correlations between the kinetic energy of the projectile E_{pro} and the excitation energy of the compound nucleus E^* can be written as

$$E_{pro} = \frac{A_{tar} + A_{pro}}{A_{tar}} \times (E^* - S_{par}), \tag{2.32}$$

where A_{tar} and A_{pro} are the number of nucleons in the target and the projectile, respectively, and S_{par} denotes the energy cost to remove a particle from the compound nucleus (separation energy).

Chapter 3

Experiments

In this chapter, we describe the beam production and experimental setup used in this work. Fission of nuclei produced in the MNT channels of the ^{18}O + ^{237}Np reaction was studied by using the ^{18}O beam with the energy of 162 MeV and intensity of 0.5 pnA, supplied by the JAEA tandem accelerator in Tokai, Japan.

3.1 Accelerator

The accelerator began its operation in 1982, and serves for the fundamental researches using heavy ion beam, concentrated mainly in the domains of nuclear physics, nuclear chemistry, material science and so on. Figure 3.1 shows an outside view of the tandem accelerator facility building, and figure 3.2 illustrates the schematic representation of the accelerator. The tandem is an electrostatic accelerator type of terminal voltage which can be increased up to 18 MV. This accelerator is composed of several main parts which are ion sources, pre-acceleration tube, mass analyzing magnet, accelerator tubes, an electron striper, insulation gas (SF6), a charge analyzing magnet, an energy analyzing magnet. There are two kinds ion sources, a negative ion source and the positive ion source (therminal (ECR) ion source). Many kinds of available ions ranging from hydrogen to bismuth can be used. Some negative ions, e.g ^{18}O used in our experiment, can be extracted from the negative ion source with the injection energy of 50–350 keV, and then pre-accelerated by passing through the pre-acceleration tube, see Fig. 3.2. The negative ions are bent and mass-purified by a mass analyzing magnet and accelerated upward by the negative (low energy) accelerator tube with the terminal voltage U = 18 MV. The electrons of these accelerated-negative-ions were removed by the electron stripper (carbon foil), and then become positive ions with charge (q = 8e) accelerating again downward by the positive (high energy) accelerator tube with the same terminal voltage as the negative accelerator tube. While accelerating negative ions, one gets its energy of 1 terminal voltage U (e.g. 18 MeV if U = 18 MV), then after passing the stripper, its charge state becomes 'q', and accelerating down will give the extra energy q$\times$U. Thus, its total energy is (q+1e)$\times$U where "e" is the electron charge. In the numerical application, the ^{18}O beam energy employing in our experiment was determined to be 162.0 MeV with q = 8e and U = 18 MV. Finally, the mono-energetic beam is exported to the experimental room after analyzing by the energy analyzing magnet. The extracted beam for the experiments has high accuracy (100 keV) and of 1 mm in diameter. For the detailed information, visit the JAEA official website [3].

FIGURE 3.1: The JAEA accelerator has been installed inside the building. The photo from JAEA website [3].

3.2 Target

The target, shown in Fig. 3.3, was made by electro-deposition of ^{237}Np material with a thickness of 76.3 μg/cm^2 on a natural nickel backing (300 μg/cm^2). The impurity in the ^{237}Np target is negligible. Note that the target purity is crucial in this measurement technique since if the impurity is significant, scattering events from the impurity elements will be contaminated in the single spectrum as shown in Fig. 4.9(a). It leads to the wrong deduction of fission barrier height and the fission probability. To quantify contribution from the backing (i.e., interaction of ^{18}O with ^{nat}Ni) to the measured data, a dummy ^{nat}Ni target (300 μg/cm^2 thick) was used with identical beam and geometry conditions. The target was placed at center of the detection system, see Fig. 3.6(a). The target was prepared with a help of a chemistry group in the heavy-element nuclear science (HENS) at Japan Atomic Energy Agency (JAEA). To avoid the radioactive contamination, the target was transferred from the preparation room to the vacuum chamber (Fig. 3.4 (c)) in the experimental room by putting in the target-handling container (Fig. 3.4 (a)). The target was inserted into and released from the container via a target-mounting ladder (Fig. 3.4 (b)) by attaching to the target holder connected with the target-catcher. The container was connected to the target handling shaft, as indicated by the yellow arrow, which can slided down and up to adjust to the beam level by a remote controller. The target status can be observed by the camera viewer mounted to the camera view port. We note that many targets can be attached at the same time with this target holder.

3.3 Detection system

The schematic representation of the detection system is shown in Fig. 3.5 and 3.6. The ejectile was detected by the $\Delta E - E$ silicon telescope (cf. Fig. 3.6(b) and its photo (c)), while the fission fragments were detected by two pairs of the multi-wire proportional counters (MWPCs, cf. Fig. 3.6(a) and one of the their photos (d)). All the detectors

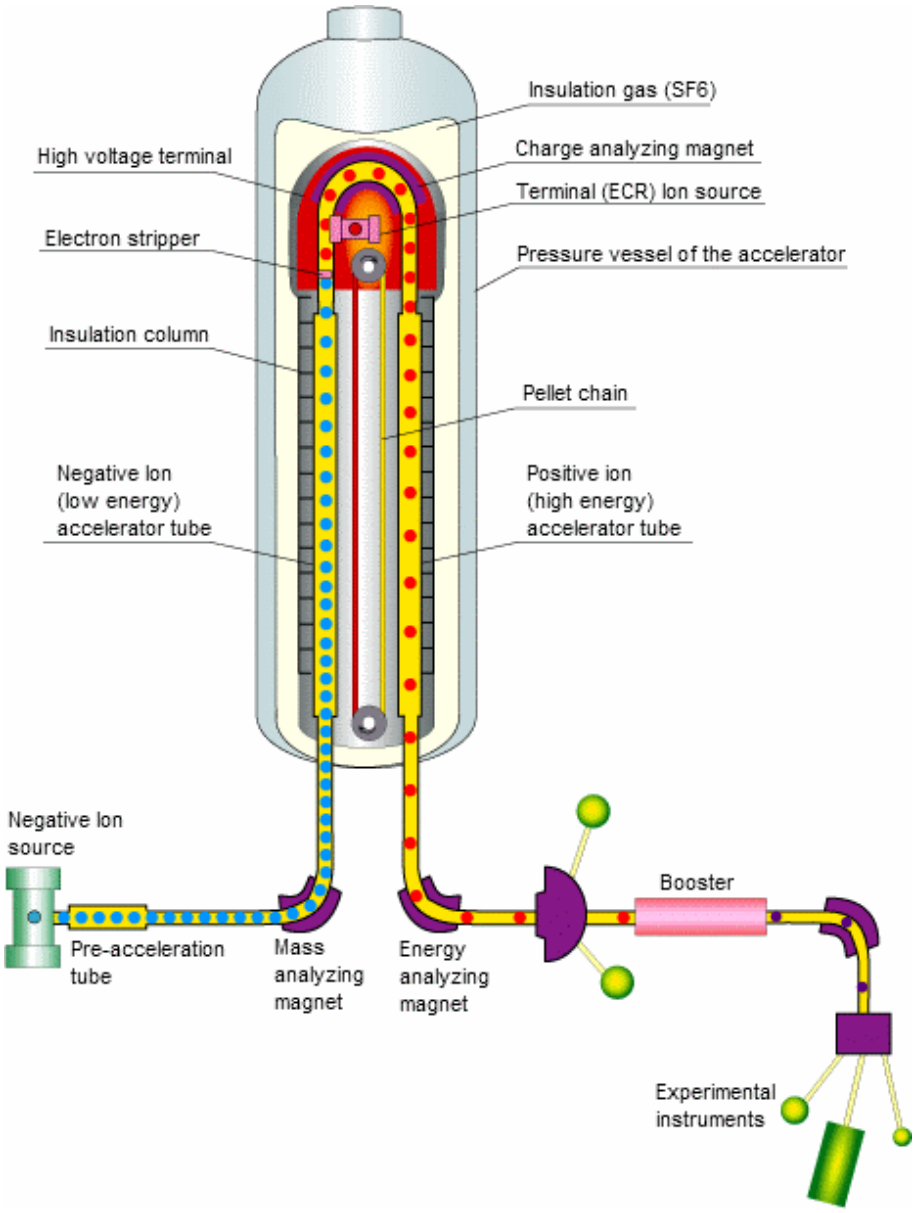

FIGURE 3.2: The representation of the JAEA tandem accelerator structure. The photo from JAEA website [3].

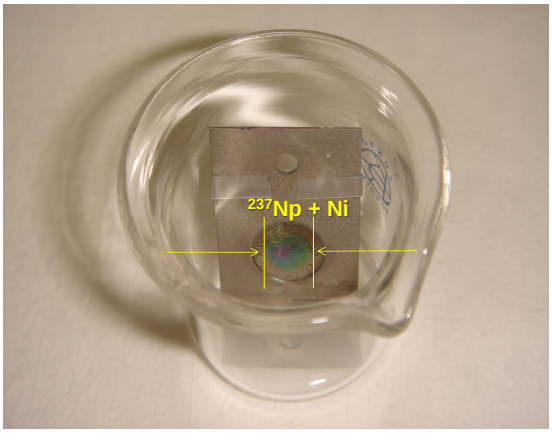

FIGURE 3.3: The ^{237}Np target electro-deposited on a nickel backing is shown.

were installed inside the vacuum chamber of 1 m in diameter with the pressure in the order of 10^{-15} Pa as shown in Fig. 3.5.

3.3.1 Si ΔE-E telescope detector

The telescope was positioned in a forward direction (of the beam) at a distance of 80 mm from the target. The telescope consists of ten Si ΔE detectors and a Si E detector, Fig. 3.6(b). Each ΔE detector has a thickness of 75 $\pm$ 1 μm and the azimuthal angle acceptance of $\Delta\ \varphi$ = 22.5^0. The E detector is divided into 16 annular stripes of the 300 μm-thick each to detect the ejectiles at different scattering angles. The inner and outer radius of the detector are 24.0 mm and 48.0 mm corresponding to scattering angles between 16.7^0 and 31.0^0, respectively. The position of the ΔE–E detector had been chosen such that the lowest acceptant angle must be reasonably higher than the grazing angle $\theta \approx 12.93^0$ for ^{18}O + ^{nat}Ni reaction with the beam energy of 162.0 MeV. In this way, it permits to avoid the disturbance from too much current generated by the elastic scattering of ^{18}O on the properly functioning of the telescope. The energy of an ejectile, E_{total}, was measured as a sum of energy loss, ΔE, generated by passing through one of ten ΔE detectors and the remaining energy (residual energy), E_{res}, totally deposited in one of the 16 strips of the E detector ($E_{total} = \Delta E + E_{res}$). The telescope serves not only for measuring the ejectile energy but also for its identification, and therefore it allows for identifying the corresponding compound nucleus.

3.3.2 Multi-Wires Proportional Counters (MWPCs)

Each MWPC (200$\times$200 mm^2), see Fig. 3.6(a) and (d), has 100 vertical and 100 horizontal tungsten wires coted with gold (two successive wires combined as one). Between the vertical and horizontal wires, there is a gold plate (2 μm-thick) used as a cathode. It has a mylar window of 3 μm thick. For this experiment, each MWPC was placed at the distance of 224 mm which is measured between the center of the cathode and the target. It covers the solid angle of 0.67 sr each. During the operation, the isobutane gas is filled and continuously flowed inside the MWPC with the pressure set to be 1.5 Torr. See also [55] for the description of the operation conditions.

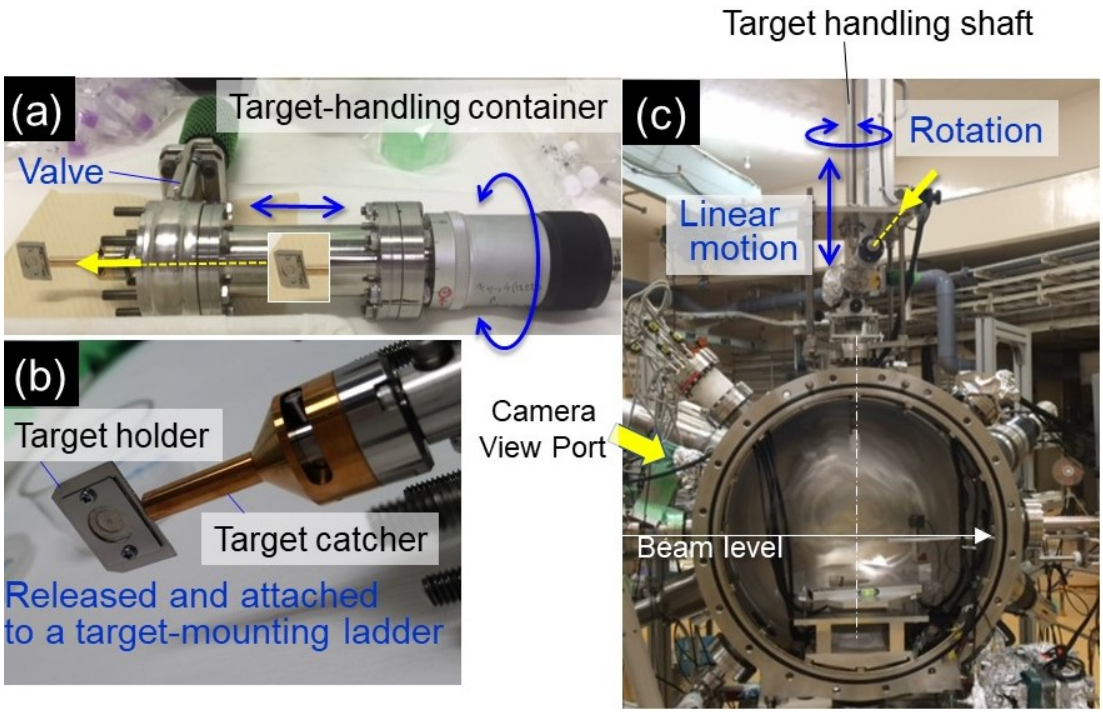

FIGURE 3.4: The target was transferred to the vacuum chamber (c) by putting in the target-handling container (a); and the target was attached to the target-mounting ladder (b).

3.4 Acquisition system

The main acquisition system was located in the control room, and its photo is shown in Fig. 3.7. The charges were independently collected for ΔE, E and MWPCs detectors. The coincidence events between these detectors were selected based on the timestamps (one timestamp = 200 ns). During the operations, ΔE, E and MWPCs were biased with $\sim$ 10–20 V, -50 V and $\sim$ 400 V, respectively. The leaked currents were observed to be $\sim$ 0.10–0.60 μA for ΔE and E, respectively.

3.4.1 Acquisition system of a Multi-Wires Proportional Counter (MWPC)

In our experiment, only the cathodes were used. Note that the wires are employed for the fission fragment mass distribution and the total kinetic energy of the fission fragments (TKE) measurements. An example of the schematic representation of the acquisition system for a cathode (Cath) of a MWPC is illustrated in Fig. 3.8. The main acquisition devices were composed of three fast amplifiers, a CFD standing for constant fraction discriminator, a divider, a gate generator (ORTEC G.G) and a QDC (Charge to Digital Converter). One fast amplifier (Philip Science company) located in the experimental room to bring the signals to the control room while two others (CAEN company) placed in the control room to amplify logic signals. The CFD, made by ORTEC, with a delay of 10 ns converts an analog signal to a logic signal and to discriminate the noise below setting threshold. Analog signals can be checked by an oscilloscope. After that the signals were split by two, one was amplified again by two fast amplifier and the other was sent to the CFD. After passing through the CFD, the digital signal was slit again by a divider, and these split signals were sent to a scalar to display counting rates and to the G.G to make QDC gate of 50 ns. The analog signal

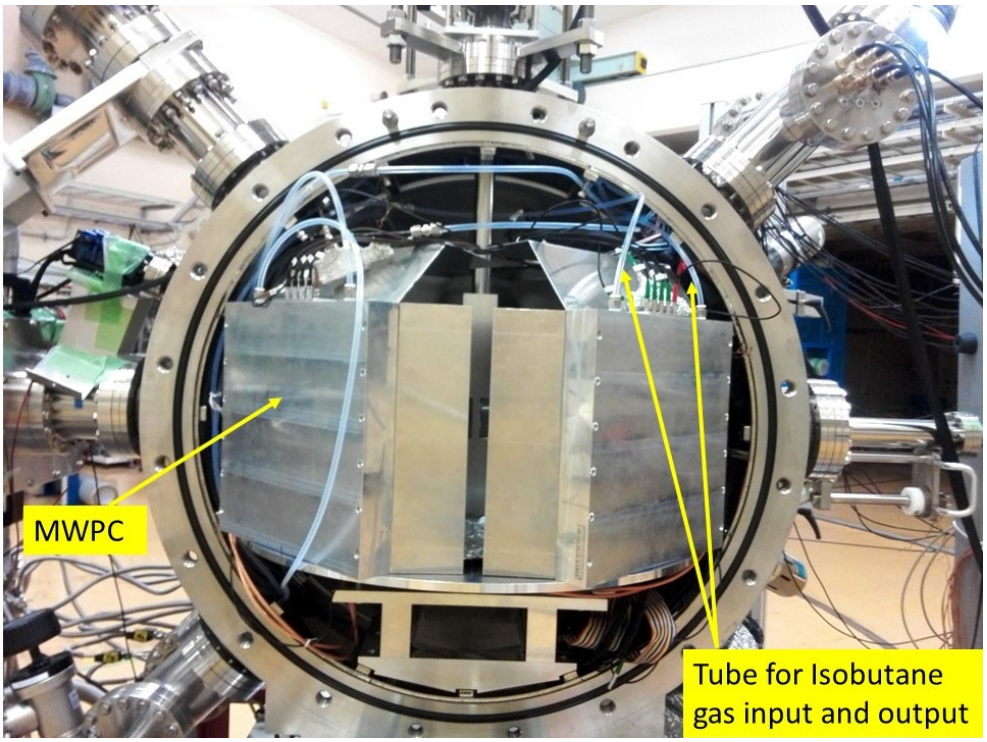

FIGURE 3.5: The $\Delta E - E$ silicon telescope, the MWPCs and the target were placed inside the vacuum chamber of 1 m in diameter with the pressure in the order of 10^{-15} Pa. For MWPCs, the input and output for the isobutane gas.

after delayed 200 ns was sent to a QDC signal (sig.). If this signal is inside the QDC gate, this signal is accepted. Otherwise, it was rejected.

3.4.2 Acquisition system of a ΔE detector

Acquisition system schematic representation of a ΔE detector out of 10 is shown. ΔE detectors were divided into two sides, A (ΔE1, 2, 3, 4 and 6) and B (ΔE7, 8, 9, 10 and 12), see Fig. 3.9. Note that number 5 and 11 were empty. The signal processing is exactly the same for all the detectors, and the acquisitions of these two sides connected by a logic "OR". For an example, the system of a ΔE1 was constituted of two amplifiers (MDS-8 amp and 778 amp), a CFD, two scalars, two FI/FO (Fan In/Fan Out) and PDC signal (PDC sig.). A negative signal was sent to FE02 PDC (Peak to Digital Converter) and also sent to CFD after amplifying again by a fast amplifier (778 amp). The signal was extracted to display counting rates by a scalar and to a ORTEC G.G to make a PDC common gate of 2 μs (FE02 PDC com. gate). PDC signals were accepted only if they inside the common gate.

3.4.3 Acquisition system of an E detector

Acquisition system schematic representation of a E detector is shown. There were also two sides, A (EA1, 2, ..., 16) and B (EB1, 2, ..., 16), corresponding to sides of ΔE detectors, see Fig. 3.10. All strips for each side were connected to the common devices which are an amplifier (N568B amp), a divider a LED (Leading Edge Discriminator), a CFD two FI/FOs. Both sides were connected to the common devices, such as two FI/FO, two ORTEC G.G2 and a coincidence (coin.). These components have already

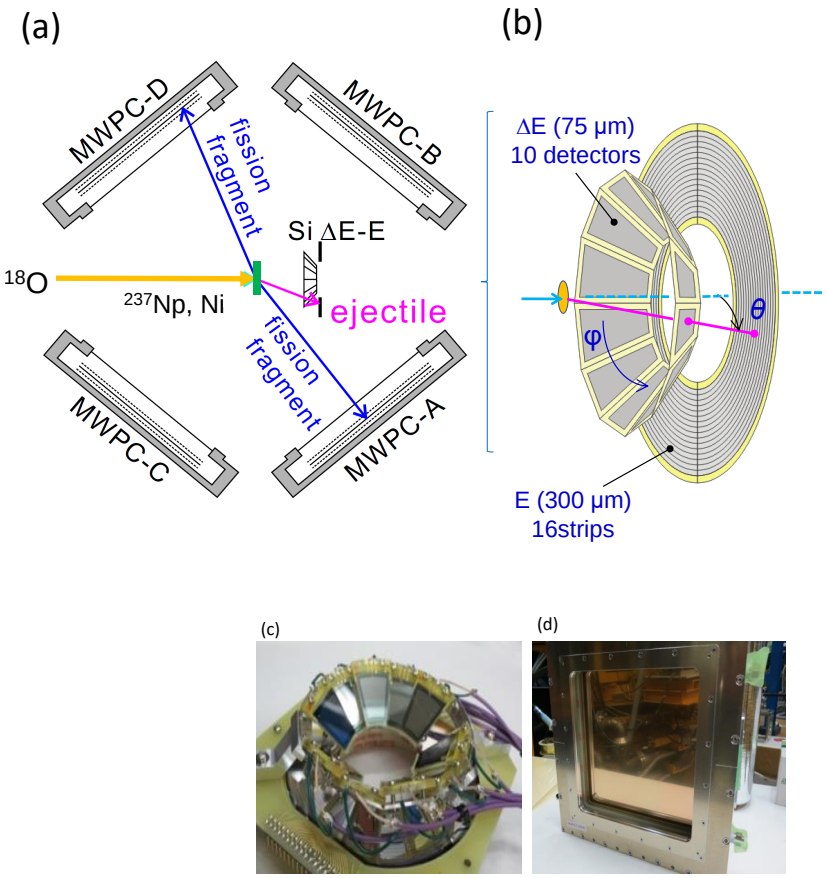

FIGURE 3.6: Schematic representation of the experimental setup. Panel (a) shows the arrangement of the four MWPCs surrounding the ^{237}Np(+Ni) target used to detect the fission fragments, and the $\Delta E - E$ telescope employed to identify the ejectiles. Panel (b) gives the expanded view of the $\Delta E - E$ detector. Panels (c) and (d) illustrate the images of telescope detector and MWPC, respectively.

been described for ΔE1 detector, except LED which is used for noise rejections. The signal processing is also similar to dE detector. Additionally, we made a veto via coin. to reject signals generated by two nearby strip at the same time when a particle hits one strip near the boundary, and a signal also generated in a nearby strip at the same time.

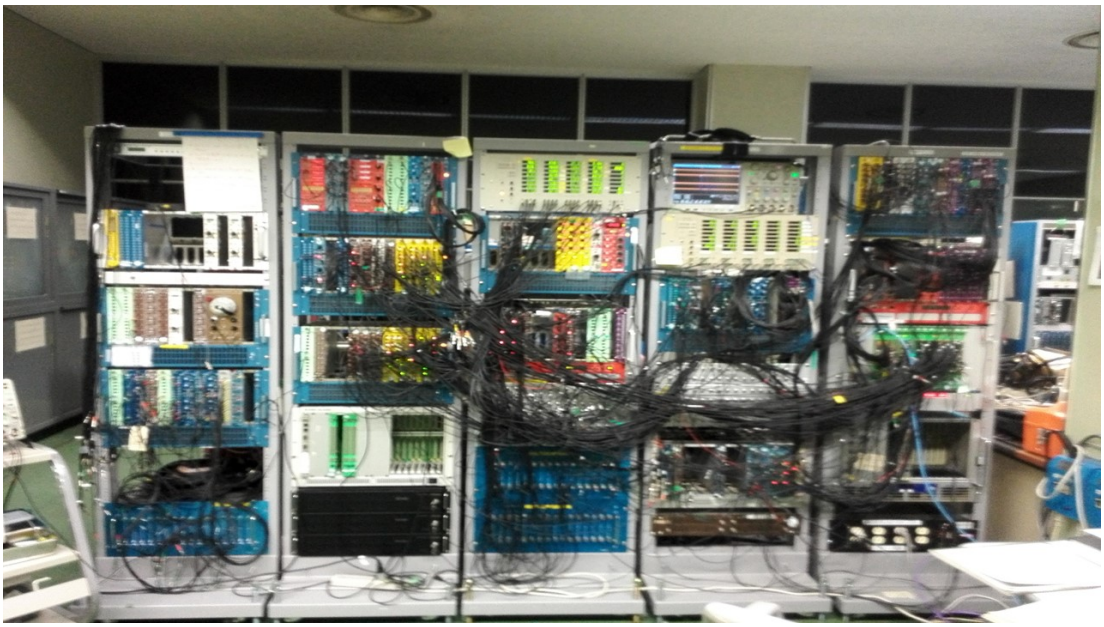

FIGURE 3.7: The photo of the main acquisition system is located in the control room.

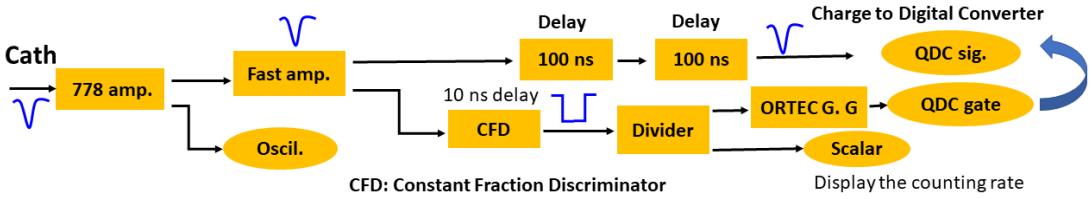

FIGURE 3.8: Acquisition system schematic representation of the cathode (Cath) of a Multi-Wire Proportional Counter is shown. There are also acquisition systems for the wires but only the cathode is presented here since it was the only requirement for our work.

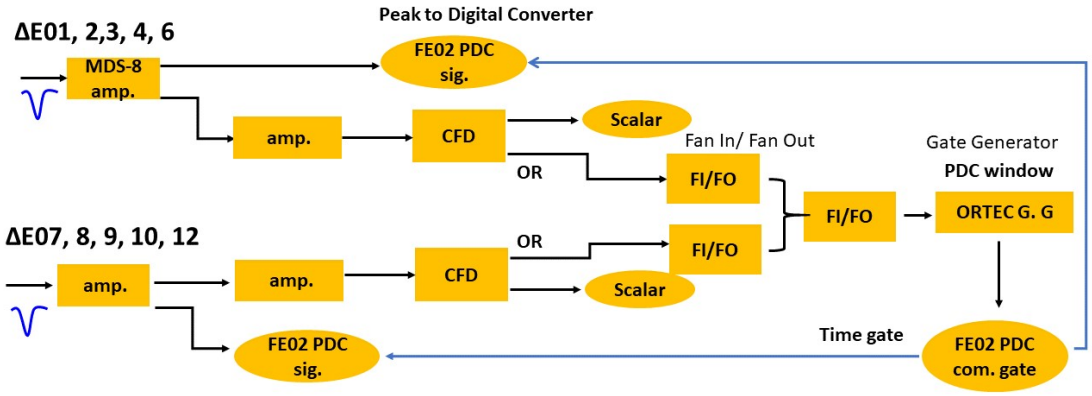

FIGURE 3.9: Acquisition system schematic representation of a ΔE detector out of 10 is shown. ΔE detectors were divided into two sides, A and B. The acquisitions of these two sides connected by a logic "OR".

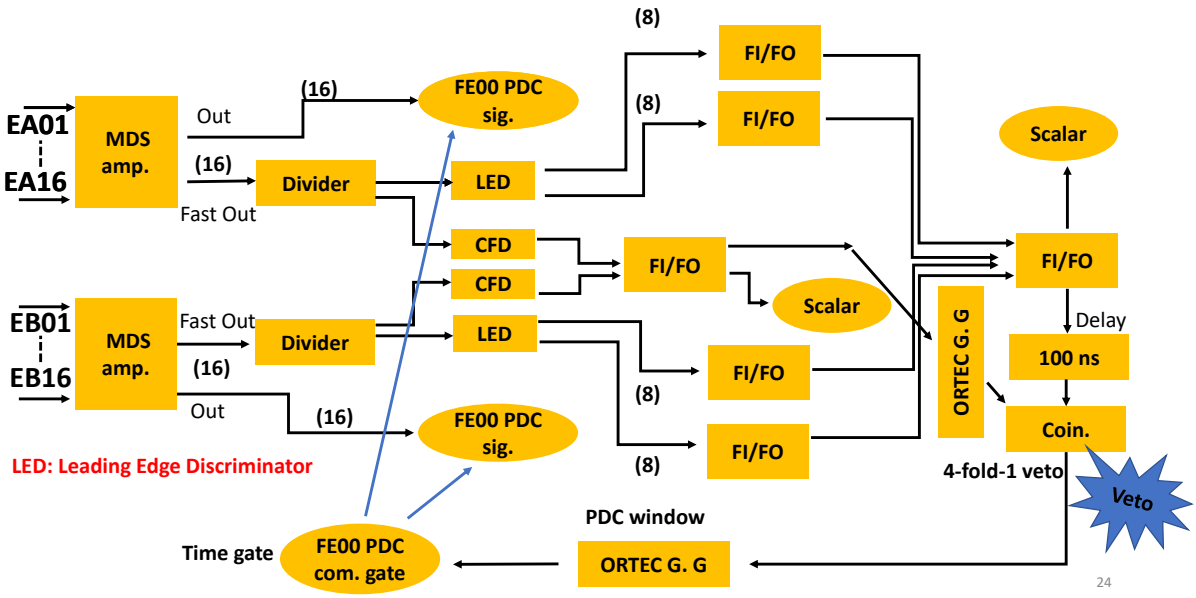

FIGURE 3.10: Acquisition system schematic representation of a E detector is shown. There were also two sides (A and B) corresponding to sides of ΔE detectors.

Chapter 4

Data analysis

We show, in this chapter, the process of the data analysis in order to derive the fission probability and the fission barrier heights.

4.1 Energy Calibration

The energy calibrations were performed for both ΔE and E detector using a software LYSE++ [45] to calculate the energy loss and the energy remaining of an ejectile passing through ΔE. The energy calibrations were performed as following: 1D spectra (the uncalibrated spectra) have been plotted for ΔE (Fig. 4.1) and E (Fig. 4.2) (the upper-spectra for ^{18}O + ^{237}Np(+^{nat}Ni) and the lowers for ^{18}O +^{nat}Ni reactions). Figures. 4.1 and 4.2 shows the energy distribution (but express in channels) of the ejectiles provided by detectors ΔE1 and E1, respectively, in a pair ΔE1–E1. These channels need to be converted into energies. For the conversion, we calculated, first of all, the energy loss ΔE_{los} of the elastic scattering of ^{18}O which penetrates a ΔE detector with different effective thickness $L(\theta)$ corresponding to the various scattering angles θ. In order to calculate the energy loss and remaining by LISE++, it requires the input information, such as the effective thickness and the elastic scattering energy $E_{el}(\theta)$ of ^{18}O. As illustrated in Fig. 4.3, the effective thickness was computed as $L(\theta) = d/sin(47.8^0 + \theta)$. The elastic scattering energy $E_{el}(\theta)$ was determined by using the conservation law of linear momentum and energy. The calculation results of $L(\theta)$, $E_{el}(\theta)$, ΔE_{los} and E_{rem} are indicated in Table 4.1. Finally, the calibrations were achieved by the energy re-normalizations according to ΔE = $[\Delta E(ch) \times \Delta E_{los})]/\Delta E_{av}$ and E_{re} = $[E(ch) \times E_{rem})]/E_{av}$ for Δ E and E detector, respectively, in every ΔE-E pair. ΔE_{av} and E_{av} are the average energies obtained by fitting the 1D spectra (e.g. Figs. 4.1 and 4.2) for ΔE and E detector with the Gaussian function (solid.. curve), respectively.

4.2 Particle Identification Plots (PID)

Examples of particle identification plots (PID) made using the ΔE-E detector are shown in Fig. 4.4 and 4.5. Figure 4.5 (a) and (b) show the registered ejectile data for the ^{237}Np(+^{nat}Ni) and dummy ^{nat}Ni targets, respectively. These plots show the energy loss ΔE versus the total energy E of the ejectiles. The different (A, Z) lines associated with specific ejectiles are well separated, making it possible to identify specific reaction channels clearly. On each plot, we applied banana-like gates(Fig. 4.4 red curves), using a functional to select the charge and mass of the ejectile in the $\Delta E - E$ telescope by using the method outlined in [67]. We note that there are 10×16 PID plots in total, which correspond to the number of ΔE and E combinations. For deducing the fission probability and fission barrier height, only strips 4–10 were taken due to the poor statistic for rests. The signals were strongly disturbed by the high elastic scattered

TABLE 4.1: The number of strips, the scattering angle θ corresponding to each strip with respect to the beam direction, the effective thickness $L(\theta)$ of a ΔE detector traversed by the ejetiles according to each strip, the elastic scattering energy $E_{el}(\theta)$ of the ejectile ^{18}O corresponding to each scattering angles and the energy loss E_{los} and energy remaining E_{rem} of ^{18}O after passing through ΔE with different effective thicknesses are presented.

# strips	θ (degree)	$L(\theta)(\mu m)$	$E_{el}(\theta)$ (MeV)	$E_{los}(MeV)$	$E_{rem}(MeV)$
1	17.2	82.75	160.90	47.49	113.42
2	18.1	82.16	160.79	47.13	113.65
3	18.99	81.60	160.67	46.80	113.87
4	19.88	81.07	160.54	46.49	114.05
5	20.77	80.57	160.41	46.20	114.21
6	21.67	80.09	160.27	45.92	114.35
7	22.56	79.63	160.13	45.66	114.47
8	23.45	79.20	159.98	45.42	114.56
9	24.35	78.79	159.83	45.20	114.63
10	25.24	78.41	159.67	44.99	114.68
11	26.13	78.05	159.50	44.80	114.71
12	27.03	77.71	159.33	44.62	114.71
13	27.92	77.39	159.16	44.46	114.70
14	28.81	77.10	158.98	44.32	114.67
15	29.71	76.82	158.80	44.18	114.62
16	30.6	76.56	158.61	44.06	114.55

events of ^{18}O generated by ^{18}O + ^{237}Np reaction in strips 1–3, while strips 11-16 were shadowed by the frame of the ΔE detectors.

4.3 Excitation Energy Determination

To calculate the excitation energy of the compound nucleus, we apply the conservation law of linear momentum and energy. By assuming that the target nucleus was at rest with respect to laboratory frame of the reference, see Fig. 4.7, the conservation of linear momentum can be written as

$$\overrightarrow{P}_{pro} = \overrightarrow{P_{ej}} + \overrightarrow{P_{re}}, \tag{4.1}$$

where $\overrightarrow{P}_{pro}$, $\overrightarrow{P_{ej}}$ and $\overrightarrow{P_{re}}$ represent the momentum of the projectile, the ejectile and the residual (compound) nucleus, respectively. We square the $\overrightarrow{P}_{pro}$, we obtain

$$P_{pro}^2 = P_{ej}^2 + P_{re}^2 - 2P_{pro}P_{ej}cos(\theta). \tag{4.2}$$

Here θ is the scattering angle compared to the beam direction, see Fig. 4.6 or 4.7. The conservation of energy of the colliding system is written as

$$m_{pro}c^2 + E_{pro} + m_{tar}c^2 = m_{ej}c^2 + E_{ej} + E_{ej}^* + m_{CN}c^2 + E_{CN} + E_{CN}^*, \tag{4.3}$$

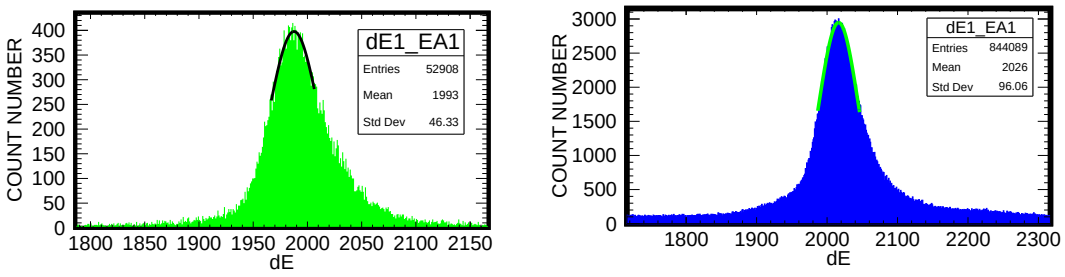

FIGURE 4.1: The above spectrum, the energy distribution (express in channels) $\Delta E(ch)$ of the ejectiles provided by detector ΔE1 in the combination with the segment E1 for ^{18}O + ^{237}Np (this spectrum was plotted using only one among 518 data files). The above spectrum, the energy distribution (express in channels) $\Delta E(ch)$ of the ejectiles provided by detector ΔE1 in the combination with the segment E1 for ^{18}O + ^{58}Ni (this spectrum was plotted using 21 data files). Green curves are Gaussian fitting.

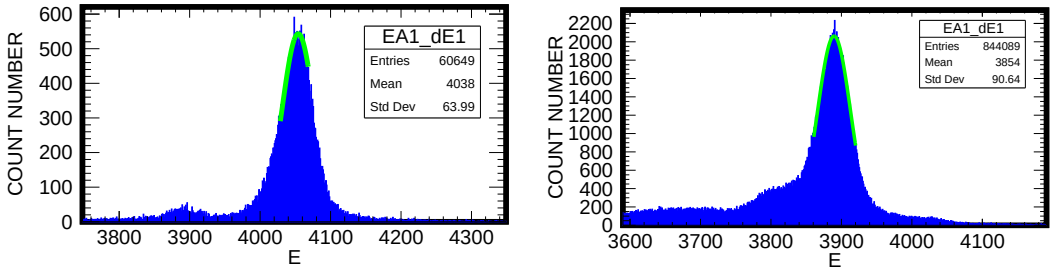

FIGURE 4.2: The above spectrum, the energy distribution (express in channels) $E(ch)$ of the ejectiles provided by detector E1 in the combination with ΔE1 for ^{18}O + ^{237}Np (this spectrum was plotted using only one data file). The below spectrum, the energy distribution (express in channels) $E(ch)$ of the ejectiles provided by detector E1 in the combination with ΔE1 for ^{18}O + ^{58}Ni (this spectrum was plotted using 21 data files). Green curves are Gaussian fitting.

where m_{pro}, m_{tar}, m_{ej} and m_{CN} are the rest masses of the projectile, the target, the ejectile and the compound nucleus, respectively. c is the peed of light. E_{pro}, E_{ej} and E_{CN} are the kinetic energy of the projectile, the ejectile and the compound nucleus, respectively, while the E^*_{ej} and E^*_{CN} represent the excitation energy of the ejectile and the compound nucleus, accordingly. For the interpretation of the experimental data, hereafter we assume that the excitation energy of the exit channel is given to the recoiled nucleus (E^*_{ej} = 0). By introducing the Q value which is equal to $931.5 \times ((m_{pro} + m_{tar}) - (m_{ej} + m_{CN}))$ (MeV) and the relation $E = P^2/2m$, the excitation of the compound nucleus is given as

$$E^*_{CN} = Q + E_{pro} - E_{ej} - E_{CN}. \tag{4.4}$$

Here E_{pro} is the beam energy (162.0 MeV) and E_{ej} is equal to E_{total}, while E_{CN} expresses as

$$E_{CN} = \frac{1}{m_{CN}} \left(m_{pro}E_{pro} + m_{ej}E_{ej} - 2\sqrt{m_{pro}m_{ej} \times E_{pro}E_{ej} \times cos(\theta)} \right) \tag{4.5}$$

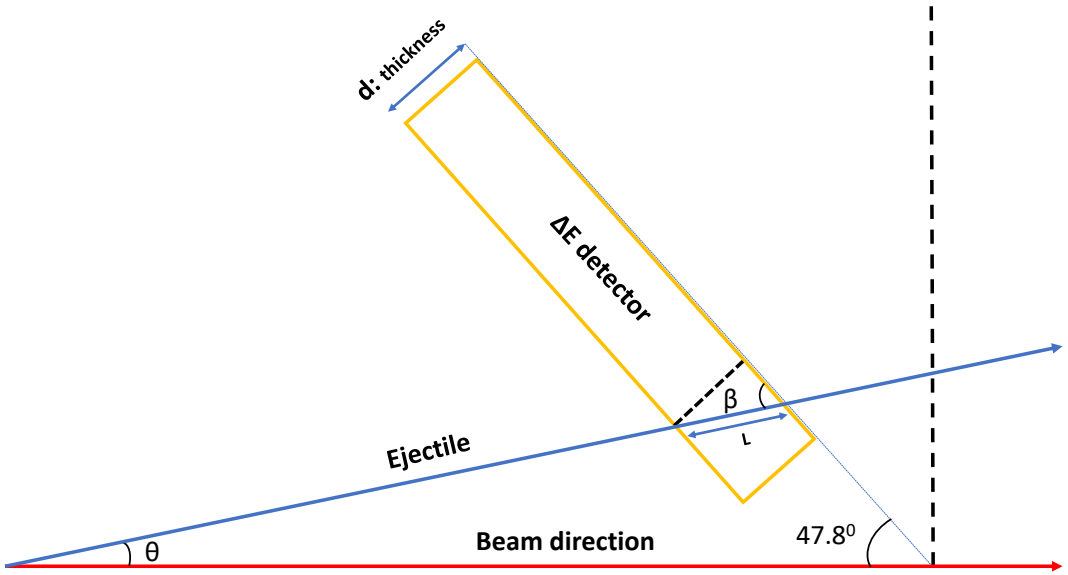

FIGURE 4.3: The method to calculate the effective thickness L of ΔE detector penetrated by the ejectile is indicated. ΔE detectors have a cone angle of 47.8^0 and a thickness of 75 ± 1 μm. The ejectile scattering angle with respect to the beam direction is denoted by θ.

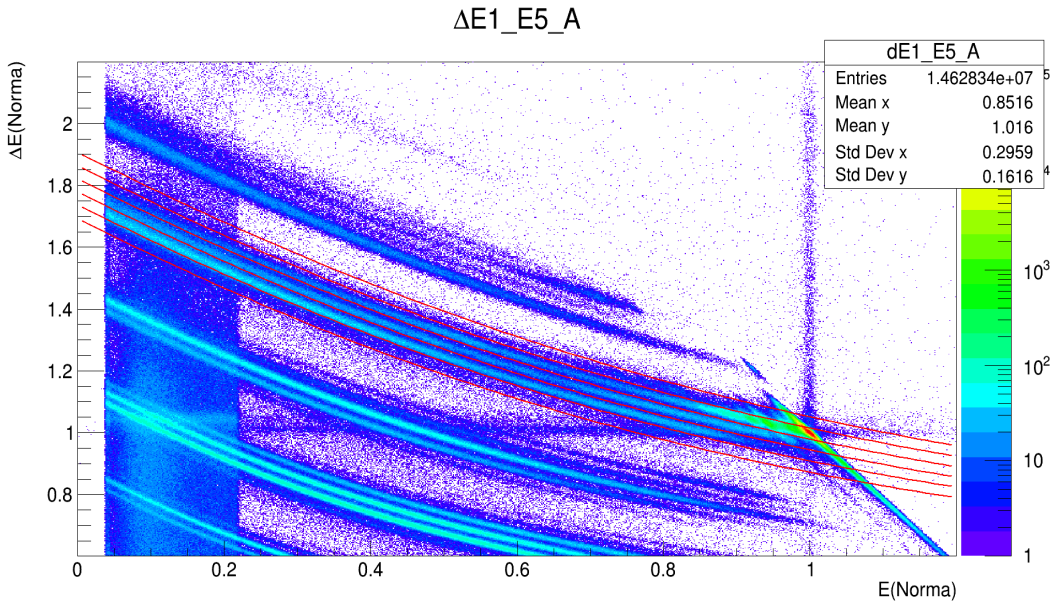

FIGURE 4.4: Energy loss ΔE versus residual energy E obtained from the ΔE-E telescope for a combination of ΔE1 and E5. It was obtained using ^{18}O + ^{237}Np(^{nat}Ni). The elastic scattering energies were normalized to 1 for both ΔE and E.

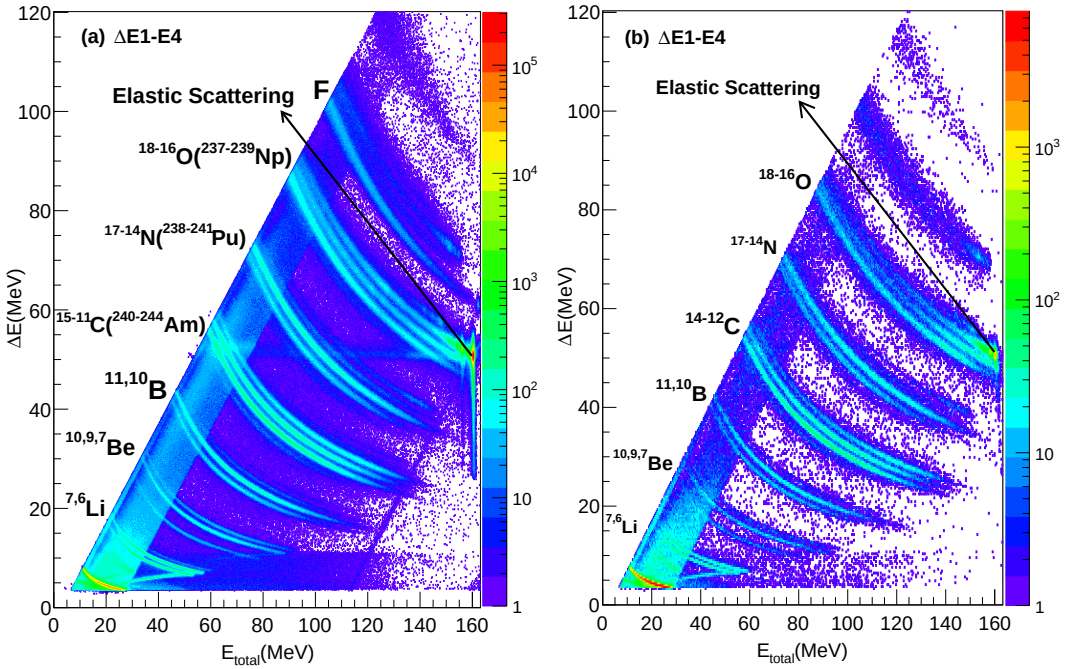

FIGURE 4.5: Energy loss versus total energy obtained from the $\Delta E - E$ telescope. Panel (a) and (b) are obtained using $^{18}O + ^{237}Np(+^{nat}Ni)$ and $^{18}O + ^{nat}Ni$, respectively, with the beam dose of 2.0×10^6 and 8.2×10^5 each.

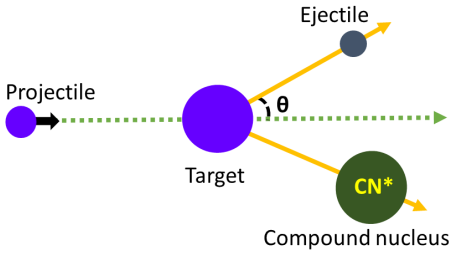

FIGURE 4.6: The kinematic representation of the interaction between heavy projectile and nucleus target. An exited compound-nucleus and an ejectile scattered at angle θ are indicated.

4.4 Uncertainty Analysis

There are two type of uncertainty in this work, such as the excitation energy uncertainty due to the measuring system and the statistical uncertainty.

Let's have a function of multi-variables y = f(x_1, x_2, ..., x_n), its uncertainty can be calculated as

$$\begin{aligned}(\Delta y)^2 =&(\frac{\partial y}{\partial x_1}\Delta x_1)^2+(\frac{\partial y}{\partial x_2}\Delta x_2)^2+(\frac{\partial y}{\partial x_3}\Delta x_3)^2...+(\frac{\partial y}{\partial x_n}\Delta x_n)^2+\\ &2(\frac{\partial y}{\partial x_1})(\frac{\partial y}{\partial x_2}).\text{Cov}\,(x_1;x_2)+2(\frac{\partial y}{\partial x_1})(\frac{\partial y}{\partial x_3}).\text{Cov}\,(x_1;x_3)+\\ &2(\frac{\partial y}{\partial x_2})(\frac{\partial y}{\partial x_3}).\text{Cov}\,(x_2;x_3)+.....,\end{aligned} \tag{4.6}$$

where Δx_1, Δx_2, ... and Δx_n indicate the uncertainty of the variables x_1, x_2, ... and

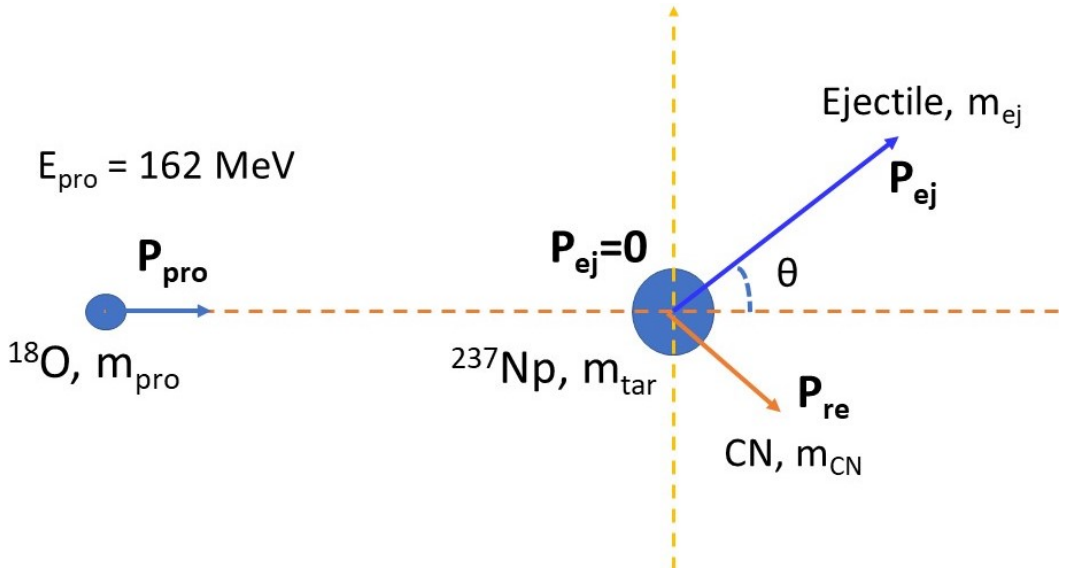

FIGURE 4.7: The kinematic representation of linear momentum for the colliding system with an ejectile scattered at angle θ are indicated.

x_n, respectively. "Cov" represent the covariance. In Eq. (4.4), Q, E_{pro}, E_{ej} and E_{CN} are all independent physical quantity and by applying Eq. (4.6), the covariance terms vanish, and the excitation energy uncertainty can therefore be derived as

$$\Delta E^*_{CN} = \sqrt{(\Delta Q)^2 + (\Delta E_{pro})^2 + (\Delta E_{ej})^2 + (\Delta E_{CN})^2}, \tag{4.7}$$

where ΔQ is the uncertainty of Q value deduced from the uncertainty of masses of the colliding system, and ΔE_{pro}, ΔE_{ej} and ΔE_{CN} are the kinetic energy uncertainties of the projectile (beam), the ejectile and the compound nuleus, respectively. ΔE_{pro} = 100 keV. ΔE_{ej} = 0.38 MeV is obtained as the energy resolution (FWHM = 0.9 MeV) of the ΔE detector divided by 2.634. The FWHM was derived from the fit to the elastic scattering peak ($\sim$ 160 MeV) of the total energy spectra, see an example in Fig. for both ^{18}O + ^{237}Np (blue) and ^{18}O + ^{nat}Ni (red). ΔE_{CN} can also be calculated according to Eq. (4.6).

On the right hand side of Eq. (4.7), by numerical applications, the most dominant term is ΔE_{ej}, and the rests can be negligible. As a result, the uncertainty of excitation energy is that of the ejectile kinetic energy ($\Delta E^* \approx \Delta E_{ej}$ = 0.38 MeV).

To plot histograms with the excitation distribution on the horizontal axis, e.g. Fig. 4.9, one needs to compromise between the bin size and the excitation energy uncertainty. Thus, the histogram bin size should be around 0.8 MeV (0.4 MeV of bin uncertainty), which is roughly twice the the uncertainty of the excitation energy. Otherwise, the uncertainty of excitation energy will be ignored if one choose bin size considerably smaller than 0.8 MeV.

For every E^* value, fission probability P_f can be extracted from the recorded data with help of the following expression (from Eq. (2.27) for the fission channel):

$$P_{\mathrm{f}}(E^*) = \frac{N^{\mathrm{coin}}_{\mathrm{ej}}(E^*)}{N^{\mathrm{sing}}_{\mathrm{ej}}(E^*)\varepsilon(E^*)} \tag{4.8}$$

Here, $N^{\mathrm{coin}}_{\mathrm{ej}}$ is a number of the selected ejectiles in coincidence with both fission fragments, $N^{\mathrm{sing}}_{\mathrm{ej}}$ is the total number of the selected ejectiles (=singles), and ε is the

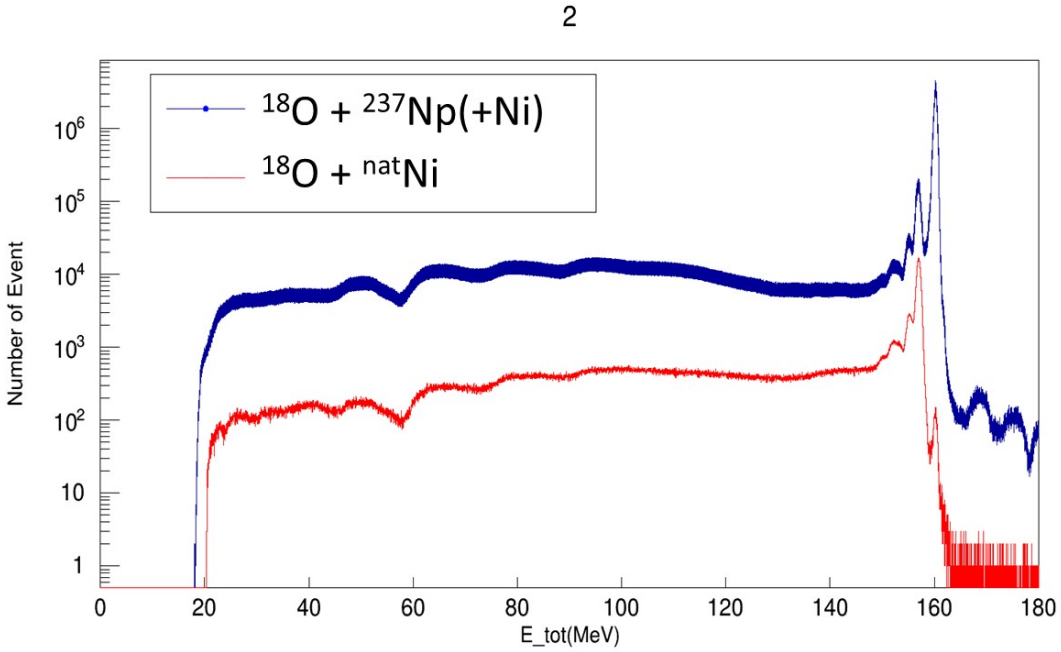

FIGURE 4.8: The total energy spectra provided by the ΔE-E telescope for both ^{18}O + ^{237}Np (blue) and ^{18}O + ^{nat}Ni (red). The elastic peaks are at ∼ 160 MeV.

fission detection efficiency.

The statistical uncertainty was calculated using the expression

$$\Delta N = \sqrt{N}, \tag{4.9}$$

where N is the number of events. In this work, the statistical uncertainty was also applied for the determination of the probability uncertainty according to Eq. (4.8), and we obtain the expression

$$\begin{aligned}\left(\frac{\Delta P_f(E^*)}{P_f}\right)^2 = &\left(\frac{\Delta N_{ej}^{coin}}{N_{ej}^{coin}}\right)^2 + \left(\frac{\Delta N_{ej}^{sing}}{N_{ej}^{sing}}\right)^2 + \left(\frac{\Delta\epsilon}{\epsilon(E^*)}\right)^2 \\ &- 2\frac{\mathrm{Cov}\left(N^{sing}(E^*); N^{coin}(E^*)\right)}{N^{sing}(E^*)N^{coin}(E^*)} \\ &- 2\frac{\mathrm{Cov}\left(N^{coin}(E^*); \epsilon(E^*)\right)}{N^{coin}(E^*)\epsilon(E^*)} \\ &+ 2\frac{\mathrm{Cov}\left(N^{sing}(E^*); \epsilon(E^*)\right)}{N^{sing}(E^*)\epsilon(E^*)}\end{aligned} \tag{4.10}$$

Since there is correlation between the number of event (N^{coin} or N^{sing}) and the efficiency ϵ, the last two covariance terms can be disregarded. But the covariance between single events and the coincident events has significantly impact on the final uncertainty. In this work for the simplification, we neglect this covariance term although over estimation of final uncertainty by 30% if it was not taken into account according to [41]. This is due to reason that it will not affect the conclusion of the method validation. We also can demonstrate that the efficiency can be considered as

constant with the excitation energy. As a consequence, the probability uncertainty is given

$$\Delta P_f(E^*) = P_f \sqrt{\left(\frac{\Delta N_{ej}^{coin}}{N_{ej}^{coin}}\right)^2 + \left(\frac{\Delta N_{ej}^{sing}}{(N_{ej}^{sing})^2}\right)^2} \tag{4.11}$$

4.5 Single, coincident and probability spectra

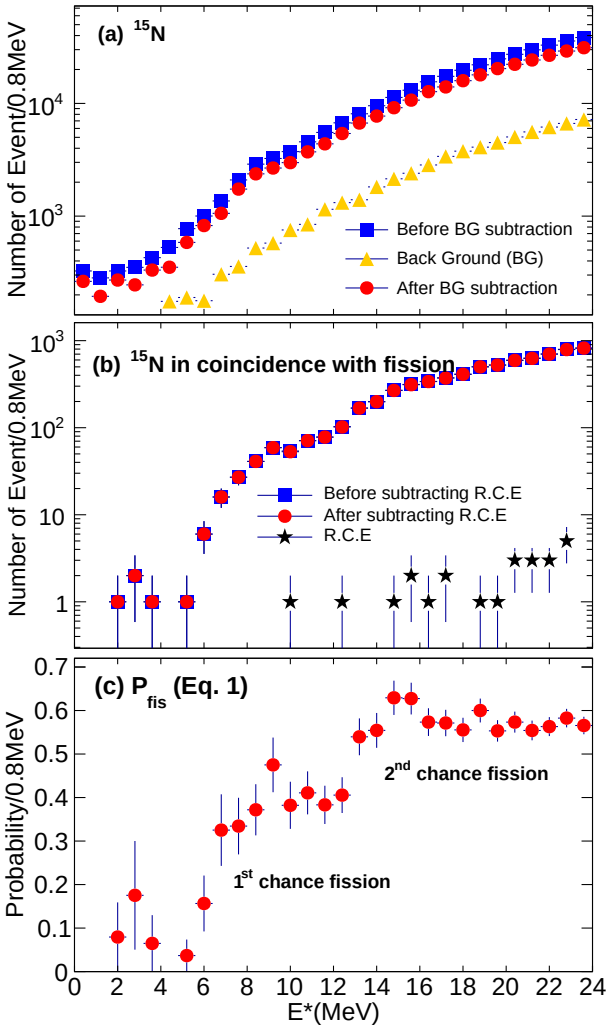

FIGURE 4.9: Data for the ^{237}Np(^{18}O,^{15}N)^{240}Pu reaction. (a) Singles spectra for ^{15}N as measured in the $\Delta E - E$ telescope, see main text for details. (b) Spectra for ^{15}N events from the $\Delta E - E$ telescope in coincidence with fission fragments detected by the MWPCs. R.C.E stands for random coincidence events. (c) Deduced fission-probability (P_f) spectrum. The increase in P_f at 6.50 MeV and at ∼14 MeV is due to the 1^{st} and 2^{nd} fission chances of ^{240}Pu, respectively.

Figure 4.9 demonstrates details of the analysis for the specific transfer channel ^{237}Np(^{18}O,^{15}N)^{240}Pu. Figure 4.9(a) shows a singles energy spectrum of the ^{15}N ejectiles recorded with the ^{237}Np(+^{nat}Ni) and dummy targets (blue rectangles and yellow triangles, respectively), which are taken from the corresponding data in Fig. 4.9(a) and (b). Difference between the two curves (red circles) is the net ejectile spectrum related

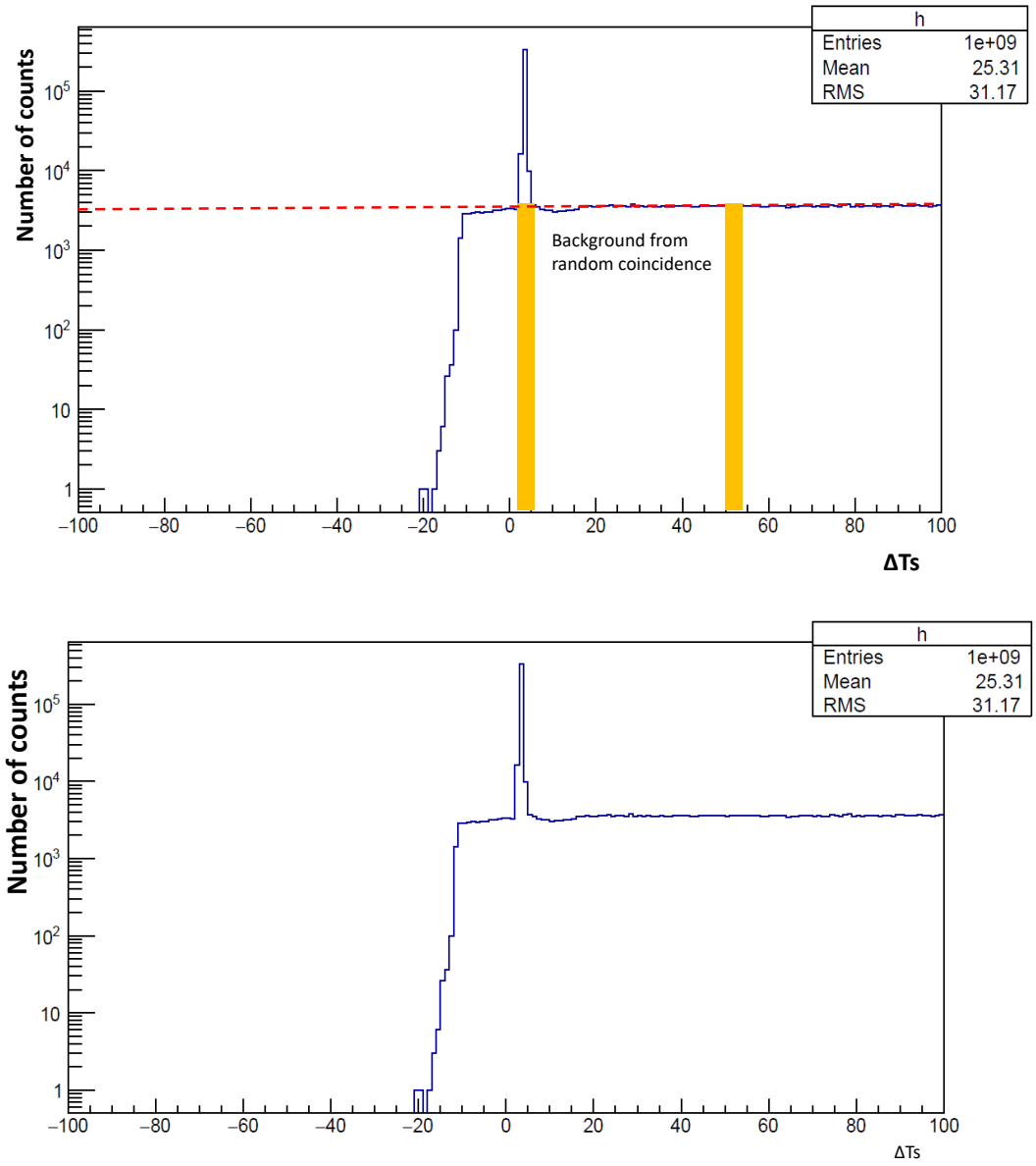

FIGURE 4.10: ΔTs is the average different time stamp (Ts) between Ts provided by a telescope ((Ts(E) + Ts(ΔE)) detector and a pair of MWPCs (Ts(MWPC1) + Ts(MWPC4)]) or (Ts(MWPC2) + Ts(MWPC3)]), can be written as: ΔTs = [(Ts(E) + Ts(ΔE) - Ts(MWPC1) + Ts(MWPC4)]/2 (top) and ΔTs = [(Ts(E) + Ts(ΔE) - Ts(MWPC2) + Ts(MWPC3)]/2 (bottom).

to the ^{237}Np target. This subtraction was done after normalization on the beam dose evaluated from the elastically-scattered peak of ^{18}O. Fig. 4.9(b) gives the ^{15}N data from Fig. 4.9(a), coincident with fission events in the MWPCs (blue rectangles). This part of the data can be affected by random coincidencies (black stars) with events from different origin, introduced in the ejectile-fragment coincidence gate (2 μs). To remove the random events, we plotted the number of counts (fission events) as a function of ΔTs which is defined as the average different time stamp (Ts) between Ts provided by a telescope ((Ts(E) + Ts(ΔE)) detector and a pair of MWPCs (Ts(MWPC1) + Ts(MWPC4)) or (Ts(MWPC1) + Ts(MWPC4)), can be written as: ΔTs = [(Ts(E) + Ts(ΔE) - Ts(MWPC1) + Ts(MWPC4)]/2 or ΔTs = [(Ts(E) + Ts(ΔE) - Ts(MWPC2) + Ts(MWPC3)]/2, see Fig. 4.10 (top) and (bottom), respectively. The flat area come from the random coincident origin. The random events containing in the green area under the peak with ΔTs between 2 and 6 or 400 ns and 1200 ns) were subtracted by the selected events covering the green area with ΔTs between 50 and 54 or 10000 ns and 10800 ns (black stars in Fig. 4.10(b)). It should be noted that random coincidences are very significant for the $^{16-18}$O ejectiles, particularly at the excitation energies of 0–5 MeV as indicated in Fig. 4.11. This is due to the influence of events from scattering (see the horizontal ^{18}O beam tail in Fig. 4.5), which are not entirely suppressed by the fragment-fragment-ejectile condition used in the data analysis. However, it can be seen in Fig. 4.9(b) that the impact of random coincidences on the remaining ejectile data is negligible. The red circles in Fig. 4.9(b) show the result after subtracting the random coincidence events from the coincidence spectrum.

By using Eq. (4.8) and the background subtracted data from Fig. 4.9(a) and (b), the $P_f(^{240}\text{Pu})$ distribution was obtained, as shown in Fig. 4.9(c).

The efficiency is mainly determined by the solid angle covered by the MWPCs, which is 7.5% after accounting for a 25% shadowing of the two forward-placed MWPCs by the $\Delta E - E$ telescope. Owing to the fact that the fission setup was able to detect both fission fragments, the efficiency correction was determined for each transfer channel according to the formula

$$\varepsilon = 7.5\% \times \frac{N_1}{N_2}, \tag{4.12}$$

where N_1 and N_2 stand for the number of ejectiles coincident with both fission fragments (triple coincidence) and with fragments detected by backward MWPC (double coincidence), respectively. The fission detection efficiencies were determined according to Eq. 4.12 for different excitation energy E^* ranges (5 MeV interval) and for different channels, as shown in Table 4.2. The dependence of ε on the transfer channel was found to be rather small: the average fission detection efficiencies, ε = 4.28(21)%, 4.82(24)%, 4.65(23)% for ^{237}Np(^{18}O, ^{16}O)^{239}Np, ^{237}Np(^{18}O, ^{16}N)^{239}Pu and ^{237}Np(^{18}O, ^{15}N)^{240}Pu, respectively. Similarly, only a weak dependence of ε on E^*, not exceeding 5%, was deduced, except for 0–5 MeV due to very statistics. The insensitivity of the efficiency to the excitation energy was also found in the comprehensive study [40].

Figure 4.12 presents fission probabilities (blue filled symbols) for the np, $2np$ and $2n$ transfer channels for the ^{237}Np(^{18}O,^{16}N)^{239}Pu, ^{237}Np(^{18}O,^{15}N)^{240}Pu and–^{18}O,^{16}O)–^{239}Np reactions, respectively. The three isotopes are of a great interest for the nuclear power cycle which explains the availability of a wealth of experimental data on their fission probabilities and barriers, thus making them suitable candidates for benchmarking the MNT method.

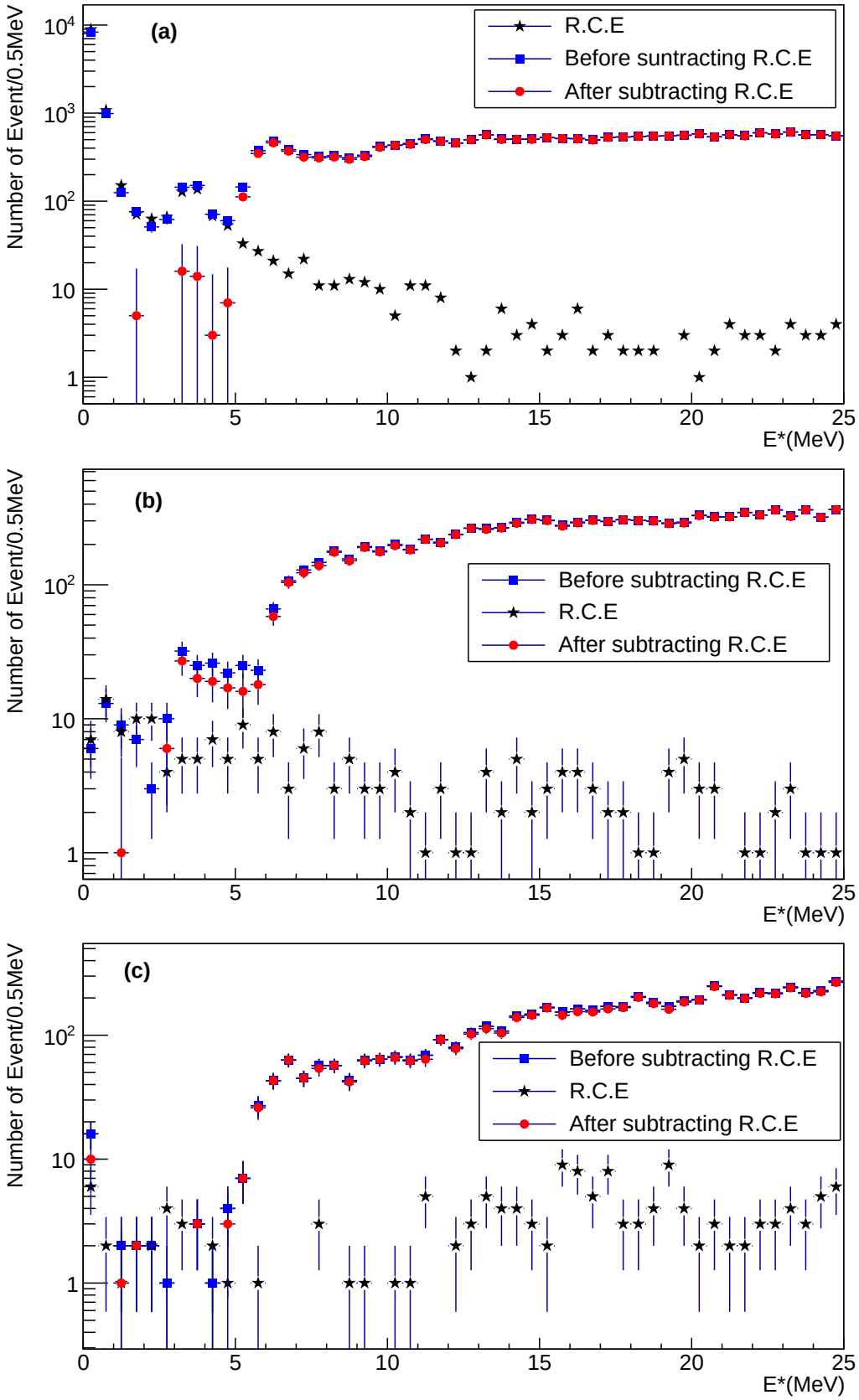

FIGURE 4.11: The coincident spectra are shown for ^{237}Np(^{18}O, ^{18}O)^{237}Np, ^{237}Np(^{18}O, ^{17}O)^{238}Np and ^{237}Np(^{18}O, ^{16}O)^{239}Np channels, respectively. The random coincidences are observed to be important for these channels.

TABLE 4.2: The fission detection efficiencies were determined according to Eq. 4.12 for different excitation energy E^* ranges (5 MeV interval) and for different channels.

E^* (0–5 MeV)	Channels	N_1	N_2	ε (%)
	^{17}O(^{18}O, ^{17}O)^{238}Np	136	485	2.80
	^{16}O(^{18}O, ^{16}O)^{239}Np	27	198	1.36
	^{16}N(^{18}O, ^{16}N)^{239}Pu	27	198	1.36
	^{15}N(^{18}O, ^{15}O)^{240}Pu	27	198	1.36
E^* (5–10 MeV)	Channels	N_1	N_2	ε (%)
	^{17}O(^{18}O, ^{17}O)^{238}Np	1135	2055	5.52
	^{16}O(^{18}O, ^{16}O)^{239}Np	455	823	5.53
	^{16}N(^{18}O, ^{16}N)^{239}Pu	613	1015	6.04
	^{15}N(^{18}O, ^{15}O)^{240}Pu	169	294	5.75
E^* (10–15 MeV)	Channels	N_1	N_2	ε (%)
	^{17}O(^{18}O, ^{17}O)^{238}Np	2247	3784	5.94
	^{16}O(^{18}O, ^{16}O)^{239}Np	929	1656	5.61
	^{16}N(^{18}O, ^{16}N)^{239}Pu	1440	2349	6.13
	^{15}N(^{18}O, ^{15}O)^{240}Pu	860	1430	6.01
E^* (15–20 MeV)	Channels	N_1	N_2	ε (%)
	^{17}O(^{18}O, ^{17}O)^{238}Np	2694	4446	6.06
	^{16}O(^{18}O, ^{16}O)^{239}Np	1584	2759	5.74
	^{16}N(^{18}O, ^{16}N)^{239}Pu	2580	4143	6.23
	^{15}N(^{18}O, ^{15}O)^{240}Pu	2528	4199	6.02

4.6 Fitting Method

The selected bin of 0.8 MeV for the plots in Fig. 4.9 result in just a few data points in the rising – and most important – part of the fission probability (P_f) curves. This rather poor energy resolution excludes observation of any resonance (class-II or well (II)) sub-barrier structures, which are sensitive to both the inner and outer barrier heights [12]. On the other hand, it is well known [22] that the use of a single-humped, Hill-Wheeler-type approximation, allows a consistent derivation of the height of the barrier to be made corresponding to the higher one as determined by the models involving the two-humped fission barrier description.

Consequently, in the present work, the fission barrier heights were deduced from P_f from Fig. 4.12, fitted with the Hill-Wheeler's expression (Eq. 2.18) for the barrier penetration. The fitting was performed using CERN ROOT code (Chi-square method), over the range of the sub-barrier and first-chance fission. The fitted curves are illustrated in Fig. 4.12 in green, whereas the deduced B_f are compared to literature values in Table 5.1. The obtained curvatures are in the range of 1-5 MeV, which in general largely different from 1 MeV known from the literature. However, the fission-barier curvature cannot be deduced in a correct way with this approach (simply inverted parabola), which replaces the complex (in general, two-humped) barrier structure in actinides with a simple inverted parabola. Therefore, in the following, only (P_f) and (B_f) will be considered.

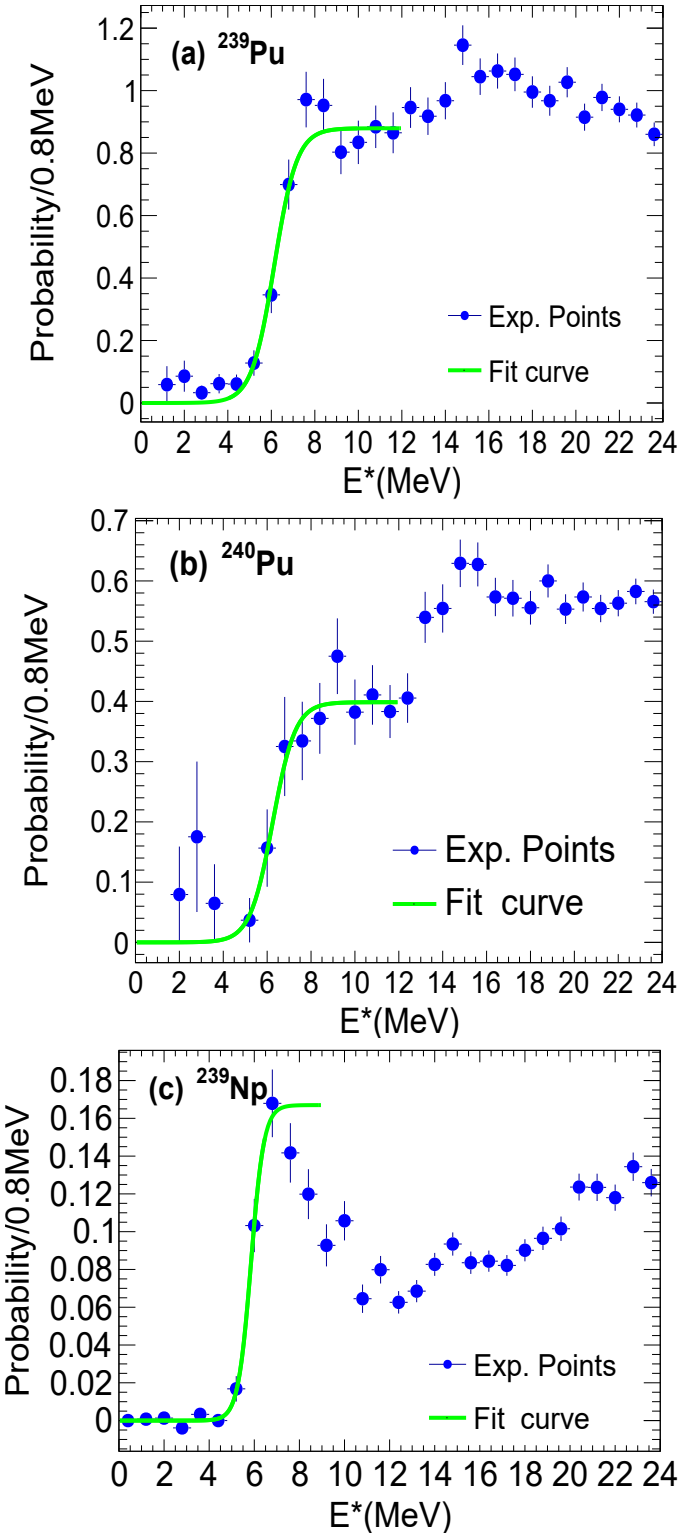

FIGURE 4.12: Fission probability as a function of excitation energy for ^{239}Pu (a), ^{240}Pu (b) and ^{239}Np (c). Green solid line on each plot shows the fit function from Eq. 4.12 applied to the sub-barrier and first-chance fission parts of the data only.

Chapter 5

Experimental Results and Discussion

5.1 Fission Barrier Heights and discussions

The fission barrier heights of the three nuclei ^{239}Np and ^{239,240}Pu were determined to be $B_f(^{239}\text{Np})$ = 5.86 $\pm$ 0.09 MeV, $B_f(^{239}\text{Pu})$ = 6.14 $\pm$ 0.12 MeV and $B_f(^{240}\text{Pu})$ = 6.25 $\pm$ 0.32 MeV. Table 5.1 compares the obtained B_f values with the RIPL3 library [18] (evaluation from the neutron-induced cross-sectons), as well as with known data from several transfer reactions using light projectiles, such as ^{238}Pu(t,p)^{240}Pu [6] and ^{238}U(^{3}He,d)^{239}Np [7]. We note that the cited literature data [6, 7, 18] provide information on the first (inner) and the second (outer) barrier height (cf. Table 5.1).

It follows from the Table that our B_f values agree well with the maximal of the two barrier heights, i.e. with the inner barrier height, for the studied nuclei. In particular, this agreement remains within one-sigma interval with the transfer-reaction results, carried out for actinide nuclei using transfer reactions [28, 6]. By using a statistical model including the double-humped fission barrier concept to describe the fission decay, peaks and curvatures for two barriers were determined for some cases, but only information for one of the barriers are given for all other cases. As for the empirical data from RIPL3 [18], their inner barrrier heights are reproduced by our results with a high precision: within 1% for ^{239}Pu and 4% for ^{240}Pu.

5.2 Fission Probabilities and discussions

Fission probabilities from Fig. 4.12 are of importance, from the point of view of reaction rate calculations for given conditions (reactor or stellar neutron spectra, for instance). In this respect, it is wort noting that transfer reactions are the only tool to access the low-energy part of the P_f spectrum (i.e., below the neutron-separation energy S_n) in nuclei with an even number of neutrons (i.e., for which $B_f \leqslant S_n$).

For the maximal values of the P_f of the compound nuclei in Fig. 4.12, we observe some discrepancies between our results and the literature data obtained using lighter ion beams [6, 7, 27, 20]. In particular, for ^{240}Pu formed in the ^{236}U(^{12}C,^{8}Be) reaction [20] one obtains P_{max} = 0.6 at E^* = 8 MeV, whereas our experient delivers a somewhat lower value of P_{max} = 0.4, at the same excitation energy. This discrepacy increases for ^{239}Np studied in the ^{239}U(^{3}He,t)^{239}Np reaction [27], where P_{max} = 0.7 at E^* = 6 MeV is significantly larger than the present result of P_{max} = 0.17 (E^* = 7 MeV). Finally, the ^{238}Pu(d,p)^{239}Pu reaction delivers P_{max} = 0.5 at E^* = 7 MeV [7] for ^{239}Pu, in contrast to our value of P_{max} = 0.9.

Concerning the latter case, it is well established [23] that results from a (d,p) reaction should be corrected for the deutron breakup, which creates protons as ejectiles

TABLE 5.1: Fission barrier heights B_f for ^{239}Np and ^{239,240}Pu isotopes from this work, in comparison to the literature data.

Isotope	Reference	B_f(MeV)(inner, outer)
^{239}Np	This work: (^{237}Np(^{18}O,^{16}O)^{239}Np)	5.86 ± 0.09
	RIPL3 [18]	—
	^{238}U(^{3}He,d)^{239}Np [7]	$5.85 \pm 0.30, 5.50 \pm 0.30$
^{239}Pu	This work: (^{237}Np(^{18}O,^{16}N)^{239}Pu)	6.14 ± 0.12
	RIPL3 [18]	6.20, 5.70
^{240}Pu	This work: (^{237}Np(^{18}O,^{15}N)^{240}Pu)	6.25 ± 0.32
	RIPL3 [18]	6.05 , 5.15
	^{238}Pu(t,p)^{240}Pu [6]	$5.80 \pm 0.20, 5.45 \pm 0.20$

and leads to an overestimation of the event number in the singles spectrum and, consequently, to an underestimation of the fission probabilities.

Our lower P_f values for ^{239}Np and ^{240}Pu nuclei can be explained by the difference in the geometry between the present and the mentioned experiments (the ejectile detector angle relative to the beam axis), which makes the final results sensitive to the induced angular momentum effect, which alters level densities that affect fission probability sensitively.

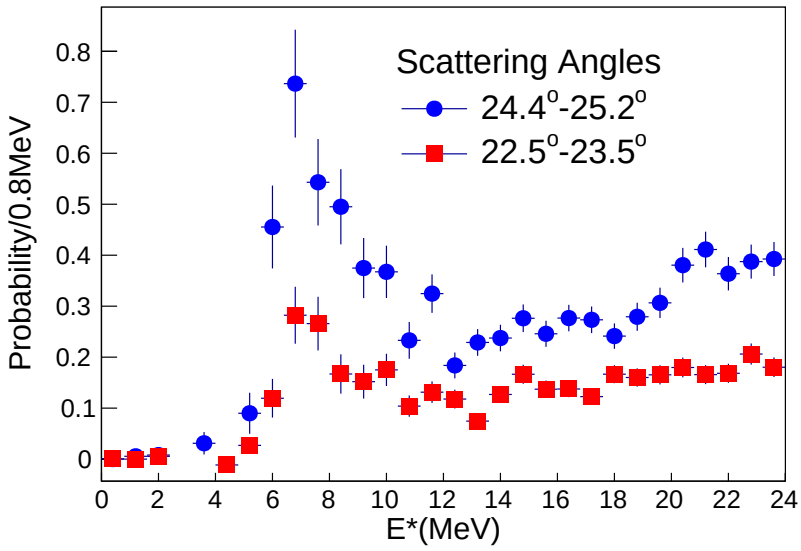

FIGURE 5.1: The fission probability of ^{239}Np as a function of the excitation energies for two different scattering angle ranges of the ejectile ^{16}O.

The above conjecture is strongly supported by our experimental data. In particular, one observes that the magnitude of the fission probability is sensitive to the angle of the registered ejectile, given by the ring of the $\Delta E - E$ telescope, with respect to the beam direction. For example, in the ^{237}Np(^{18}O,^{16}O)^{239}Np reaction, the P_{max} value can

TABLE 5.2: The inner fission barrier heights B_f for ^{239}Np and ^{239,240}Pu isotopes from this work compared with the theoretical calculation using the constrained Hartree-Fock + BCS model with Skyrme interactions (SkM* and SLy4).

Isotope	This work	SLy4	SkM*
^{239}Np	5.87 ± 0.09	10.3	8.50
^{239}Pu	6.14 ± 0.12	10.1	8.25
^{240}Pu	6.25 ± 0.32	10.6	8.76

be changed by a factor of two, as indicated in Fig. 5.1. For the effects of the angular momentum transfer on the fission barrier height, due to the poor statistics, any definitive conclusion could not be drawn with high degree of confidence, thus leaving the question open to further investigations.

The P_f dependence on the ejectile angle was also observed in the ^{238}U(d,p) reaction, though the effect was found to be smaller [23]. The magnitude of the effect is expected to be linked to the projectile mass (^{18}O in the present study and ^{3}He in [23]); this topic makes a subject for dedicated further study.

Our fission barrier data have also been compared with the theoretical prediction using the constrained Hartree-Fock + BCS model with Skyrme interactions (SkM* and SLy4), as shown in Tab. 5.2. The model with SkM* and SLy4 overestimate the inner fission barrier heights. Although the reasons are well understood from the fact that by the exclusion of axial asymmetry, the fission barrier heights are overestimated by 0.25–2 MeV, we have motivation to find out other essential factors which contribute to better reproduce the fission barrier height. We investigate the many-body force term of the Skyrme force.

Chapter 6

Many-body force effects on fission barrier height

Although there are many applicable theories accounting essentially for the nucleus degrees of freedom, microscopic quantum calculations taking into account the nucleon degrees of freedom is desired for the highly-reliable theoretical nuclear data. Indeed, the shell effect, which can be correctly introduced within microscopic quantum calculations, is known to play an important role in the occurrence of fission [69]. On the other hand, the fission barrier height, which is indispensable for completing the theoretical nuclear database (for example, see [49, 48, 9, 17]), is a decisive factor for the occurrence of fission. In this work, based on a microscopic axial symmetry Z, ρ constraint Hartree-Fock+BCS calculations, the fission barrier height is systematically studied focusing on the many-body force effect. Here, in terms of explaining the binding property of neutron-rich light nuclei (e.g., the binding energy of ^{24}O and so on), the three-body force attracts a special attention in the nuclear physics community[29] .

6.1 Hartree-Fock theory

6.1.1 Skyrme interaction

The Skyrme interaction can be expressed as a potential in its original form [72],

$$V = \sum_{i<j} v_{ij}^2 + \sum_{i<j<k} v_{ijk}^3, \tag{6.1}$$

where v_{ij}^2 and v_{ijk}^3 are the two- and three-body term, respectively. For the simplification of the calculations, the short-range expansion (with δ function) was employed for both two- and three-body interaction. The two-body term can be written in the configuration space with the relative wave vector $\vec{k}$ and $\vec{k}$ of two nucleons as

$$\begin{aligned} v_{12} &= t_0(1 + x_0 P_\sigma)\delta(\vec{r_1} - \vec{r_2}) && (6.2)\\ &+ \frac{1}{2} t_1(1 + x_1 P_\sigma)[\delta(\vec{r_1} - \vec{r_2})k^2 + k'^2\delta(\vec{r_1} - \vec{r_2})] && (6.3)\\ &+ t_2(1 + x_2 P_\sigma)\vec{k}'\delta(\vec{r_1} - \vec{r_2})\vec{k} + iW_0(\vec{\sigma_1} + \vec{\sigma_2}).\vec{k}' \times \delta(\vec{r_1} - \vec{r_2})\vec{k}. && (6.4) \end{aligned}$$

Here t_0, t_1, t_2 and x_0, x_1, x_2 are the parameters. v_{12} depends on the relative distance $\vec{r_1} - \vec{r_2}$ between two nucleons. The spin-exchange operator and the Pauli spin matrices are denoted by P_σ and $\vec{\sigma}$, respectively. The short-range limit W_0 of the two-body spin-orbit force can be written,

$$W_0 = -\frac{2}{3}\pi \int_0^{+\infty} V_{LS}(r) r^4 dr. \tag{6.5}$$

Now $\vec{k}$ is the operator $(\vec{\nabla}_1 - \vec{\nabla}_2)/2i$ acting on the right; while, $\vec{k}'$ denotes the operator -$(\vec{\nabla}_1 - \vec{\nabla}_2)/2i$ acting on the left.

The Syrme three-body force term has a form with a zero-range force

$$v^3_{123} = t_3(1 + x_3 P_\sigma)\delta(\vec{r_1} - \vec{r_2})\delta(\vec{r_2} - \vec{r_3}). \tag{6.6}$$

Here t_3 and x_3 are also parameters. This term gives a simple phenomenological description of many-body effects (medium effects) representing the interaction between two nucleons in the influence of other nucleons. Skyrme interaction can be described as a type of phenomenological G matrix which is already corrected with the effect of short-range.

6.1.2 Hartree-Fock (HF) equation

For the Skyrme force, the HF equation can be derived relatively simple, and will be shown now. The wave functions of nucleon at their ground states are represented by an product of single wave functions $\phi_i(x_j)$ in a Slater determinant form:

$$\Phi_{HF} = \frac{1}{\sqrt{N!}} det|\phi_i(x_j)|_{i,j=1,2,3,....N}. \tag{6.7}$$

Here x represents the set ($\vec{r}, \sigma$ and q) which are space, spin, and isospin coordinates ($q = +\frac{1}{2}$ for a proton, $q = -\frac{1}{2}$ for a neutron).

The Hamiltonian operator is:

$$\hat{H} = \hat{T} + \hat{V} \tag{6.8}$$

The HF energy or the expectation value of the total energy is obtained

$$E_{HF} = \left\langle \Phi_{HF} | \hat{H} | \Phi_{HF} \right\rangle \tag{6.9}$$

$$= \sum_i \left\langle i \left| \frac{p^2}{2m} \right| i \right\rangle + \frac{1}{2} \sum_{ij} \langle ij \left| \tilde{v}_{12} \right| ij \rangle + \frac{1}{6} \sum_{ijk} \langle ijk \left| \tilde{v}_{123} \right| ijk \rangle \tag{6.10}$$

$$= \int H(\vec{r}) d^3 r, \tag{6.11}$$

where $\tilde{v}$ indicates an antisymmetrized matrix element. We used the Skyrme energy functional, thus the most general form of the Hamiltonian density $H(\vec{r})$ [42] is expressed:

$$H(\vec{r}) = \varepsilon_{\text{kin}} + \varepsilon_{\text{Skyrme}} + \varepsilon_{\text{Coulomb}} + \varepsilon_{\text{pair}} + \varepsilon_{\text{cm}}, \tag{6.12}$$

The total kinetic energy density functional for proton and neutron by accounting for the slight difference between the proton and the neutron mass ($\frac{\hbar^2}{2m_p} = 20.749821$, $\frac{\hbar^2}{2m_n} = 20.721260$) which becomes important for exotic and heavy nuclei.

$$\varepsilon_{\text{kin}} = \frac{\hbar^2}{2m_p}\tau_n + \frac{\hbar^2}{2m_p}\tau_p, \tag{6.13}$$

$$\begin{aligned}\varepsilon_{\text{Skyrme}} =& \frac{1}{2}B_0\rho^2 + \frac{1}{2}B_3\rho^{\alpha+2} - \frac{1}{2}(B_0' + B_3'\rho^{\alpha})\tilde{\rho}^2 + B_1(\rho\tau - \boldsymbol{j}^2) \\ &+ B_1'(\tilde{\rho}\tilde{\tau} - \tilde{\boldsymbol{j}}^2) + \frac{1}{2}B_2\rho\Delta\rho + \frac{1}{2}B_2'\tilde{\rho}\Delta\tilde{\rho} - \frac{1}{2}B_4[\rho\nabla.\boldsymbol{J} + \boldsymbol{\sigma}.(\nabla\times\boldsymbol{j})] \\ &- \frac{1}{2}(B_4 + b_4')[\tilde{\rho}\nabla.\tilde{\boldsymbol{J}} + \tilde{\boldsymbol{\sigma}}.(\nabla\times\tilde{\boldsymbol{j}})] + \frac{1}{2}C_1(\boldsymbol{J} - \boldsymbol{\sigma}.\boldsymbol{\tau}) + \frac{1}{2}C_1'(\tilde{\boldsymbol{J}} - \tilde{\boldsymbol{\sigma}}.\tilde{\boldsymbol{\tau}}),\end{aligned} \tag{6.14}$$

$$\varepsilon_{\text{Coulomb}} = \frac{1}{2}\frac{e^2\rho_p(\boldsymbol{r})\rho_p'(\boldsymbol{r})}{|\boldsymbol{r}-\boldsymbol{r'}|} - \frac{3}{4}e^2\left(\frac{3}{\pi}\right)^{1/3}[\rho_p]^{4/3}, \tag{6.15}$$

$$\varepsilon_{\text{cm}} = -\frac{1}{2mA}\left\langle(\hat{P}_c m)^2\right\rangle, \hat{P}_c m) = \sum_i \hat{P}_i. \tag{6.16}$$

$\varepsilon_{\text{pair}}$ is correspond to the pairing energy E^{DD}_{pair} in Sec. 6.1.3. Here, the functionals are written in terms of a few local densities and currents: local density ρ, kinetic energy density τ, spin-orbit density $\boldsymbol{J}$, current $\boldsymbol{j}$, spin density $\boldsymbol{\sigma}$, kinetic spin density $\boldsymbol{\tau}$, and pair current ξ.

$$\rho_q(r) = \sum_{i=1}^{N}|\phi_i(\vec{r},\sigma,q)|^2, \tag{6.17}$$

$$\tau_q(r) = \sum_{i=1}^{N}|\nabla\phi_i(\vec{r},\sigma,q)|^2 \tag{6.18}$$

$$\boldsymbol{J}_q(r) = (-i)\sum_i[\phi_i^*(\vec{r},\sigma,q)\nabla\phi_i(\vec{r},\sigma,q)\times\sigma], \tag{6.19}$$

$$\boldsymbol{j}_q(r) = -\frac{i}{2}\sum_i[\phi_i^*(\vec{r},\sigma,q)\nabla\phi_i(\vec{r},\sigma,q) - c.c], \tag{6.20}$$

$$\boldsymbol{\sigma}(r) = \sum_i[\phi_i^*(\vec{r},\sigma,q)\sigma\phi_i(\vec{r},\sigma,q)], \tag{6.21}$$

$$\boldsymbol{\tau}(r) = \sum_i\sum_j[\nabla_i\phi_j^*(\vec{r},\sigma,q)\hat{\sigma}\nabla_i\phi_j(\vec{r},\sigma,q)], \tag{6.22}$$

$$\xi_q(r) = 2\sum_{i=1}|\phi_i|^2(\vec{r},\sigma,q), \tag{6.23}$$

The index q denotes for either protons or neutrons. It is also useful to define the isoscalar density $\rho = \rho_p + \rho_p$ and the isovector density $\tilde{\rho} = \rho_p - \rho_p$.

The parameter B_i and B_i' are useful for the functional form, and they are associated with the widely employed standard Skyrme parameters t_i and x_i via

$$\begin{aligned}B_0 &= \frac{3}{4}t_0, \\ B_0' &= \frac{1}{2}t_0(\frac{1}{2} + x_0), \\ B_1 &= \frac{3}{16}t_1 + \frac{5}{16}t_2 + \frac{1}{4}t_2x_2,\end{aligned}$$

$$
\begin{aligned}
B_1' &= \frac{1}{8}[t_1(\frac{1}{2}+x_1) - t_2(\frac{1}{2}+x_2)], \\
B_2 &= \frac{9}{32}t_1 - \frac{5}{32}t_2 - \frac{1}{8}t_2x_2, \\
B_2' &= \frac{1}{16}[3t_1(\frac{1}{2}+x_1) + t_2(\frac{1}{2}+x_2)], \\
B_3 &= \frac{1}{8}t_3, \\
B_3' &= \frac{1}{12}t_3(\frac{1}{2}+x_3), \\
B_4 &= \frac{1}{2}t_4 - \frac{1}{2}b_4', \\
C_1 &= \eta_{tls}\frac{1}{8}[t_1(\frac{1}{2}-x_1) - t_2(\frac{1}{2}+x_2)] \\
C_1' &= -\eta_{tls}\frac{1}{16}(t_1-t_2).
\end{aligned}
$$

The parameter b_4' turns the isovector dependency of the spin-orbit interaction. For a zero-range tow-body interaction, $b_4' = t_4/2$. The parameter η_{tls} is inserted as a switch factor: $\eta_{tls} = 1$ for including the full tensor spin-orbit, whereas, $\eta_{tls} = 0$ is usually employed to neglect the tensor spin-orbit term.

6.1.3 BCS theory

Pairing interaction is an important ingredient of quantum many-body systems. This interaction combines two fermions into one boson, so that condensation can take place as a new feature. For example the superconductivity follows from the pairing interaction.

There have been proposed two methods of introducing the pairing interaction in many-nucleon systems; one is the HFB (Hartree-Fock-Bogoliubov) approach, and the other is the BCS (Bardeen, Cooper, and Schrieffer) approach. In this research, the BCS type pairing is calculated using the code SkyAX. In order to include the pairing effect, the following energy density should be added to the standard Skyrme energy density functional.

$$E_{\text{pair}} = \sum_q \frac{v_q}{4} \int dr^3 \xi_q(r)^2$$

where v_q is the strength parameter, $\xi_q(r)$ denotes the paring density with the phase-space weight w_a, occupation amplitude u_a and non-occupation v_a ($u_a = \sqrt{1-v_a^2}$). More precisely, we introduce the density-dependent pairing

$$E_{\text{pair}}^{DD} = \sum_q \frac{v_q}{4} \int dr^3 \left[\left\{ 1 - \frac{\rho(r)}{\rho_0}^{\gamma} \right\} \xi_q(r)^2 \right]$$

where ρ_0 is the nuclear saturation density, typically $\rho_0 = 0.16\, fm^3$. The surface profile of the pairing is controlled by the corresponding parameter γ, whose standard value is equal to 1. For the detail of the pairing used in the density functional, see a review article [64].

6.1.4 Deformation energies

To obtain a solution with a given deformation, one has to add in eq.(6.12) an external field (constraint); otherwise one finds automatically a solution for which the energy is locally a minimum (ground state or eventually, an isomeric state). The shape of a nucleus may be characterized by the multipole moments of the density:

$$Q_{\lambda\mu} = tr[\,\rho q_{\lambda\mu}]; (tr \equiv trace) \tag{6.24}$$

here $q_{\lambda\mu}$ is the matrix element $\langle\alpha|\hat{q}_{\lambda\mu}|\beta\rangle$ of the multipole operator $\hat{q}_{\lambda\mu}$

$$\hat{q}_{\lambda\mu} = r^{\lambda}\, Y_{\lambda\mu}(\theta, \varphi); \tag{6.25}$$

Let us choose for instance the quadrupole moment $Q_{20} = Q_2$. If HF equation

$$[\hat{T} + V_{HF} - \lambda\hat{q_2}]\phi_i = \epsilon_i\phi_i \tag{6.26}$$

is solved, one obtains a solution with a quadrupole moment Q_2. The Lagrange multiplier λ gives then the local derivative of the deformation energy at the point Q_2 (i.e. the negative driving force, which wants to bring the nucleus back to the minimum):

$$\lambda = \frac{dE(Q_2)}{d(Q_2)} \tag{6.27}$$

In this way, one can, however, only obtain those regions of the curve $E_{HF}(Q2)$ which have a positive curvature. To obtain the full curves, one can use a quadratic constraint.

Note: The Skyrme force has ten adjustable parameters; for the pairing effects (in BCS approximation [71]) one more parameter is used. Thus, a total of eleven free parameters are used in all calculations.

6.2 Nuclear medium effect

6.2.1 Density functional theory

Among several microscopic treatments of many nucleon systems we employ nuclear density functional theory.

Within the zero-range type Skyrme interaction formalism, the Hamiltonian density of nuclear energy density functional [72] is described as follows:

$$H = \frac{3}{8}t_0\rho^2 + \frac{1}{16}t_3\rho^{2+\alpha} + \cdots \tag{6.28}$$

where t_0-term mainly includes the two-body force effect, and $t_3\rho^{2+\alpha}$ is called the density dependent term (for the mathematical procedure leading to the Hamiltonian, see Ref. [36]). According to Ref. [35] , t_0-term is claimed to be the most dominant term in the nuclear energy density functional, and t_3-term is the second dominant terms; indeed, no bound states exist for ^{4}He and ^{8}He if there is not for t_0-term, and the binding energies of ^{4}He and ^{8}He are drastically changed by the t_3-term. We focus on t_0 and t_3 terms of the energy density functional shown in Eq. (6.28). It is true that the density-dependent term in the energy density functional approximately represents the effect of the three-body force and of various in-medium effects. However it is worth noting before starting the main discussion that such effects cannot be rigorously included

within Hartree-Fock or Hartree-Fock-Bogoliubov approach (for the connection between zero-range three body force and the density-dependent term, see [72] and [9] for additional references). For a recent review explaining the nuclear energy density functional and the Skyrme parameter set within the usage of heavy-ion collisions, for example, see [63].

If t_3-term purely includes the three-body force effect, α should be equal to 1. On the other hand, the force parameter α is not generally an integer, due mainly to the nuclear medium effects as seen in the latter section. As a typical value, $\alpha = 1/6$ is employed for SLy4 [19] and SkM* [8] interactions.

6.2.2 Many-body force

Using a mathematical expansion, we try to find an appearance of nuclear medium effect as represented by $\rho^{2+\alpha}$ with $0 < \alpha \leq 1$ in the surface tension contributions. Nuclear medium effect includes the three-body, four-body forces and so on. Let us start with the two-body force (Panel (a) of Figure. 6.1). At the level of the Hamiltonian density (to be integrated with respect to the spatial directions), the potential part due to the two-body force ($F = -\nabla V$) is represented analogously to the classical electromagnetic force

$$V_{\text{2body}} = \frac{k}{2!}\sum_{i\neq j}\frac{\rho_i\rho_j}{|r_i - r_j|} \sim \frac{k}{2r}\rho_i^2 = k_2\rho^2$$

at the zero range approximation limit ($\rho_j \to \rho_i$), where k denotes the coupling constant, and $|r_i - r_j|$ is replaced with the specific length r. The multiplication $1/2!$ appears by accounting for the double counting. Although k_2 depends on r, it is abbreviated in the notation. This simply shows the appearance of $\rho^2 = |\psi|^4$ term in the energy density functional (cf. the $|\varphi|^4$-theory of the Lagrangian formalism of the scaler field theory).

In the same manner, the potential part of the Hamiltonian density due to the three-body force can be reduced to that proportional to ρ^3 (Panel (b) of Figure 6.1).

$$V_{\text{3body}} = \frac{k'}{3!}\sum_{i\neq j\neq h}\frac{\rho_i\,\rho_j\,\rho_h}{(|r_i - r_j|\;|r_j - r_h|\;|r_i - r_h|)^{1/3}} \sim k_3\rho^3,$$

where the coupling constant k' is usually different from k. Since there is no three-body force in electronic systems, here V_{3body} is assumed to be applied to nucleon systems. Although the two-body force depends only on the positions/configurations of the two particles, the three-body force can be different by the positions/configurations of the three particles. The specific length of three-body force should be different from that of two-body force. We assume that the representation for the n-body force can be introduced similarly. Note that what we have shown here is only done by a mathematical expansion (for a rigorous quantum treatment, refer to many-body perturbation theory [29]).

The previous discussion on many-body force effect is the volumetric energy contribution, because only the volumetric density has been considered. Since nuclei are finite-body systems with their surfaces, the surface energy contribution might play a non-negligible role in determining the fission dynamics. According to the concept of the leptodermous expansion (for example, see [68, 58]), the nuclear medium effect is regarded as certain surface energy contributions. For the volumetric contribution

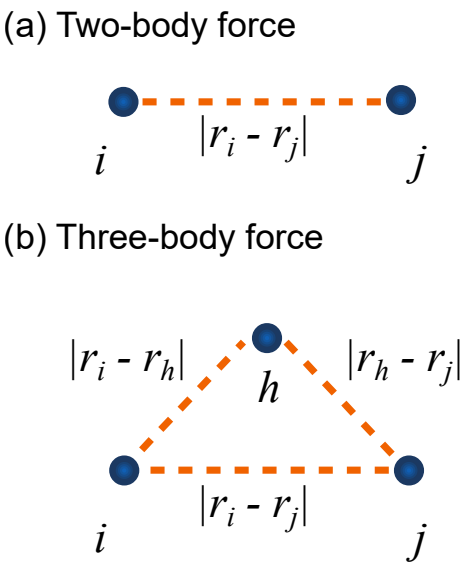

FIGURE 6.1: Illustration of the nuclear medium effect as nuclear many-body force effects. Interactions are shown in the dashed lines. Two-body force acts between the particles i and j, and three-body force acts between particles i, j, and h. The three-body force effect is included in the parameter α of the nuclear energy density functional.

described by $V = k_2\rho^2 + k_3\rho^3 + \cdots$, the surface contribution V_S becomes

$$\begin{aligned} V_S &= (k_2\rho^2 + k_3\rho^3 + \cdots)^{2/3} \\ &= k_2^{2/3}\rho^{4/3}(1 + (k_3/k_2)\rho + \cdots)^{2/3} \\ &\sim k_2^{2/3}\rho^{4/3} + \tfrac{2}{3}k_3k_2^{-1/3}\rho^{7/3}. \end{aligned}$$

By representing V_S by V expanded by ρ^2, the fractional powers $4/3, 7/3, 10/3, \cdots$ are obtained. If we restrict ourselves to the power larger than 2, the fractional power $7/3$ appears at first.

Let us limit ourselves to the power between 2 and 3. By representing V_S by V expanded by ρ or ψ, the fractional density dependence with $8/3$ appears in the former case, while that with $7/3$ and $17/6$ appear in the latter case. In this paper those terms associated with more than two-body forces is referred to many-body force term. This simple calculi show that many-body forces tend to manifest in the surface contribution. If we choose one value for the power (e.g., $7/3$), it approximately includes the mixture of many-body force effects of several kinds. More precisely, a given power of the density in the Hamiltonian density represent either the effect of a genuine three-body force or the many-body correlations induced by a two-body force.

6.3 Method

6.3.1 Constrained Hartree-Fock+BCS theory

For carrying out the density fuctional calculations, the constrained Hartree-Fock+BCS theory (CHF) is utilized to impose a constraint on the quadrupole-deformation. The

TABLE 6.1: Skyrme parameter sets (10 parameters profiling the effective nuclear force). The proposed interactions (mSLy4 and mSkM*) are compared to the original interactions (SLy4 and SkM*), where the difference can be found in the values of t_3 and α.

	SLy4	SkM*	mSLy4	mSkM*
t_0 (MeV·fm^3)	−2488.913	−2645.000	−2488.913	−2645.000
t_1 (MeV·fm^5)	486.818	410.000	486.818	410.000
t_2 (MeV·fm^5)	−546.395	−135.000	−546.395	−135.000
t_3 (MeV·fm$^{3(1+\alpha)}$)	13777.000	15595.000	14645.710	16004.450
x_0	0.834	0.090	0.834	0.090
x_1	−0.344	0.000	−0.344	0.000
x_2	−1.000	0.000	−1.000	0.000
x_3	1.354	0.000	1.354	0.000
W_0 (MeV·fm^5)	123.000	130.000	123.000	130.000
α	0.166667	0.166667	0.195967	0.179000

TABLE 6.2: Binding energy [MeV] for selected reference nuclei. The calculated values using original interactions (SLy4 and SkM*) and the proposed interactions (mSLy4 and mSkM*) are shown.

	Experiment (NuDat2 [1])	SLy4	SkM*	mSLy4	mSkM*
^{208}Pb	1636.96	1636.96	1632.80	1634.88	1622.40
^{120}Sn	1020.00	1020.00	1017.60	1022.40	1014.00
^{90}Zr	783.90	785.70	763.20	792.00	760.50
^{40}Ca	342.00	346.40	345.20	352.40	346.80
^{16}O	127.63	129.60	130.24	133.92	132.00

master equation is obtained by the variational principle:

$$\delta \langle \psi | \hat{H} - \beta_2 \hat{Q} | \psi \rangle = 0,$$

where $\hat{H}$ means the Hamiltonian of many nucleon systems, the quadrupole parameter β_2 plays a role of the Lagrangian multiplier for the quadrupole constraint $\beta_2 \hat{Q}$, and the trial function ψ is taken as the Slater determinant. The BCS-type pairing interaction is included in $\hat{H}$ together with the nuclear and the Coulomb interactions. For the pairing interaction only neutron-neutron pairs and proton-proton pairs are taken into account in these calculations. Each deformed state and the corresponding energy surface are obtained by choosing the values of α and β_2 (**Figure. 6.2**).

The calculation is performed by the SkyAX code [58] in which the quadrupole deformation is given on the three-dimensional Cartesian coordinate. In the SkyAx code, the octupole moment is optimized by adding a small octupole moment to the initial wave functions under the quadrupole constraint. Although the axial symmetry is assumed for the SkyAX calculations, it does not require anything more for the quadrupole constraint calculations. Indeed, the quadrupole-deformed nuclei can be fully described within axial symmetric framework. Two different effective nuclear interactions SLy4 [19] and SkM* [8] are examined with the density-dependent pairing

TABLE 6.3: Nuclear radius (proton radius - neutron radius - total radius) [fm]. The calculated values using original interactions (SLy4 and SkM*) and the proposed interactions (mSLy4 and mSkM*) are shown. Note that experimental radius is charge radius.

	Experiment [5]	SLy4	SkM*	mSLy4	mSkM*
^{208}Pb	5.50	5.46 - 5.62 - 5.55	5.53 - 5.62 - 5.56	5.70 - 5.84 - 5.78	5.58 - 5.74 - 5.68
^{120}Sn	4.65	4.59 - 4.73 - 4.68	4.58 - 4.73 - 4.67	4.79 - 4.92 - 4.86	4.68 - 4.83 - 4.77
^{90}Zr	4.27	4.23 - 4.28 - 4.26	4.23 - 4.28 - 4.26	4.40 - 4.47 - 4.43	4.32 - 4.37 - 4.35
^{40}Ca	3.48	3.45 - 3.38 - 3.41	3.46 - 3.40 - 3.43	3.57 - 3.50 - 3.53	3.53 - 3.47 - 3.50
^{16}O	2.70	2.79 - 2.72 - 2.76	2.77 - 2.71 - 2.74	2.83 - 2.76 - 2.80	2.84 - 2.78 - 2.81

interaction. By focusing on the three-body force effects being included in the density dependent force term, the fission barrier height is systematically calculated for Thorium, Protactinium, Uranium, Neptunium, Plutonium, Americium, and Curium isotopes (for a complete list of calculated nuclei, see Figure 6.5 and Table A.1 in Appendix, and the minor actinides are widely covered. Possibly due to the inclusion of the pairing interaction, the quality of barrier height calculations for odd-odd, odd-even and even-odd nuclei are as good as those for even-even nuclei. We have decided to include those odd nuclei in our analysis.

6.3.2 Skyrme fractional-power perturbation

As seen in Figure 6.5 and Table A.1 in Appendix, the original effective nuclear force overestimates the fission barrier height, and we propose a modified force parameters adding a perturbation to the fractional-power. Indeed, as an average of the difference between experiment and theory is 3.81 MeV (inner barrier) for SLy4, and 2.14 MeV (inner barrier) for SkM*. It provides us a sound motivation to modify the existing Skyrme parameter sets; in the following, SLy4 and SkM* are adopted.

The fractional power perturbation optimizes the nuclear medium effects. For any Skyrme parameters, we focus on the competition between $t_0\rho^2$ (two-body force) and $t_3\rho^{2+\alpha}$ (many-body force) in order to have a better description of fission and a better prediction power for heavy nuclear physics in general. The refit scheme of fractional power perturbation is shown as follows.

- adding a perturbation $\delta\alpha$ to fit the theoretically calculated fission barrier heights to the experiments;
- changing the parameter t_3 to keep the quality of the original interaction in terms of reproducing the basic and static properties;

in this way a whole t_3-term is optimized to reproduce the fission property well. The validity of the fractional power perturbation scheme is checked whether

$$\left| 1 - \frac{< \psi | t_3' \rho^{2+\alpha+\delta\alpha} | \psi >}{< \psi | t_3 \rho^{2+\alpha} | \psi >} \right| < 0.05 \tag{6.29}$$

is satisfied or not, where $\delta\alpha$ is a perturbation, and t_3' is a modified parameter of t_3. This condition of permitting 5% difference is reasonable, because almost a few % differences of binding energy already exist in the original interactions (**Table 6.2**). In summary, for finding better effective interaction parameter sets, the proposed fractional power perturbation makes use of the different mathematical behavior due to the power index (α) and the multiplication parameter (t_3).

In this paper, the experimental inner fission barrier height of ^{236}U is utilized to modify the effective nuclear force parameters. The differences between the theoretical and the experimental values are 2.36 MeV for SLy4, and 2.53 MeV for SkM*. For the modification, the calculated inner fission barrier height of ^{236}U is fitted to the experimental value, and the binding energy of ^{236}U is also fitted to keep the original quality of the interactions. As a result to two reference values are optimized by two variables t_3 and α. For the validity check, the binding energies and the radii of ^{16}O, ^{40}Ca, ^{90}Zr, ^{120}Sn, and ^{208}Pb are also utilized, as they are referred to in most of Skyrme parameter fittings.

6.4 Results and discussions

6.4.1 Validity of Skyrme fractional power perturbation

We propose two modified Skyrme parameter sets mSLy4 and mSkM* starting with SLy4 and SkM*, respectively. The original values of α is equal to $1/6 = 0.167$, and it is changed from 0.133, 0.142, $\cdots$, 0.217 in parameter-searching calculations. In order to optimize the calculated fission barrier height, the potential energy surface of ^{236}U is calculated by changing α and t_3 simultaneously. The parameter t_3 plays a role of an adjusting parameter to keep the original value of the binding energy of ^{236}U. As a result, the potential energy surface is systematically obtained for each α value (Figure 6.2), and the height of the inner potential barrier located around $\beta = 0.5$ is compared to the experiment. Roughly speaking, in terms of the fission barrier height, we see that α should be around 0.19. Note that the potential surfaces shown in Figure 6.2 are the potentials calculated by the effective nuclear force with the similar quality to original SLy4 interaction in terms of binding energy. Almost 0.02 difference of α-value leads to 4 MeV difference of fission barrier height. It implies the large impact of many-body force effect on the fission dynamics. In particular we found that the lower fission barrier heights are calculated by larger α values, and vice versa. That is, the many-body force effect lowers the fission barrier. This fact was generally found in all the calculated cases without exceptions. Being distinct from the barrier height, the deformation of the ground states are not so different for the three cases, ($\beta \sim 0.25$), as well as the deformation of the barrier tops ($\beta \sim 0.50$). It implies a quite limited many-body force effect on the deformation. Eventually, according to the comparison to the experiments, $\alpha = 0.196$ is chosen for the new α-value for the modified SLy4 interaction, and $\alpha = 0.179$ for the modified SkM* interaction (Figure 6.5 and **Table A.2** in Appendix).

For the validity check, we use the binding energies of the selected reference nuclei. Table 6.2 shows the binding energies obtained by the proposed effective interactions. The difference compared to the experimental values is less than 5%. In the case of ^{208}Pb, the difference is 0.13% for mSLy4, and 0.889% for mSkM*. In the case of ^{120}Sn, the difference is 0.24% for mSLy4, and 0.588% for mSkM*. In the case of ^{90}Zr, the difference is 1.03% for mSLy4, and 2.99% for mSkM*. In the case of ^{40}Ca, the difference is 3.04% for mSLy4, and 1.40% for mSkM*. In the case of ^{16}O, the difference is 4.89%

for mSLy4, and 3.38% for mSkM*. In summary we see that the condition (6.29) is satisfied.

For the further validity check, we calculate the root mean square radius of the reference nuclei **(Table 6.3)**. The difference compared to the experimental values (for the theory, proton radius) is less than 5%. Indeed, in the case of ^{208}Pb, the difference is 3.51% for mSLy4, and 1.43% for mSkM*. In the case of ^{120}Sn, the difference is 2.92% for mSLy4, and 0.64% for mSkM*. In the case of ^{90}Zr, the difference is 2.96% for mSLy4, and 1.16% for mSkM*. In the case of ^{40}Ca, the difference is 2.52% for mSLy4, and 1.42% for mSkM*. In the case of ^{16}O, the difference is 4.59% for mSLy4, and 4.93% for mSkM*. This is permissible, because almost similar difference can be found for the original interactions.

As a common feature for both binding energies and nuclear radii, the proposed method works rather well for heavier nuclei, and larger discrepancies can be found in the lighter cases. Consequently, in terms of the binding energies and the nuclear radii, we see that the quality of the original interaction is well preserved in the proposed mSLy4 and mSkM* interactions.

6.4.2 Density dependence of many-body force

Let us begin with figuring out what is modified by the new interaction. The competition between two-body force and many-body force is examined by ρ dependence of

$$t_0\rho^2 + \frac{t_3}{6}\rho^{2+\alpha}. \tag{6.30}$$

As estimated in Fig. 6.3, there exist minimums in any cases (the most stable density as an average), and the minimum becomes larger due to the modification. The density dependent terms (6.30) behave as the attractive force (negative-valued) for the low density situation, while they behave as the repulsive force (positive-valued) for the high density situation. This is in accordance with the known fact that the sign of the many-nucleon force can be mostly repulsive in the mean-field description. This feature is commonly true to four effective interactions, and quite similar dependence can also be found for lower densities satisfying $\|\rho\| < 0.25$. As a result, Figure 6.3 shows that the modification is weakening the attractive force.

The parameter analysis clarifies a linear relation between the parameters t_3 and α. In order to determine t_3 and α simultaneously, it is practical to have a priori estimate of t_3 values only by imposing the energy condition (6.29). We found a useful relation

$$t_3 = 29774.757\alpha + 8810.842 \tag{6.31}$$

for SLy4, and

$$t_3 = 34868.794\alpha + 9762.947 \tag{6.32}$$

for SkM*. The proportional relations are true for both interactions SLy4 and SkM* (Figure 6.4). The parameter α should not be taken as an independent number, and here is a simple linear dependence between the multiplication effect (t_3 value) and the power effect (α value). These formulae are utilizable to change the reference nuclei; e.g., U^{236}. We observe that t_3 increases as a linear function of α for both interactions. This is because ρ^α decrease when α increase since $\rho < 1$, thus t_3 has to be increased in order to keep the binding energy the same as that produced by the original interactions (t_3 and α). The linear relations between t_3 and α can be interpreted as following. To conserve the binding energy by changing t_3 and α, we have to keep the value of

the term $\frac{t_3}{6}\rho^{2+\alpha}$. We changed from t_3 and α to t_3' and $\alpha' = \alpha + \Delta\alpha$. We obtained

$$t_3'\rho^{2+\alpha+\Delta\alpha} = t_3\rho^{2+\alpha}. \tag{6.33}$$

The $\rho^{2+\alpha}$ term can be simplified. Then Eq. 6.33 becomes

$$t_3'\rho^{\Delta\alpha} = t_3. \tag{6.34}$$

t_3' is deduced as

$$t_3' = \frac{t_3}{\rho^{\Delta\alpha}}. \tag{6.35}$$

We define

$$y = \rho^{\Delta\alpha}. \tag{6.36}$$

We put the logarithm on both sides of Eq. 6.36, it can be written as

$$\ln y = \Delta\alpha \ln\rho. \tag{6.37}$$

We do the partial derivation on Eq. 6.37

$$\frac{\partial \ln y}{\partial\Delta\alpha} = \frac{\partial y}{y\partial\Delta\alpha} = \ln\rho. \tag{6.38}$$

We can write

$$\frac{\partial y}{\partial\Delta\alpha} = y\ln\rho. \tag{6.39}$$

By using Taylor's expansion, Eq. 6.36 expresses

$$y = \rho^{\Delta\alpha} \approx 1 + \left(\frac{\partial y}{\partial\Delta\alpha}\right)_{\Delta\alpha=0}\Delta\alpha. \text{ (The higher order terms are ignored .)} \tag{6.40}$$

Since

$$\left(\frac{\partial y}{\partial\Delta\alpha}\right)_{\Delta\alpha=0} = \ln\rho. \tag{6.41}$$

We define $\ln\rho = -\beta$ assumed to be a constant, we can write

$$y = \rho^{\Delta\alpha} \approx 1 - \beta\Delta\alpha. \tag{6.42}$$

Eq. 6.42 is plugged in Eq. 6.35, t_3' can be derived as

$$t_3' = \frac{t_3}{1-\beta\Delta\alpha} \approx t_3(1+\beta\Delta\alpha). \tag{6.43}$$

We can write t_3' as a function of $\alpha' = \alpha + \Delta\alpha$

$$t_3' \approx t_3 + t_3\beta(\alpha+\Delta\alpha) - t_3\beta\alpha. \tag{6.44}$$
$$\approx t_3(1-\beta\alpha) + t_3\beta\alpha'. \tag{6.45}$$

We fine two constants which are $a = t_3\beta$ and $b = t_3(1-\beta\alpha)$, and also we substitute t_3' and α' by t_3 and α, respectively. Finally, we can write the linear relation between t_3 and α

$$t_3 \approx a\alpha + b. \tag{6.46}$$

By comparing Eq. 6.46 with Eq. 6.31 and Eq. 6.32, a = 29774.757 and b = 8810.842 for SLy4, and a = 34868.794 and b = 9762.947 for SkM*.

6.4.3 The fission barrier height

The fission barrier height is systematically calculated for 43 nuclei chosen from Thorium, Protactinium, Uranium, Neptunium, Plutonium, Americium, and Curium isotopes. The 43 nuclei are selected based on whether the comparable experimental data [18] are available or not. In Figure 6.5, the fission barrier heights calculated by the modified interactions are compared to those by the original interactions. As a general trend, overestimated fission barrier heights are improved by the the modified interactions. As an average for 43 isotopes, the difference of inner barrier height between experiment and theory is 0.66 MeV for mSLy4, and 0.46 MeV for mSkM*. The precision of fission barrier height calculations is almost 80% improved from the original cases, and the modified interaction describes the fission barrier height within 0.7 MeV errors as an average. Due to the modification, the distribution areas of points in Figure 6.5 are compressed for the perpendicular direction entailing the parallel shifts. It implies that the isotope dependence of barrier heights is also well preserved, so that a rather direct relation between the many-body force term and the fission barrier height is noticed at last. In terms of reproducing the experimental fission barrier heights, Figures 6.3 and 6.5 may explain why the original SkM* interaction is better than SLy4 interaction as only SLy4 is located separately from the others in Figure 6.3. Although $x_3 = 0.000$ is assumed for SkM*, and $x_3 = 1.354$ for SLy4 even within t_3 term, such a difference is not significantly noticed in the present systematics. All the calculated values are shown in Table A.2 (Appendix).

6.4.4 The many-body force effects on heavy nuclei

To show the impact magnitudes of many body force term on the fission barrier height and the binding energy of heavy nuclei, we calculated the change of fission barrier height (FB ratio) and the change of binding energy (BE ratio) as a function of the change of alpha (α ratio), as shown in Figure. 6.6. We changed α value by ± 5 % with respect to its original value. In these calculations, the Skyrme parameter set is refitted by the fractional power perturbation in terms of keeping the binding energy of reference nuclei. Note that the above 43 nuclei are employed in these calculations. As a result, with respect to 5% α-perturbation analysis for both SLy4 and SkM*, the validity of fractional power perturbation is confirmed in which the the binding energy is well preserved within 3 % difference, while the fission barrier height achieves 20-30 % differences. Among several features, we found the fission barrier height is quite sensitive to the α value. Almost 10 times larger effect of α on the fission barrier height than on the binding energy is clarified by the fractional power perturbation. It is remarkable that not only the binding energy of ^{236}U but also the binding energies of the other nuclei experiences almost the same amount (ratio) of changes. This fact is also confirmed if the equally conditioned analysis with changing only α value is executed.

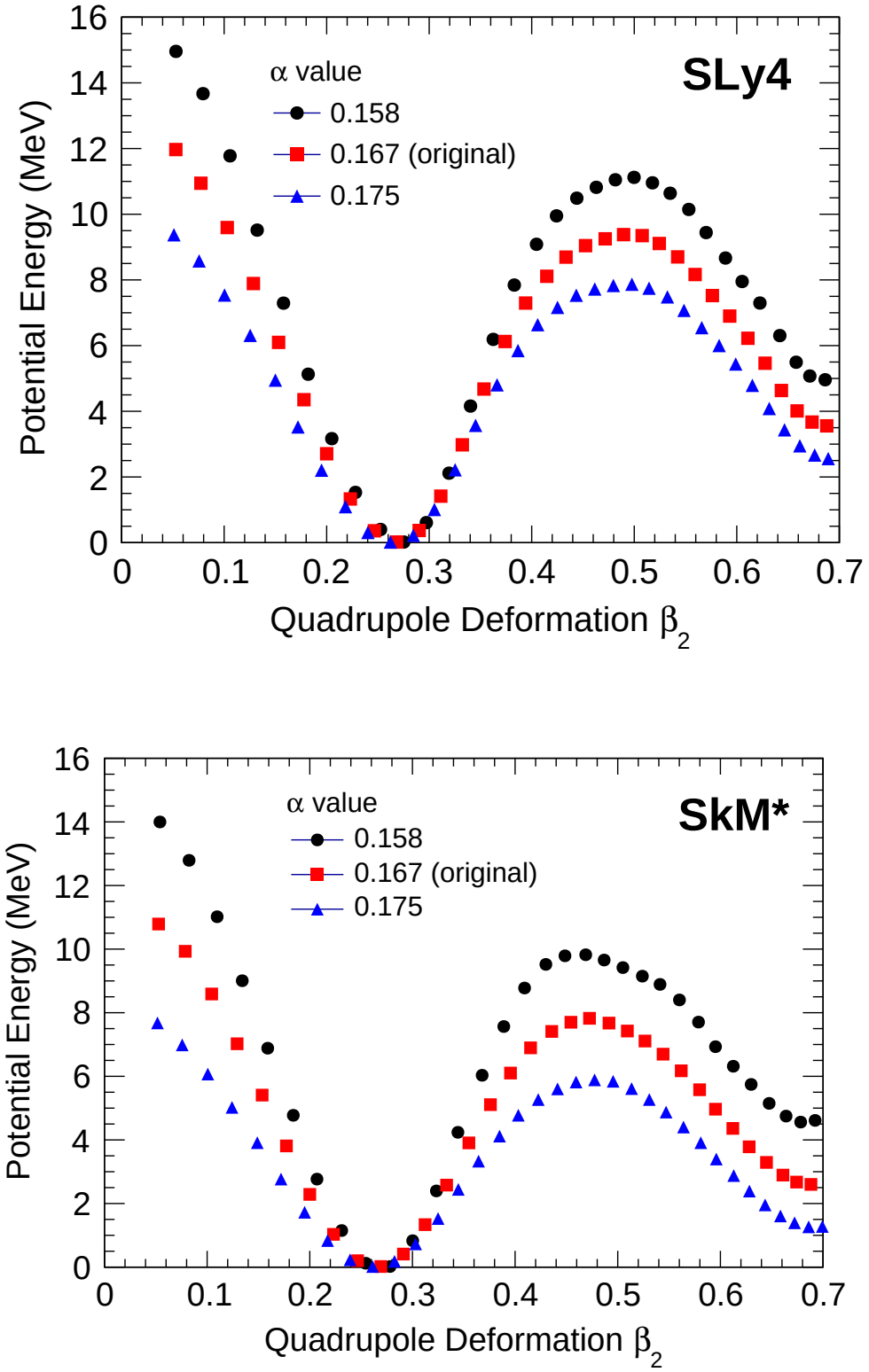

FIGURE 6.2: (Color online) α dependence of the potential energy surface of ^{236}U for SLy4 and SkM*. The different α values with $\pm 5\%$ from the original value $\alpha = 1/6$ are examined, where the 3-digits rounded α-values are shown for the better comparison. In each case, parameters α and t_3 are optimized simultaneously to fulfill the scheme. Note that the binding energy of ^{236}U is preserved to be the same. The experimental value for the barrier is 5.0 MeV in this case.

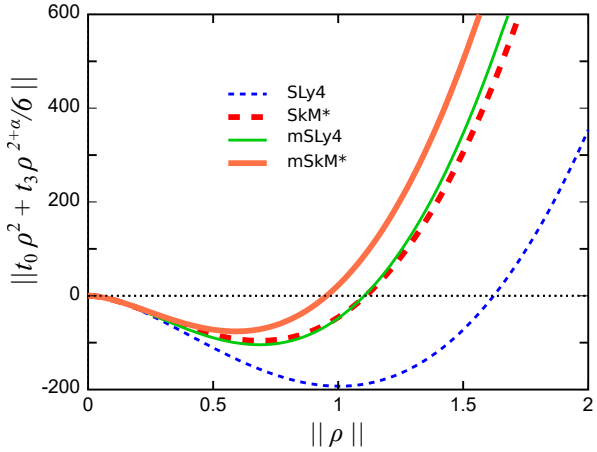

FIGURE 6.3: (Color online) The density dependence of t_0 and t_3 terms. The normed estimation is carried out by assuming $\|t_0\rho^2 + t_3\rho^{2+\alpha}/6\| \sim t_0 \|\rho\|^2 + t_3 \|\rho\|^{2+\alpha}/6$, where note that t_3 is negative value. The curve shows only parabolic dependence, if we take $t_3 = 0$. Although it is not the exact manner, it is rather practical to see the curves by making upside down for presuming the competition of attractive t_0 and repulsive t_3 effects.

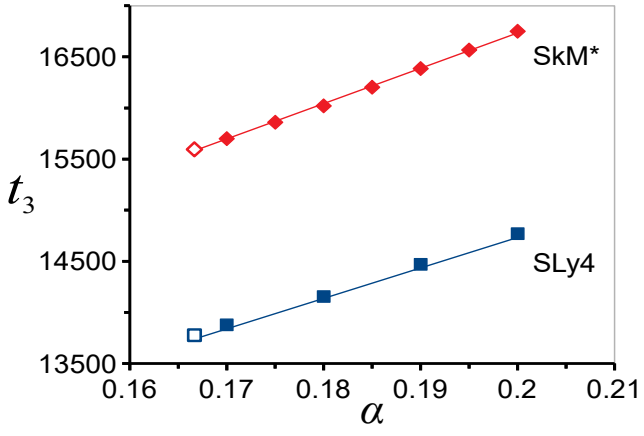

FIGURE 6.4: (Color online) Correlation between parameters t_3 and α. The original t_3 and α values are blank squares, and the obtained values are approximated by the linear regression. Since the total energy is preserved by the modification, these lines correspond to the iso-energetic lines for a whole t_3 term.

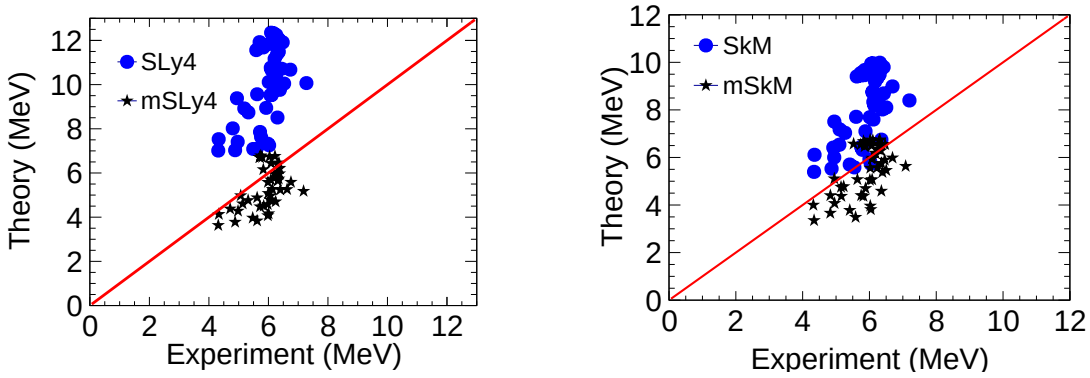

FIGURE 6.5: (Color online) Comparison to the experimental fission barrier height. The experimental and theoretical values are for the horizontal axis, and the vertical axis, respectively. Blue circles denote the calculations using original parameter set (SLy4 and SkM*), and black stars denote the calculations using proposed parameter set (mSLy4 and mSkM*)..

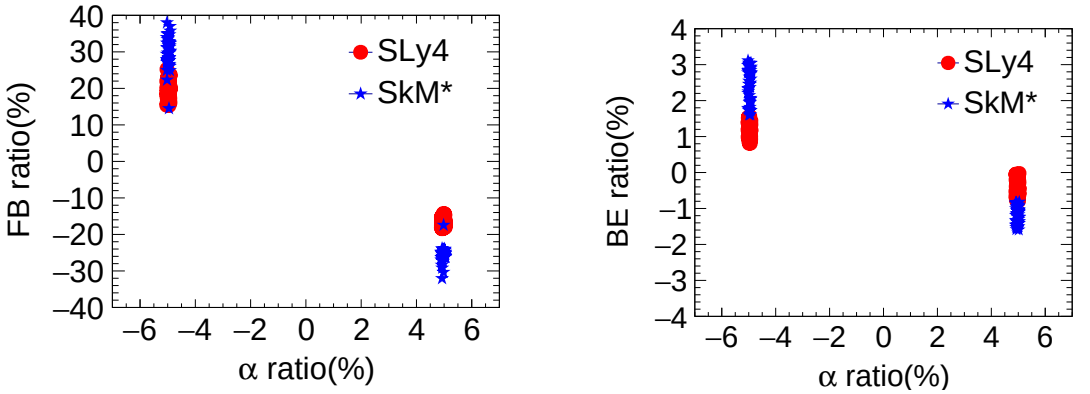

FIGURE 6.6: The calculated binding energy change (BE ratio) as a function of the change of alpha (α ratio), and the calculated fission barrier height change (FB ratio) as a function of the change of alpha (α ratio) are illustrated. The changes arising from $\pm 5\%$ of α-values from the original value are plotted (cf. Fig. 6.2) based on the fractional power perturbation theory. Almost 10 times larger effect on the fission barrier height than on the binding energy is noticed. Note that the calculated fission barrier heights of 43 heavy nuclei with both SLy4 and SkM* are included in these plots.

Chapter 7

Conclusion and outlooks

7.1 Experiments

In the present work, the fissio barrier heights of ^{239}Np,^{239,240}Pu nuclei were deduced by using the MNT-idnduce fission reactions. A good agreement between the previous known data, originating from neutron-induced and particle-induced reaction, was demonstrated. This fact allows one to confirm the validitgy of the MNT menthod.

The demonstrated agreement of the B_f results obtained in the present study with known fission-barrier data from different neutron (RIPL3) and particle-transfer ((t,p), (^{3}He,d)) reactions allows one to extend the validity of the transfer-reaction technique for the fission-barrier studies to the ^{18}O beam.

We find that the MNT-technique with heavy ion beam, e.g ^{18}O as in this case, allows for a variety of compound nuclei to be created and simultaneously investigated for fission properties. In particular, the ^{18}O + ^{237}Np MNT-reactions producing oxygen, nitrogen, and carbon isotopes as ejectiles can be used for the fission-barrier determination, as they produce fissioning elements at sufficiently low excitation energy. In contrast to this, the compound nuclei of Cm, Bk and Cf corresponding to light ejectiles such as B, Be and Li, respectively, are poorly produced at the excitation energies comparable with, or below, the fission-barrier height, which shrinks the number of the MNT channels suitable for the fission-barrier studies. However, the fission barriers of heavier nuclei can be accessed by using MNT reactions on heavier and more exotic target nuclei , such as ^{244}Pu, ^{243}Am, ^{249}Cm, ^{249}Bk, ^{249}Cf.

In summary, direct-kinematics multi-nucleon transfer reactions using ^{18}O as projectile is a useful tool for a simultaneous determination of fission-barrier heights for a wide range of nuclei in the actinide region.

7.2 Theory

The Skyrme fractional power perturbation is introduced based on the Hartree-Fock+BCS framework. It improves the description of heavy nuclei by their fission barrier heights without losing the original quality of the Skyrme interactions. The different mathematical behavior due to the power index (α) and the multiplication parameter (t_3) is essential, and it is confirmed to be working well (Figure 6.6). The perturbation scheme is successfully carried out by the newly-found relation shown in Figure 6.4. As an average, the description of fission barrier height is improved by almost 80 %. The obtained interactions mSLy4 and mSkM* are shown in Table A.2, which are to be utilized for the fission barrier height measurements. Although the breaking of axial symmetry has been reported to be a large effect on fission barriers (inner barrier in actinides by a few MeV [2] roughly corresponding to 0.01 difference of α value), this

point is not taken into account in the present calculation. In this sense, the proposed α value still holds the ambiguity around the precision of the order 0.01.

The nuclear medium effect is represented by the density dependent force term of the energy density functional including three-body force, four-body force and higher-order many-body forces. The classification of nuclear medium effect is made with respect to the density dependent force. The modified α values are located between $\alpha = 1/6$ and $\alpha = 1/3$, so that they are regarded as a mixture of several types of many-body force. Indeed, in Figure 6.3, many-body force effects are moderately changed by changing α value, where the details of many-body force cannot be identified only by the α value itself, while it can be assessed by the difference from the parabolic dependence presented in Figure 6.3.

Eventually, according to a systematic calculation for Thorium, Protactinium, Uranium, Neptunium, Plutonium, Americium, and Curium isotopes, the nuclear many-body force effect is shown to have a significantly large impact on the description of heavy nuclei. Indeed, almost several 10 times larger effect on the fission barrier height than on the binding energy is presented (Figure 6.6). As a minor finding within the fractional power perturbation results, the lower fission barrier heights are calculated for larger α values, and vice versa. This fact has been confirmed to be true being independent of effective interactions (at least for SLy4 and SkM*). The density functional calculations suggest that one possible driving force of nuclear fission is identified to be the nuclear many-body (more than two-body) force. Although the fission mechanism has been explained by the competition between the surface tensor and the Coulomb repulsion, the present research shows the 3-body force plays a role in the surface tension and the tension acting on the neck.

The nuclear force is still a mysterious issue in sub-atomic physics. The rather direct relation between the nuclear many-body force and the fission property is suggested in the present article. In terms of nuclear density functional theory, there have been many works of Skyrme parametrization in the context of finding the ultimate nuclear energy density functional (for examples of recent works, see Refs. [42, 43, 15]) . The proposed scheme will provide a simple solution to the Skyrme parametrization towards the heavy nuclear physics.

7.3 Grand conclusion

As a grand conclusion, the fission barrier height can be accessed by both experiment using MNT with ^{18}O beam and the theoretical calculation performing the constrained HF + BCS with our newly proposed interaction (mSkM* and mSLy4). Our new proposed-interactions better reproduced the fission barrier heights with respect to the original interaction SkM* and SLy4 with axial-symmetric assumption, as indicated in Tab. 7.1.

TABLE 7.1: The inner fission barrier heights B_f for ^{239}Np and ^{239,240}Pu isotopes from this work compared with the theoretical calculation using the constrained Hartree-Fock + BCS model with Skyrme interactions (SkM* and SLy4) and with new proposed interactions (mSkM* and mSLy4).

Isotope	This work	SLy4	SkM*	mSLy4	mSkM*
^{239}Np	5.87 ± 0.09	10.3	8.50	—	—
^{239}Pu	6.14 ± 0.12	10.1	8.25	5.25	5.55
^{240}Pu	6.25 ± 0.32	10.6	8.76	5.59	5.87

Appendix A

TABLE A.1: Fission barrier height of heavy nuclei [MeV]: inner barrier (left) and outer barrier (right). The calculated results using SLy4 and SkM* are compared to the experimental data [18].

	Experiment (RIPL-2 [18])	SLy4	SkM*
^{230}Th	6.10, 6.80	7.21, 9.57	5.73, 6.63
^{231}Th	6.00, 6.70	7.36, 9.12	5.91, 6.35
^{232}Th	5.80, 6.70	7.58, 9.05	6.25, 6.28
^{230}Pa	5.60, 5.80	7.07, 9.65	5.56, 6.28
^{231}Pa	5.50, 5.50	7.14, 8.71	5.65, 6.05
^{232}Pa	5.00, 6.40	7.46, 8.61	6.04, 6.03
^{233}Pa	5.70, 5.80	7.92, 8.80	6.39, 5.97
^{234}Pa	6.30, 6.15	8.57, 9.18	6.76, 6.08
^{231}U	4.40, 5.50	6.90, 6.51	5.34, 5.50
^{232}U	4.90, 5.40	7.10, 8.66	5.63, 5.48
^{233}U	4.35, 5.55	7.49, 8.09	6.01, 5.55
^{234}U	4.80, 5.50	8.02, 8.31	6.45, 6.60
^{235}U	5.25, 6.00	8.77, 8.75	6.99, 5.86
^{236}U	5.00, 5.67	7.36, 8.29	7.53, 6.18
^{237}U	6.40, 6.15	9.86, 8.52	7.93, 6.46
^{238}U	6.30, 5.50	10.2, 8.92	6.37, 6.97
^{239}U	6.45, 6.00	10.7, 9.28	8.70, 8.21
^{236}Np	5.90, 5.40	8.87, 8.27	7.11, 5.49
^{237}Np	6.00, 5.40	9.52, 8.39	7.66, 7.76
^{238}Np	6.50, 5.75	10.0, 8.35	8.16, 6.18
^{237}Pu	5.10, 5.15	8.92, 7.69	7.17, 4.50
^{238}Pu	5.60, 5.10	9.55, 8.14	7.75, 5.34
^{239}Pu	6.20, 5.70	10.1, 8.67	8.25, 5.62
^{240}Pu	6.05, 5.15	10.6, 8.79	8.76, 6.08
^{241}Pu	6.15, 5.50	11.2, 8.81	9.19, 6.34
^{242}Pu	5.85, 5.05	11.6, 8.92	9.48, 6.69
^{243}Pu	6.05, 5.45	11.8, 9.07	9.56, 6.97
^{244}Pu	5.70, 4.85	11.9, 9.34	9.49, 7.19
^{245}Pu	5.85, 5.25	11.7, 10.2	9.37, 7.52
^{239}Am	6.00, 5.40	9.51, 7.50	7.74, 4.75
^{240}Am	6.10, 6.00	10.1, 8.00	8.29, 5.05
^{241}Am	6.00, 5.35	10.7, 8.66	8.87, 5.43
^{242}Am	6.32, 5.78	11.3, 8.54	9.35, 5.89
^{243}Am	6.40, 5.05	11.9, 8.57	9.74, 6.26
^{244}Am	6.25, 5.90	12.1, 8.74	9.81, 8.52
^{241}Cm	7.15, 5.50	10.1, 7.39	8.35, 4.45
^{242}Cm	6.65, 5.00	10.7, 8.04	9.00, 4.94
^{243}Cm	6.33, 5.40	11.5, 8.25	9.53, 5.32
^{244}Cm	6.18, 5.10	12.0, 8.21	9.91, 9.74
^{245}Cm	6.35, 5.45	12.3, 8.51	10.0, 6.02
^{246}Cm	6.00, 4.80	12.4, 9.14	10.0, 6.25
^{247}Cm	6.12, 5.10	12.2, 9.86	9.92, 6.58
^{248}Cm	5.80, 4.80	11.8, 10.7	9.68, 6.02
^{249}Cm	5.63, 4.95	11.5, 10.4	9.40, 5.50

TABLE A.2: Fission barrier height of heavy nuclei [MeV]: inner barrier (left) and outer barrier (right). The calculated results using the proposed interaction (mSLy4 and mSkM*) are compared to the experimental values.

	Experiment (RIPL-3 [18])	mSLy4	mSkM*
^{230}Th	6.10, 6.80	4.12, 6.17	3.80, 4.75
^{231}Th	6.00, 6.70	4.27, 6.17	4.03, 4.80
^{232}Th	5.80, 6.70	4.50, 6.42	4.32, 4.95
^{230}Pa	5.60, 5.80	3.82, 5.43	3.54, 4.15
^{231}Pa	5.50, 5.50	4.01, 5.47	3.74, 4.11
^{232}Pa	5.00, 6.40	4.19, 5.65	4.03, 4.19
^{233}Pa	5.70, 5.80	5.86, 4.44	4.34, 4.35
^{234}Pa	6.30, 6.15	4.70, 6.11	4.66, 4.55
^{231}U	4.40, 5.50	3.63, 4.72	3.36, 3.37
^{232}U	4.90, 5.40	3.84, 4.84	3.65, 3.45
^{233}U	4.35, 5.55	4.11, 4.99	4.01, 3.56
^{234}U	4.80, 5.50	4.38, 5.28	4.35, 3.76
^{235}U	5.25, 6.00	4.68, 5.56	4.74, 3.97
^{236}U	5.00, 5.67	5.00, 5.89	5.09, 4.27
^{237}U	6.40, 6.15	5.30, 6.15	5.37, 4.50
^{238}U	6.30, 5.50	5.60, 6.51	5.66, 4.78
^{239}U	6.45, 6.00	5.88, 6.90	5.88, 5.05
^{236}Np	5.90, 5.40	4.63, 4.89	4.79, 3.40
^{237}Np	6.00, 5.40	4.98, 5.21	5.15, 3.67
^{238}Np	6.50, 5.75	5.29, 5.51	5.48, 3.93
^{237}Pu	5.10, 5.15	4.55, 4.17	4.77, 2.74
^{238}Pu	5.60, 5.10	4.89, 4.47	5.16, 2.98
^{239}Pu	6.20, 5.70	5.25, 4.85	5.55, 3.31
^{240}Pu	6.05, 5.15	5.59, 5.25	5.87, 3.62
^{241}Pu	6.15, 5.50	5.90, 5.64	6.20, 3.96
^{242}Pu	5.85, 5.05	6.20, 6.06	6.39, 4.21
^{243}Pu	6.05, 5.45	6.46, 6.47	6.52, 4.41
^{244}Pu	5.70, 4.85	6.65, 6.60	6.59, 4.50
^{245}Pu	5.85, 5.25	6.73, 6.43	6.53, 4.16
^{239}Am	6.00, 5.40	4.80, 3.74	5.15, 2.29
^{240}Am	6.10, 6.00	5.19, 4.15	5.59, 2.66
^{241}Am	6.00, 5.35	5.56, 4.53	5.96, 2.99
^{242}Am	6.32, 5.78	5.90, 4.97	6.27, 3.29
^{243}Am	6.40, 5.05	6.22, 5.35	6.52, 3.59
^{244}Am	6.25, 5.90	6.49, 5.75	6.68, 3.78
^{241}Cm	7.15, 5.50	5.12, 3.39	5.56, 1.92
^{242}Cm	6.65, 5.00	5.49, 3.79	5.96, 2.28
^{243}Cm	6.33, 5.40	5.84, 4.21	6.30, 2.61
^{244}Cm	6.18, 5.10	6.18, 4.59	6.54, 2.87
^{245}Cm	6.35, 5.45	6.46, 5.02	6.76, 3.09
^{246}Cm	6.00, 4.80	6.68, 4.91	6.83, 3.12
^{247}Cm	6.12, 5.10	6.77, 4.63	6.79, 2.85
^{248}Cm	5.80, 4.80	6.77, 4.23	6.72, 2.52
^{249}Cm	5.63, 4.95	6.65, 3.79	6.56, 2.14

Bibliography

[1] NuDat 2.7. In: *National Nuclear Data Center, Brookhaven National Laboratory* (). URL: https://www.nndc.bnl.gov/nudat2/.

[2] H. Abusara, A. V. Afanasjev, and P. Ring. "Fission barriers in actinides in covariant density functional theory: The role of triaxiality". In: *Phys. Rev. C* 82 (4 2010), p. 044303. DOI: 10.1103/PhysRevC.82.044303. URL: https://link.aps.org/doi/10.1103/PhysRevC.82.044303.

[3] Japan Atomic Energy Agency. In: *Tandem accelerator* (2019). URL: https://www.jaea.go.jp/english/04/ntokai/kasokuki/kasokuki_04.html.

[4] A. N. Andreyev, K. Nishio, and K-H Schmidt. "Nuclear fission: a review of experimental advances and phenomenology". In: *Reports on Progress in Physics* 81.1 (2017), p. 016301. DOI: 10.1088/1361-6633/aa82eb. URL: https://doi.org/10.1088%2F1361-6633%2Faa82eb.

[5] I. Angeli and K.P. Marinova. "Table of experimental nuclear ground state charge radii: An update". In: *Atomic Data and Nuclear Data Tables* 99.1 (2013), pp. 69 –95. ISSN: 0092-640X. DOI: https://doi.org/10.1016/j.adt.2011.12.006. URL: http://www.sciencedirect.com/science/article/pii/S0092640X12000265.

[6] B. B. Back et al. "Fission of doubly even actinide nuclei induced by direct reactions". In: *Phys. Rev. C* 9 (5 1974), pp. 1924–1947. DOI: 10.1103/PhysRevC.9.1924. URL: https://link.aps.org/doi/10.1103/PhysRevC.9.1924.

[7] B. B. Back et al. "Fission of odd-*A* and doubly odd actinide nuclei induced by direct reactions". In: *Phys. Rev. C* 10 (5 1974), pp. 1948–1965. DOI: 10.1103/PhysRevC.10.1948. URL: https://link.aps.org/doi/10.1103/PhysRevC.10.1948.

[8] J. Bartel et al. "Towards a better parametrisation of Skyrme-like effective forces: A critical study of the SkM force". In: *Nuclear Physics A* 386.1 (1982), pp. 79 –100. ISSN: 0375-9474. DOI: https://doi.org/10.1016/0375-9474(82)90403-1. URL: http://www.sciencedirect.com/science/article/pii/0375947482904031.

[9] M. Bender et al. "Potential energy surfaces of superheavy nuclei". In: *Phys. Rev. C* 58 (4 1998), pp. 2126–2132. DOI: 10.1103/PhysRevC.58.2126. URL: https://link.aps.org/doi/10.1103/PhysRevC.58.2126.

[10] H. A. Bethe. "Nuclear Physics B. Nuclear Dynamics, Theoretical". In: *Rev. Mod. Phys.* 9 (2 1937), pp. 69–244. DOI: 10.1103/RevModPhys.9.69. URL: https://link.aps.org/doi/10.1103/RevModPhys.9.69.

[11] H. A. Bethe and R. F. Bacher. "Nuclear Physics A. Stationary States of Nuclei". In: *Rev. Mod. Phys.* 8 (2 1936), pp. 82–229. DOI: 10.1103/RevModPhys.8.82. URL: https://link.aps.org/doi/10.1103/RevModPhys.8.82.

[12] S. Bjørnholm and J. E. Lynn. "The double-humped fission barrier". In: *Rev. Mod. Phys.* 52 (4 1980), pp. 725–931. DOI: 10.1103/RevModPhys.52.725. URL: https://link.aps.org/doi/10.1103/RevModPhys.52.725.

[13] Niels Bohr and John Archibald Wheeler. "The Mechanism of Nuclear Fission". In: *Phys. Rev.* 56 (5 1939), pp. 426–450. DOI: 10.1103/PhysRev.56.426. URL: https://link.aps.org/doi/10.1103/PhysRev.56.426.

[14] H. C. Britt and J. B. Wilhelmy. "Simulated (n,f) Cross Sections for Exotic Actinide Nuclei". In: *Nuclear Science and Engineering* 72.2 (1979), pp. 222–229. DOI: 10.13182/NSE72-222. eprint: https://doi.org/10.13182/NSE72-222. URL: https://doi.org/10.13182/NSE72-222.

[15] Aurel Bulgac et al. "Minimal nuclear energy density functional". In: *Phys. Rev. C* 97 (4 2018), p. 044313. DOI: 10.1103/PhysRevC.97.044313. URL: https://link.aps.org/doi/10.1103/PhysRevC.97.044313.

[16] J. T. Burke et al. "Deducing the ^{237}U(n, f) cross section using the surrogate ratio method". In: *Phys. Rev. C* 73 (5 2006), p. 054604. DOI: 10.1103/PhysRevC.73.054604. URL: https://link.aps.org/doi/10.1103/PhysRevC.73.054604.

[17] T. Burvenich et al. "Publisher's Note: Systematics of fission barriers in superheavy elements [Phys. Rev. C 69, 014307 (2004)]". In: *Phys. Rev. C* 69 (2 2004), p. 029901. DOI: 10.1103/PhysRevC.69.029901. URL: https://link.aps.org/doi/10.1103/PhysRevC.69.029901.

[18] Roberto Capote et al. "RIPL–reference input parameter library for calculation of nuclear reactions and nuclear data evaluations". In: *Nuclear Data Sheets* 110 (Jan. 2009), pp. 3107–3214.

[19] E. Chabanat et al. "A Skyrme parametrization from subnuclear to neutron star densities Part II. Nuclei far from stabilities". In: *Nuclear Physics A* 635.1 (1998), pp. 231 –256. ISSN: 0375-9474. DOI: https://doi.org/10.1016/S0375-9474(98)00180-8. URL: http://www.sciencedirect.com/science/article/pii/S0375947498001808.

[20] E. Cheifetz, H. C. Britt, and J. B. Wilhelmy. "Fission probabilities for actinide nuclei excited by the (^{12}C, ^{8}Be$_{g.s.}$) reaction". In: *Phys. Rev. C* 24 (2 1981), pp. 519–522. DOI: 10.1103/PhysRevC.24.519. URL: https://link.aps.org/doi/10.1103/PhysRevC.24.519.

[21] J. D. Cramer and H. C. Britt. "Neutron Fission Cross Sections for 231Th, 233Th, 235U, 237U, 239U, 241Pu, and 243Pu from 0.5 to 2.25 MeV Using (t, pf) Reactions". In: *Nuclear Science and Engineering* 41.2 (1970), pp. 177–187. DOI: 10.13182/NSE70-A20705. eprint: https://doi.org/10.13182/NSE70-A20705. URL: https://doi.org/10.13182/NSE70-A20705.

[22] J. D. Cramer and J. R. Nix. "Exact Calculation of the Penetrability Through Two-Peaked Fission Barriers". In: *Phys. Rev. C* 2 (3 1970), pp. 1048–1057. DOI: 10.1103/PhysRevC.2.1048. URL: https://link.aps.org/doi/10.1103/PhysRevC.2.1048.

[23] Q. Ducasse et al. "Investigation of the ^{238}U(d, p) surrogate reaction via the simultaneous measurement of γ-decay and fission probabilities". In: *Phys. Rev. C* 94 (2 2016), p. 024614. DOI: 10.1103/PhysRevC.94.024614. URL: https://link.aps.org/doi/10.1103/PhysRevC.94.024614.

[24] Jutta E. Escher and Frank S. Dietrich. "Cross sections for neutron capture from surrogate measurements: An examination of Weisskopf-Ewing and ratio approximations". In: *Phys. Rev. C* 81 (2 2010), p. 024612. DOI: 10.1103/PhysRevC.81.024612. URL: https://link.aps.org/doi/10.1103/PhysRevC.81.024612.

[25] Jutta E. Escher and Frank S. Dietrich. "Determining (n, f) cross sections for actinide nuclei indirectly: Examination of the surrogate ratio method". In: *Phys. Rev. C* 74 (5 2006), p. 054601. DOI: 10.1103/PhysRevC.74.054601. URL: https://link.aps.org/doi/10.1103/PhysRevC.74.054601.

[26] H. Flocard et al. "Self-consistent calculation of the fission barrier of 240Pu". In: *Nuclear Physics A* 231.1 (1974), pp. 176 –188. ISSN: 0375-9474. DOI: https://doi.org/10.1016/0375-9474(74)90300-5. URL: http://www.sciencedirect.com/science/article/pii/0375947474903005.

[27] A. Gavron et al. "$\frac{\Gamma_n}{\Gamma_f}$ for actinide nuclei using (^{3}He, df) and (^{3}He, tf) reactions". In: *Phys. Rev. C* 13 (6 1976), pp. 2374–2384. DOI: 10.1103/PhysRevC.13.2374. URL: https://link.aps.org/doi/10.1103/PhysRevC.13.2374.

[28] P. Glässel, H. Rösler, and H.J. Specht. "Intermediate structure in the 239Pu(d, pf) reaction". In: *Nuclear Physics A* 256.2 (1976), pp. 220 –242. ISSN: 0375-9474. DOI: https://doi.org/10.1016/0375-9474(76)90105-6. URL: http://www.sciencedirect.com/science/article/pii/0375947476901056.

[29] Hans-Werner Hammer, Andreas Nogga, and Achim Schwenk. "Colloquium: Three-body forces: From cold atoms to nuclei". In: *Rev. Mod. Phys.* 85 (1 2013), pp. 197–217. DOI: 10.1103/RevModPhys.85.197. URL: https://link.aps.org/doi/10.1103/RevModPhys.85.197.

[30] Walter Hauser and Herman Feshbach. "The Inelastic Scattering of Neutrons". In: *Phys. Rev.* 87 (2 1952), pp. 366–373. DOI: 10.1103/PhysRev.87.366. URL: https://link.aps.org/doi/10.1103/PhysRev.87.366.

[31] Otto Haxel, J. Hans D. Jensen, and Hans E. Suess. "On the "Magic Numbers" in Nuclear Structure". In: *Phys. Rev.* 75 (11 1949), pp. 1766–1766. DOI: 10.1103/PhysRev.75.1766.2. URL: https://link.aps.org/doi/10.1103/PhysRev.75.1766.2.

[32] S. Hilaire, Ch. Lagrange, and A.J. Koning. "Comparisons between various width fluctuation correction factors for compound nucleus reactions". In: *Annals of Physics* 306.2 (2003), pp. 209 –231. ISSN: 0003-4916. DOI: https://doi.org/10.1016/S0003-4916(03)00076-9. URL: http://www.sciencedirect.com/science/article/pii/S0003491603000769.

[33] David Lawrence Hill and John Archibald Wheeler. "Nuclear Constitution and the Interpretation of Fission Phenomena". In: *Phys. Rev.* 89 (5 1953), pp. 1102–1145. DOI: 10.1103/PhysRev.89.1102. URL: https://link.aps.org/doi/10.1103/PhysRev.89.1102.

[34] K. Hirose et al. "Role of Multichance Fission in the Description of Fission-Fragment Mass Distributions at High Energies". In: *Phys. Rev. Lett.* 119 (22 2017), p. 222501. DOI: 10.1103/PhysRevLett.119.222501. URL: https://link.aps.org/doi/10.1103/PhysRevLett.119.222501.

[35] Yoritaka Iwata. "Energy-dependent existence of soliton in the synthesis of chemical elements". In: *Modern Physics Letters A* 30.16 (2015), p. 1550088. DOI: 10.1142/S0217732315500881. eprint: https://doi.org/10.1142/S0217732315500881. URL: https://doi.org/10.1142/S0217732315500881.

[36] Yoritaka Iwata and Joachim A. Maruhn. "Energy density functional in nuclear physics". In: (2012). arXiv: 1211.2355 [nucl-th].

[37] B. Jurado et al. "Fission Cross Sections and Fission-Fragment Mass Yields via the Surrogate Reaction Method". In: *AIP Conference Proceedings* 1005.1 (2008), pp. 90–95. DOI: 10.1063/1.2920753. eprint: https://aip.scitation.org/doi/pdf/10.1063/1.2920753. URL: https://aip.scitation.org/doi/abs/10.1063/1.2920753.

[38] Beatriz Jurado. "The surrogate-reaction method and excitation-energy sorting in nuclear fission". Habilitation à diriger des recherches. Université de Bordeaux, Mar. 2015. URL: http://hal.in2p3.fr/tel-01262708.

[39] A V Karpov, A Kelić, and K-H Schmidt. "On the topographical properties of fission barriers". In: *Journal of Physics G: Nuclear and Particle Physics* 35.3 (2008), p. 035104. DOI: 10.1088/0954-3899/35/3/035104. URL: https://doi.org/10.1088%2F0954-3899%2F35%2F3%2F035104.

[40] G. Kessedjian et al. "Fission probabilities of ^{242}Am,^{243} Cm, and ^{244}Cm induced by transfer reactions". In: *Phys. Rev. C* 91 (4 2015), p. 044607. DOI: 10.1103/PhysRevC.91.044607. URL: https://link.aps.org/doi/10.1103/PhysRevC.91.044607.

[41] G. Kessedjian et al. "Neutron-induced fission cross sections of short-lived actinides with the surrogate reaction method". In: *Physics Letters B* 692.5 (2010), pp. 297 –301. ISSN: 0370-2693. DOI: https://doi.org/10.1016/j.physletb.2010.07.048. URL: http://www.sciencedirect.com/science/article/pii/S0370269310009007.

[42] P. Klüpfel et al. "Variations on a theme by Skyrme: A systematic study of adjustments of model parameters". In: *Phys. Rev. C* 79 (3 2009), p. 034310. DOI: 10.1103/PhysRevC.79.034310. URL: https://link.aps.org/doi/10.1103/PhysRevC.79.034310.

[43] M. Kortelainen et al. "Nuclear energy density optimization: Large deformations". In: *Phys. Rev. C* 85 (2 2012), p. 024304. DOI: 10.1103/PhysRevC.85.024304. URL: https://link.aps.org/doi/10.1103/PhysRevC.85.024304.

[44] R. Léguillon et al. "Fission fragments mass distributions of nuclei populated by the multinucleon transfer channels of the 18O+232Th reaction". In: *Physics Letters B* 761 (2016), pp. 125 –130. ISSN: 0370-2693. DOI: https://doi.org/10.1016/j.physletb.2016.08.010. URL: http://www.sciencedirect.com/science/article/pii/S0370269316304300.

[45] LISE++. In: (2017). URL: http://lise.nscl.msu.edu/lise.html.

[46] L.R. "Theories of nuclear fission: L. Wilets, (Clarendon Press: Oxford University Press, Oxford, 1964. x-132 p. 18 s)". In: *Nuclear Physics* 59.4 (1964), p. 691. ISSN: 0029-5582. DOI: https://doi.org/10.1016/0029-5582(64)90063-X. URL: http://www.sciencedirect.com/science/article/pii/002955826490063X.

[47] Bing-Nan Lu et al. "Multidimensionally constrained relativistic mean field model and applications in actinide and transfermium nuclei". In: *Physica Scripta* 89.5 (2014), p. 054028. DOI: 10.1088/0031-8949/89/5/054028. URL: https://doi.org/10.1088%2F0031-8949%2F89%2F5%2F054028.

[48] A. Mamdouh et al. "Fission barriers of neutron-rich and superheavy nuclei calculated with the ETFSI method". In: *Nuclear Physics A* 679.3 (2001), pp. 337 –358. ISSN: 0375-9474. DOI: https://doi.org/10.1016/S0375-9474(00)00358-4. URL: http://www.sciencedirect.com/science/article/pii/S0375947400003584.

[49] A. Mamdouh et al. "Large-scale fission-barrier calculations with the ETFSI method". In: *Nuclear Physics A* 644.4 (1998), pp. 389 –414. ISSN: 0375-9474. DOI: https://doi.org/10.1016/S0375-9474(98)00576-4. URL: http://www.sciencedirect.com/science/article/pii/S0375947498005764.

[50] Maria Goeppert Mayer. "On Closed Shells in Nuclei. II". In: *Phys. Rev.* 75 (12 1949), pp. 1969–1970. DOI: 10.1103/PhysRev.75.1969. URL: https://link.aps.org/doi/10.1103/PhysRev.75.1969.

[51] P. A. Moldauer. "Theory of Average Neutron Reaction Cross Sections in the Resonance Region". In: *Phys. Rev.* 123 (3 1961), pp. 968–978. DOI: 10.1103/PhysRev.123.968. URL: https://link.aps.org/doi/10.1103/PhysRev.123.968.

[52] William D. Myers and Wladyslaw J. Swiatecki. "Nuclear masses and deformations". In: *Nuclear Physics* 81.1 (1966), pp. 1 –60. ISSN: 0029-5582. DOI: https://doi.org/10.1016/0029-5582(66)90639-0. URL: http://www.sciencedirect.com/science/article/pii/0029558266906390.

[53] S. G. Nilsson. "Binding states of individual nucleons in strongly deformed nuclei". In: *Kong. Dan. Vid. Sel. Mat. Fys. Med.* 29N16 (1955), pp. 1–69.

[54] Sven Gösta Nilsson et al. "On the nuclear structure and stability of heavy and superheavy elements". In: *Nuclear Physics A* 131.1 (1969), pp. 1 –66. ISSN: 0375-9474. DOI: https://doi.org/10.1016/0375-9474(69)90809-4. URL: http://www.sciencedirect.com/science/article/pii/0375947469908094.

[55] K. Nishio et al. "Effects of nuclear orientation on the mass distribution of fission fragments in the reaction of ^{36}S $+^{238}$ U". In: *Phys. Rev. C* 77 (6 2008), p. 064607. DOI: 10.1103/PhysRevC.77.064607. URL: https://link.aps.org/doi/10.1103/PhysRevC.77.064607.

[56] M. Petit et al. "Determination of the 233Pa(n,f) reaction cross section from 0.5 to 10 MeV neutron energy using the transfer reaction 232Th(3He,p)234Pa". In: *Nuclear Physics A* 735.3 (2004), pp. 345 –371. ISSN: 0375-9474. DOI: https://doi.org/10.1016/j.nuclphysa.2004.02.017. URL: http://www.sciencedirect.com/science/article/pii/S0375947404002064.

[57] S. M. Polikanov et al. In: *Soviet Physics -JETP* 15 (1962), p. 1016.

[58] P.-G. Reinhard et al. "Shape coexistence and the effective nucleon-nucleon interaction". In: *Phys. Rev. C* 60 (1 1999), p. 014316. DOI: 10.1103/PhysRevC.60.014316. URL: https://link.aps.org/doi/10.1103/PhysRevC.60.014316.

[59] C.E. Rolfs and W.S. Rodney. *Cauldrons in the Cosmos: Nuclear Astrophysics*. Theoretical Astrophysics. University of Chicago Press, 1988. ISBN: 9780226724577. URL: https://books.google.co.jp/books?id=BHKLFPUS1RcC.

[60] Dieter Scharnweber, Walter Greiner, and Ulrich Mosel. "The two-center shell model". In: *Nuclear Physics A* 164.2 (1971), pp. 257 –278. ISSN: 0375-9474. DOI: https://doi.org/10.1016/0375-9474(71)90212-0. URL: http://www.sciencedirect.com/science/article/pii/0375947471902120.

[61] Karl-Heinz Schmidt and Beatriz Jurado. "Review on the progress in nuclear fission—experimental methods and theoretical descriptions". In: *Reports on Progress in Physics* 81.10 (2018), p. 106301. DOI: 10.1088/1361-6633/aacfa7. URL: https://doi.org/10.1088%2F1361-6633%2Faacfa7.

[62] N Schunck and L M Robledo. "Microscopic theory of nuclear fission: a review". In: *Reports on Progress in Physics* 79.11 (2016), p. 116301. DOI: 10.1088/0034-4885/79/11/116301. URL: https://doi.org/10.1088%2F0034-4885%2F79%2F11%2F116301.

[63] P. D. Stevenson and M. C. Barton. "Low-Energy Heavy-Ion Reactions and the Skyrme Effective Interaction". In: *Prog. Part. Nucl. Phys.* 104 (2019), pp. 142–164. DOI: 10.1016/j.ppnp.2018.09.002. arXiv: 1809.05801 [nucl-th].

[64] J.R. Stone and P.-G. Reinhard. "The Skyrme interaction in finite nuclei and nuclear matter". In: *Progress in Particle and Nuclear Physics* 58.2 (2007), pp. 587 –657. ISSN: 0146-6410. DOI: https://doi.org/10.1016/j.ppnp.2006.07.001. URL: http://www.sciencedirect.com/science/article/pii/S0146641006000627.

[65] V.M. Strutinsky. "Shell effects in nuclear masses and deformation energies". In: *Nuclear Physics A* 95.2 (1967), pp. 420 –442. ISSN: 0375-9474. DOI: https://doi.org/10.1016/0375-9474(67)90510-6. URL: http://www.sciencedirect.com/science/article/pii/0375947467905106.

[66] V.M. Strutinsky. ""Shells" in deformed nuclei". In: *Nuclear Physics A* 122.1 (1968), pp. 1 –33. ISSN: 0375-9474. DOI: https://doi.org/10.1016/0375-9474(68)90699-4. URL: http://www.sciencedirect.com/science/article/pii/0375947468906994.

[67] L. Tassan-Got. "A New functional for charge and mass identification in Delta E-E telescopes". In: *Nucl. Instrum. Meth.* B194 (2002), pp. 503–512. DOI: 10.1016/S0168-583X(02)00957-6. arXiv: nucl-ex/0103004 [nucl-ex].

[68] J. Treiner and H. Krivine. "Semi-classical nuclear properties from effective interactions". In: *Annals of Physics* 170.2 (1986), pp. 406 –453. ISSN: 0003-4916. DOI: https://doi.org/10.1016/0003-4916(86)90098-9. URL: http://www.sciencedirect.com/science/article/pii/0003491686900989.

[69] M. D. Usang et al. "Effects of microscopic transport coefficients on fission observables calculated by the Langevin equation". In: *Phys. Rev. C* 94 (4 2016), p. 044602. DOI: 10.1103/PhysRevC.94.044602. URL: https://link.aps.org/doi/10.1103/PhysRevC.94.044602.

[70] Robert Vandenbosch and John R. Huizenga. *Nuclear fission [by] Robert Vandenbosch [and] John R. Huizenga*. English. Academic Press New York, 1973, xii, 422 p. ISBN: 0127108505.

[71] D. Vautherin. "Hartree-Fock Calculations with Skyrme's Interaction. II. Axially Deformed Nuclei". In: *Phys. Rev. C* 7 (1 1973), pp. 296–316. DOI: 10.1103/PhysRevC.7.296. URL: https://link.aps.org/doi/10.1103/PhysRevC.7.296.

[72] D. Vautherin and D. M. Brink. "Hartree-Fock Calculations with Skyrme's Interaction. I. Spherical Nuclei". In: *Phys. Rev. C* 5 (3 1972), pp. 626–647. DOI: 10.1103/PhysRevC.5.626. URL: https://link.aps.org/doi/10.1103/PhysRevC.5.626.

[73] V. F. Weisskopf and D. H. Ewing. "On the Yield of Nuclear Reactions with Heavy Elements". In: *Phys. Rev.* 57 (6 1940), pp. 472–485. DOI: 10.1103/PhysRev.57.472. URL: https://link.aps.org/doi/10.1103/PhysRev.57.472.

[74] C. F. v. Weizsäcker. "Zur Theorie der Kernmassen". In: *Zeitschrift für Physik* 96.7 (1935), pp. 431–458. ISSN: 0044-3328. DOI: 10.1007/BF01337700. URL: https://doi.org/10.1007/BF01337700.

[75] W. Younes and H. C. Britt. "Neutron-induced fission cross sections simulated from (t, pf) results". In: *Phys. Rev. C* 67 (2 2003), p. 024610. DOI: 10.1103/PhysRevC.67.024610. URL: https://link.aps.org/doi/10.1103/PhysRevC.67.024610.

[76] W. Younes and H. C. Britt. "Simulated neutron-induced fission cross sections for various Pu, U, and Th isotopes". In: *Phys. Rev. C* 68 (3 2003), p. 034610. DOI: 10.1103/PhysRevC.68.034610. URL: https://link.aps.org/doi/10.1103/PhysRevC.68.034610.